1-2021

Machine learning approaches for lung cancer diagnosis.

Ahmed Mahmoud Ahmed Shaffie
University of Louisville

MACHINE LEARNING APPROACHES FOR LUNG CANCER DIAGNOSIS

By

Ahmed Mahmoud Ahmed Shaffie
M.Sc., Department of Engineering Mathematics and Physics,
Alexandria University, Alexandria, Egypt, 2012

A Dissertation
Submitted to the Faculty of the
J. B. Speed School of Engineering of the University of Louisville
in Partial Fulfillment of the Requirements
for the Degree of

Doctor of Philosophy in Computer Science and Engineering

Department of Computer Engineering and Computer Science
University of Louisville
Louisville, Kentucky

May 2021

MACHINE LEARNING APPROACHES FOR LUNG CANCER DIAGNOSIS

By

Ahmed Mahmoud Ahmed Shaffie
M.Sc., Department of Engineering Mathematics and Physics,
Alexandria University, Alexandria, Egypt, 2012

A Dissertation Approved on

April 21, 2021

---

by the Following Dissertation Committee:

Adel Elmaghraby, Ph.D., Co-advisor

Ayman El-Baz, Ph.D., Co-advisor

Ibrahim Imam, Ph.D.

Neal Dunlap, M.D.

Harry Zhang, Ph.D.

DEDICATION

This dissertation is dedicated to my grand mother's soul.

ACKNOWLEDGMENTS

In the name of Allah the most merciful, the most compassionate. All deepest thanks are due to Almighty Allah for the uncountable gifts given to me.

I would like to thank Dr Adel Elmaghraby, my dissertation co-advisor. His immense knowledge and insightful ideas have been of great help for the accomplishment of this work and his moral support helped me facing multiple challenges during hard times.

I also would like to express my deepest gratitude to Dr. Ayman El-Baz, my dissertation co-advisor, for his constant support, advising, and help over the course of my Ph.D. study. I thank him for allowing me to be part of his great research team and for giving me the opportunity to work on bright applications and gain different experiences in different domains. The completion of my research would not have been possible without his guidance and expertise. I also express my deepest gratitude to Dr. Ibrahim Imam, Dr. Neal Dunlap, and Dr. Harry Zhang for being on my dissertation committee with enthusiasm and taking interest in my research in the midst of many other responsibilities and commitments.

I also have to thank Dr. Ahmed Soliman for his useful discussions and valuable comments and feedback. He has never hesitated to share his experience in Markov-Gibbs random field and the field of image processing. I also express my deepest thanks to all members of the research group in the BioImaging Laboratory at the University of Louisville.

Last but not least, I would like to sincerely thank all my family members: my father Major General Mahmoud Shaffie, my mother Dr. Elham Tawfik, and my sister Dr. Rasha Shaffie, for their great patience, encouragement, and unconditional love.

ABSTRACT

MACHINE LEARNING APPROACHES FOR LUNG CANCER DIAGNOSIS

Ahmed Mahmoud Ahmed Shaffie

April 21, 2021

The enormity of changes and development in the field of medical imaging technology is hard to fathom, as it does not just represent the technique and process of constructing visual representations of the body from inside for medical analysis and to reveal the internal structure of different organs under the skin, but also it provides a noninvasive way for diagnosis of various disease and suggest an efficient ways to treat them. While data surrounding all of our lives are stored and collected to be ready for analysis by data scientists, medical images are considered a rich source that could provide us with a huge amount of data, that could not be read easily by physicians and radiologists, with valuable information that could be used in smart ways to discover new knowledge from these vast quantities of data. Therefore, the design of computer-aided diagnostic (CAD) system, that can be approved for use in clinical practice that aid radiologists in diagnosis and detecting potential abnormalities, is of a great importance. This dissertation deals with the development of a CAD system for lung cancer diagnosis, which is the second most common cancer in men after prostate cancer and in women after breast cancer. Moreover, lung cancer is considered the leading cause of cancer death among both genders in USA. Recently, the number of lung cancer patients has increased dramatically worldwide and its early detection doubles a patient's chance of survival. Histological examination through biopsies is considered the gold standard for final diagnosis of pulmonary nodules. Even though resec-

tion of pulmonary nodules is the ideal and most reliable way for diagnosis, there is still a lot of different methods often used just to eliminate the risks associated with the surgical procedure. Lung nodules are approximately spherical regions of primarily high density tissue that are visible in computed tomography (CT) images of the lung. A pulmonary nodule is the first indication to start diagnosing lung cancer. Lung nodules can be benign (normal subjects) or malignant (cancerous subjects). Large (generally defined as greater than 2 cm in diameter) malignant nodules can be easily detected with traditional CT scanning techniques. However, the diagnostic options for small indeterminate nodules are limited due to problems associated with accessing small tumors. Therefore, additional diagnostic and imaging techniques which depends on the nodules' shape and appearance are needed.

The ultimate goal of this dissertation is to develop a fast noninvasive diagnostic system that can enhance the accuracy measures of early lung cancer diagnosis based on the well-known hypotheses that malignant nodules have different shape and appearance than benign nodules, because of the high growth rate of the malignant nodules. The proposed methodologies introduces new shape and appearance features which can distinguish between benign and malignant nodules. To achieve this goal a CAD system is implemented and validated using different datasets.

This CAD system uses two different types of features integrated together to be able to give a full description to the pulmonary nodule. These two types are appearance features and shape features. For the appearance features different texture appearance descriptors are developed, namely the 3D histogram of oriented gradient, 3D spherical sector isosurface histogram of oriented gradient, 3D adjusted local binary pattern, 3D resolved ambiguity local binary pattern, multi-view analytical local binary pattern, and Markov Gibbs random field. Each one of these descriptors gives a good description for the nodule texture and the level of its signal homogeneity which is a distinguishable feature between benign and malignant nodules. For the shape features multi-view peripheral sum curvature scale space, spherical harmonics expansions, and different group of fundamental geometric features are

utilized to describe the nodule shape complexity.

Finally, the fusion of different combinations of these features, which is based on two stages is introduced. The first stage generates a primary estimation for every descriptor. Followed by the second stage that consists of an autoencoder with a single layer augmented with a softmax classifier to provide us with the ultimate classification of the nodule. These different combinations of descriptors are combined into different frameworks that are evaluated using different datasets. The first dataset is the Lung Image Database Consortium which is a benchmark publicly available dataset for lung nodule detection and diagnosis. The second dataset is our local acquired computed tomography imaging data that has been collected from the University of Louisville hospital and the research protocol was approved by the Institutional Review Board at the University of Louisville (IRB number 10.0642). These frameworks accuracy was about 94%, which make the proposed frameworks demonstrate promise to be valuable tool for the detection of lung cancer.

TABLE OF CONTENTS

LIST OF TABLES

LIST OF FIGURES

CHAPTER I
INTRODUCTION

Medical imaging is the different techniques that are utilized to reveal the interior of the human body in order to analyze it clinically, to diagnose, and monitor the body organs medical conditions. This is why medical imaging has crucial role in the early detection and the accurate diagnosis of different organ diseases. Usually, the original output of any imaging modality could be divided into four categories: one-Dimensional (1D) which is like the Electrocardiogram (ECG). Two-dimensional (2D) signal like an X-ray, in this type of data there is an ordinary 2D image, which is a flat image that appears as a rectangular array of values, that represents different signals that express the characteristics of a specific organ or location in the body, called pixels. Three-dimensional (3D) signal like Computed Tomography (CT), in this type of data there is a volume which is a stack of consecutive 2D images, every one of them called a slice. This volume is represented as a three dimensional array of values called voxels. Four-dimensional (4D) signal, in which there is a volume, but with multiple frames for this volume and it is obvious that the fourth dimension is time. The modern evolution of the medical imaging modalities is now providing a ton of scans with very high resolution and different degrees of contrasts. All the data stored in the scans shows a huge amount of information that needs to be interpreted by the radiologists. Therefore, there is a real need for an automated diagnostic system that will help to save time, cost, and exclude the complications that may be get involved in invasive surgical procedure. Of course, this systems will not replace the clinician or radiologists, it typically marks the location of suspicious areas, and gives the clinician or the radiologist a signal to investigate this part and make the final diagnoses. This will help to avoid the traditional human errors as a result of the huge amount of exhausting work which come from the large

number of images for only one patient and of course the radiologist has to interpret up to 50 cases per day [1]. There are many types of imaging modalities, each one based on various types of energy sources, such as light, X-rays, ultrasound and nuclear magnetic. The focal points and constraints of each imaging modality are principally operated by the basic physical and biological standards which impact the manner in which every energy source affect the tissues [2]. The most common imaging modalities are: magnetic resonance imaging (MRI), computed tomography (CT), ultrasound, positron emission tomography (PET), and single photon emission computed tomography (SPECT) (see Figure 1).

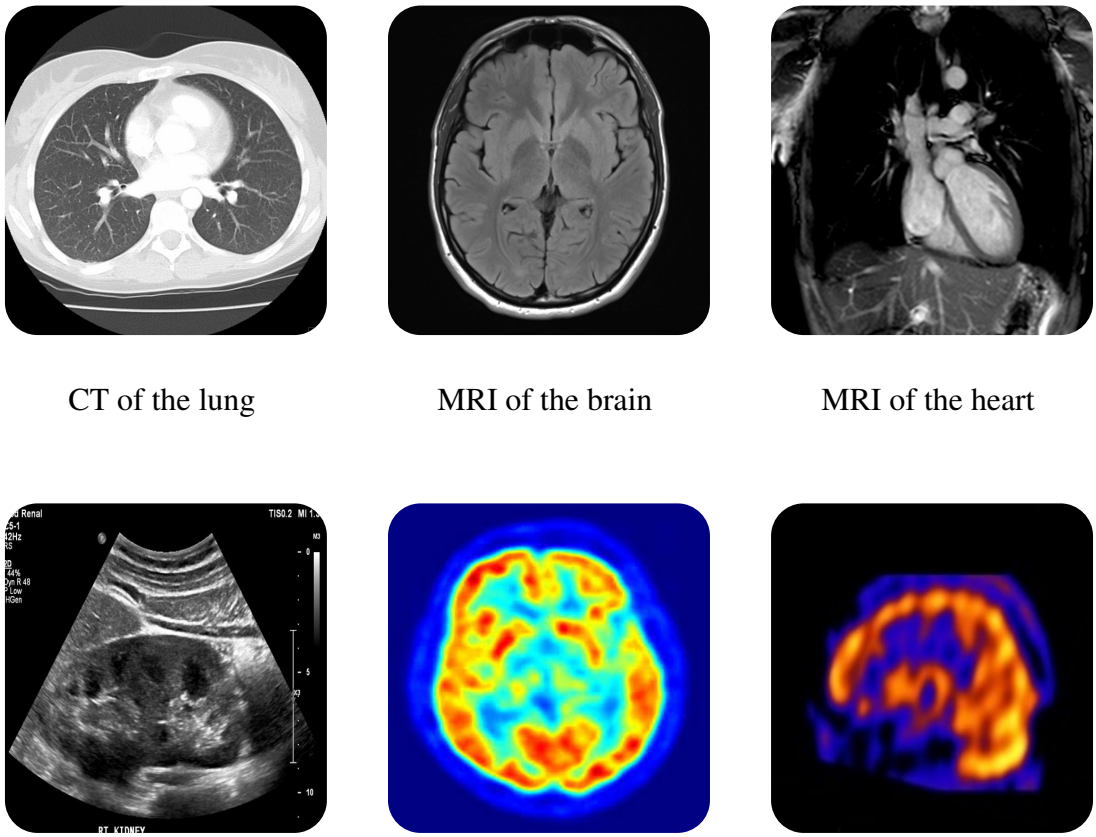

CT of the lung | MRI of the brain | MRI of the heart

Ultrasound of the kidney | PET of the Brain | Liver SPECT image

FIGURE 1: The most common medical images

Imaging modalities could be also divided into two categories based on the provided information by the modalities. The first category is functional imaging or sometimes called

physiological imaging, which depends on measuring and identifying the changes in the blood stream, metabolism, and most of the physiological activities. Ultrasound, PET, and SPECT are examples of functional imaging. The second category is structural imaging, which is concerned with the visualization of the anatomy of the organs to show whether there is any injury or anomaly. CT and MRI are examples of structural imaging, although they also belong to functional imaging. As the CT is the related imaging modality that is used through the dissertation, it will be the focus of the following section.

A. COMPUTED TOMOGRAPHY (CT) IMAGING

Computed Tomography (CT) is one of the most popular imaging techniques. This imaging modality evolved since the mid-seventies and proved its efficiency in multiple medical domain applications. The CT remodels internal object structures from multiple projections acquired by estimating transmission of X-ray radiation through the object. CT scanner utilizes a motorized X-ray source that rotates around a circular shaped structure called a gantry. The bed where the patient lies during the CT imaging procedure moves through the gantry and the X-ray tube rotates around the patient pointing arrow beams of x-rays through the body. CT scanners adopt special digital X-ray detectors instead of film. These detectors are placed in an opposite direction from the X-ray source. When the X-rays vacate the patient, they are collected by the detectors and transmitted to a computer. Every time the X-ray source finishes a full rotation, the CT computer utilizes sophisticated mathematical approaches to build a 2D image slice of the patient. Once a full slice image is finalized the bed moves into the gantry. The same process is repeated until physicians get the needed number of slices. Images are either shown individually or stacked together by the computer to produce a 3D image of the patient that identifies many parts of the patient like the organs, the skeleton and the tissues along with any abnormalities the doctors are trying to distinguish. The integral incorporation of rays in the patients' body from multiple directions of the X-ray radiation permit the reconstruction of point-wise X-ray attenuation

coefficients for each location in the object. These coefficients are calculated in integer Hounsfield units (HU), named by CT numbers. These numbers vary from 1000 (air) to +1000 (cortical bone) and represent the intensity values of CT scans. Figure 2 shows different projection for CT scan.

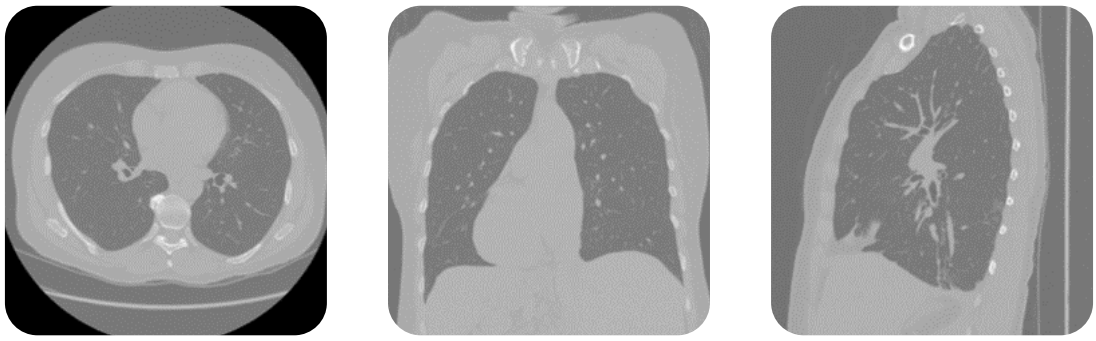

Axial view Coronal view Sagittal view

FIGURE 2: CT scan for the lung from different views: axial, coronal, and sagittal

1. Structural CT

In old years, the CT scans were captured in an axial or transverse plane that is orthogonal to the long axis of the body. In more recent years, the development of multi-slice and spiral CT allowed the 3D reconstruction images from multiple 2D views. Nowadays, images with much better details and in a faster time are obtained with CT scanners with 64 or more detectors. Images resolution and the necessary time for images acquisition continue to improve and this help in diagnosing diseases in a more efficient way. This helped in fasting treatments and amplified the survival rate of patients.

2. Contrast–enhanced CT (CE-CT)

CE-CT Contrast agents are used during contrast enhanced computed tomography to enhance physiological tissues and organs of the body. While bones can be identified easily

on X-ray images, imaging some other organs and soft tissues is more challenging. Sufficient contrast is crucial for identifying a difference in the density between areas of a CT image. Identifying a disease may be a difficult task due to very low contrast between pathological tissues (for e.g. tumors, abscesses and metastases) and normal organ tissues and this encouraged the use of contrast–enhanced CT. Contrast agents for this imaging modality is used in multiphasic CT researches to give dynamic information of blood supply (e.g., liver CT). It is also utilized in CT angiography (CTA) to delineate vessels and in CE-CT studies of various body parts to attain opacification of the studied tissue (e.g., kidney CT) comparing to the background tissue. Contrast enhanced multi-detector row CT (MDCT) took over several well-known imaging modalities including cholangiography, intravenous urography and catheter angiography because it allows faster examination with clearer output images. Figure 3 shows the effect of the contrast agent on making the scan clear.

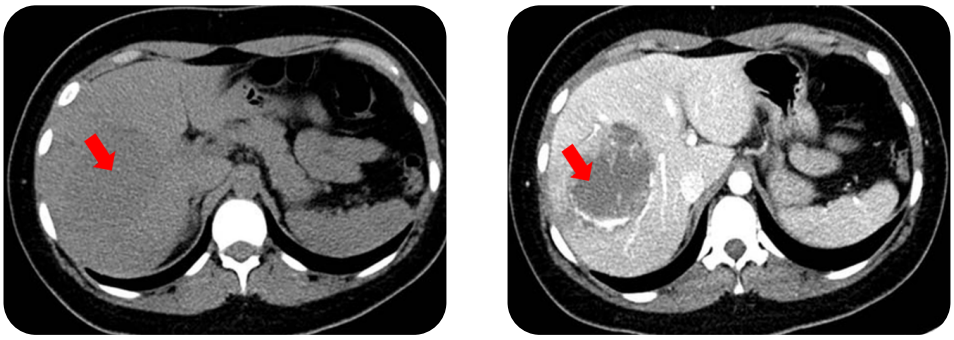

Unenhanced CT Enhanced CT

FIGURE 3: Two examples of enhanced and unenhanced computed tomography (CT) scans of the liver

3. Microtomography (Micro-CT)

Micro-CT is a 3D imaging technique that use X-rays to see inside an object, slice by slice. Micro-CT, named also by microtomography or micro computed tomography, is comparable to hospital CT or CTA scan imaging but with increased resolution because it

uses a small scale. Samples can be scanned with pixel sizes as small as 100 nanometers and objects can be imaged as large as 200 millimeters in diameter. Micro-CT scanners catch multiple 2D planar X-ray images and rebuild the data into 2D cross-sectional slices. These slices can be processed into 3D models as well or even printed as 3D physical objects for analysis. While with 2D X-ray systems, it is possible to see through an object, with 3D micro-CT systems, it is possible to see inside the object and divulge internal features.

4. CT angiography (CTA)

Computed tomography angiography (CTA) utilizes an injection of contrast material into blood vessels and CT scanning to assist in the diagnosis and evaluation of blood vessels disease or similar conditions, such as blockages or aneurysms. Compared to other imaging techniques, CTA has a lower cost and acquire images in a faster way. It allows the detection of aneurysms (enlarged blood vessels) and shows the vessels damages early enough to find appropriate therapies.

5. Dynamic CT imaging (4D-CT)

Dynamic volume CT scans are similar to normal CT scan, except that the patient is asked to perform movements during the scan. Dynamic volume CT scans allow the clinician to acquire unique 4D information about joint motion. The high resolution 4D information attributed by these scans is not available using other techniques, including X-ray, MRI and Ultrasound.

6. CT imaging: Advantages and disadvantages

At present, the CT modality is faster and more universally available than other imaging modalities. This results in low per-scan costs. CT allows the acquisition of bones, blood vessels and soft tissue in the same time. Unlike the MRI imaging modality, CT permit the

separation of two inner structures separated by small distances from each other. It is also less sensitive to patient movement and the radiation don't stay in the body after the examination. Despite all these advantages, one concern resides in the fact that CT uses X-ray radiation, which can harm patients by causing both cancer and DNA damages. To reduce the radiation effect novel CT technologies utilizes low radiation but this introduce images deterioration.

B. Lung Cancer

Cancer in general is a very wide term for a category of diseases in which the abnormal cells in the human body start to develop and grow out of control as well as invade the surrounding normal cells. This cancer is called lung cancer when it starts in lung and it may spread to different organs, such as brain. Also the opposite could happen and affect the lung from other organs. The cancer is called metastases, when it spread to an organ from another one. Lung cancer is the second most common cancer in men after prostate cancer and in women after breast cancer, but it is considered the leading cause of cancer death among both gender in the United States as about 1 out of every 4 cancer deaths is resulting from lung cancer [3]. Cigarette smoking is the main source of lung cancer. It also may happen as a result of using different types of tobacco, such as hookah or pipes, exposed to secondhand smoke or some certain substances, such as radon, and having cancer family or personal history. It could be divided into two main categories, small cell that appears small and round under a microscope and non-small cells which are larger and more common that the small cells.

1. Pulmonary Nodules

The first indicator of the lung cancer is the Pulmonary nodules, which are spot on the lung with no definite shape that appears on a chest X-ray or chest CT scan as a white

spot as it is more solid than the regular lung tissue. Figure 4 shows different samples of benign and malignant nodules. Lung nodules are visible on around 50% of the CT scans of the adult and this is why they are very common and more than 95% of these nodules are benign ones. The benign nodules are usually the result of old infections (such as tuberculosis), noninfectious inflammation (such as rheumatoid arthritis), or noncancerous tumors (such as fibroma). The malignant nodules mainly could be determined from the following characteristics: (1) The malignant nodule has very high growth rate, as it may double in size in a few months. (2) The border of the malignant nodule is irregular and has a complex shape comparing with the well define border of the benign one. (3) The large nodule in size has a greater probability to be malignant (greater than twenty millimeters). (4) The malignant nodule has eccentric and inhomogeneous texture comparing with the benign nodule.

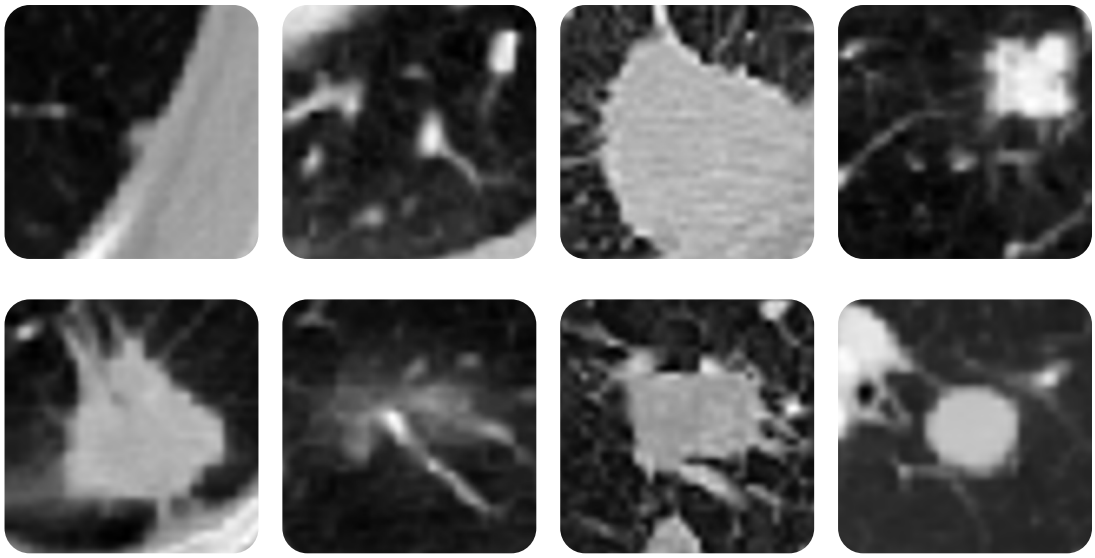

FIGURE 4: Samples of 2D axial projection for benign (*first-row*) and malignant (*second-row*) lung nodules.

2. Diagnosis of Lung Cancer

Histological examination through biopsies is considered the gold standard for final diagnosis of pulmonary nodules. These biopsies could be collected in two ways. The first one is transthoracic Needle biopsy, in the beginning the doctor may make a small incision in the patient skin where the needle will be inserted, then while the patient hold his breath and remain as still as possible, the doctor will insert the needle through his skin and chest wall, the patient may feel pressured and then a quick sharp pain when the needle reaches the surfaces of the patient's lung. The doctor will quickly obtain the sample of the tissue and withdraw the needle. Afterwards a chest x ray or any type of imaging technique will be used to make sure that the lung has not collapsed. Figure 4 shows an illustration of taking biopsy samples from the lung. The second one is bronchoscope biopsy. The bronchoscope

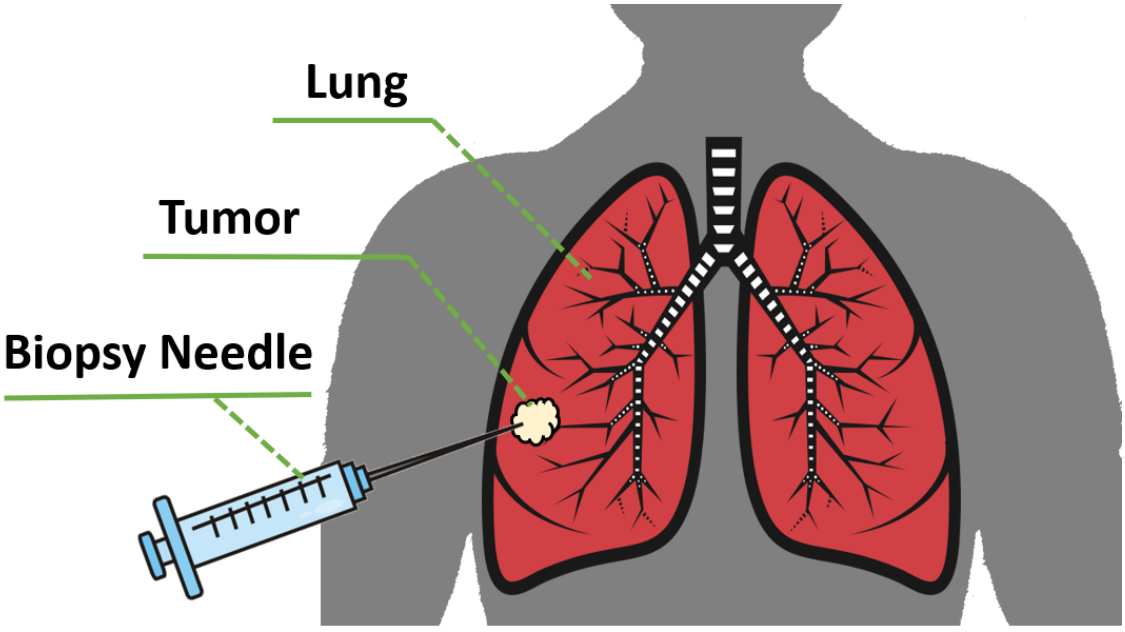

FIGURE 5: Taking lung biopsy samples illustration

is used to sample abnormal spots in the lung. The tube is passed through the mouth or nose of the patient and goes into the trachea, from there it passes through the bronchial tubes to be in the lung. Biopsy tools are gently passed through the bronchoscope to reach a few

abnormalities, a live x-ray called fluoroscope is used to watch the biopsies tools reach the lung sacs. Now biopsies and other samples can be taken and additional ones may be taken also for various tests. Figure 6 shows an illustration of using bronchoscope in the lung. Usually they use the transthoracic needle biopsy to obtain samples from tumors which is

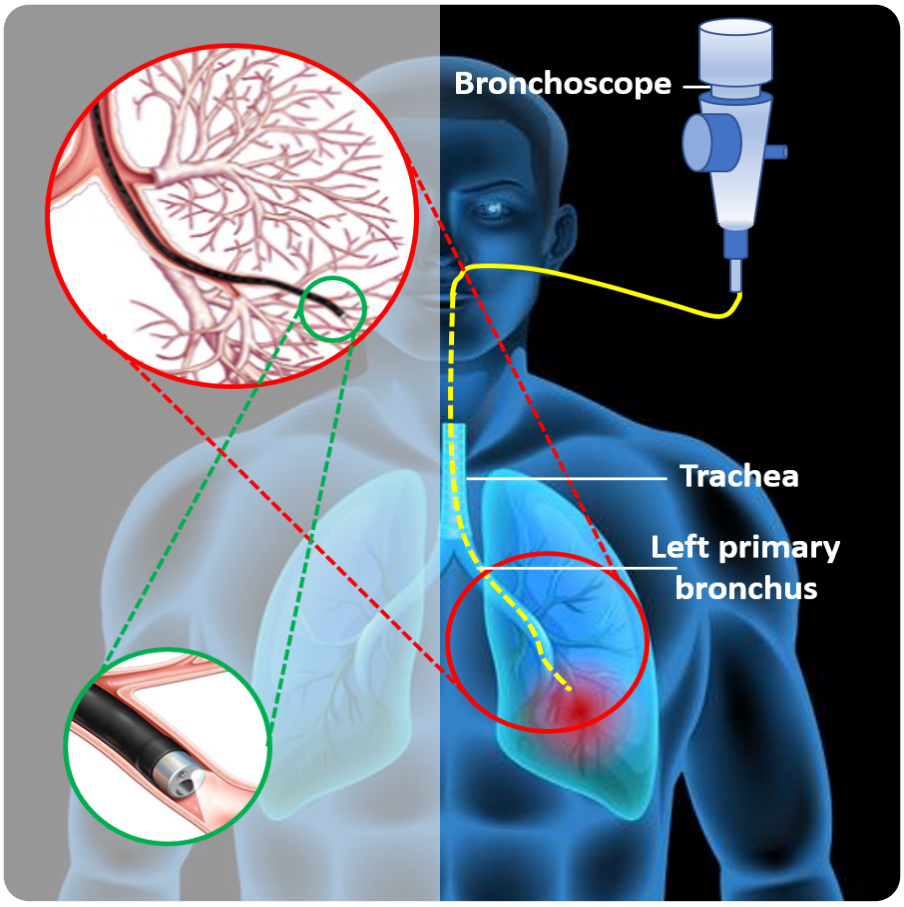

FIGURE 6: Illustration of using the flexible bronchoscope

near the chest wall as it will be very difficult to reach using the bronchoscope through the lung bronchioles. However, the transthoracic needle biopsy and bronchoscope are less invasive comparing with the surgical biopsy that needs general anesthesia, but they are still an invasive way for diagnosis and there is a very high risk as some problems may happen like: Pneumonia, infection, coughing up blood, collapsed lung, or bleeding. In other words, even though resection of pulmonary nodules is the ideal and most reliable way for

diagnosis, there is a real need to eliminate the risks associated with the surgical procedure through noninvasive methods. And actually this was the great motive to implement a new noninvasive CAD system.

C. The role of the imaging modalities in lung cancer diagnosis

Usually when people start to feel the symptoms of the lung cancer, such as chest pain, weight loss without justification, wheezing, or coughing that does not stop, they start visiting the physician that most probably will ask them to make a chest CT scan. The radiologist will start to analyze the scans. If the radiologist found a nodule, which will happen in most cases, then the radiologist has to check the nodule size. If the nodule size is small (less than $4mm$) the radiologist will ask for another scan after 6 months to check the growth rate of the nodule, which will be the indicator of the malignancy of that nodule. If the nodule size is large (more than $20mm$) then the nodule is diagnosed as a malignant nodule (see Figure 7). This procedure make the diagnosis of the lung cancer happen in a very late stage which make the recovery very difficult. This is why the Objective of

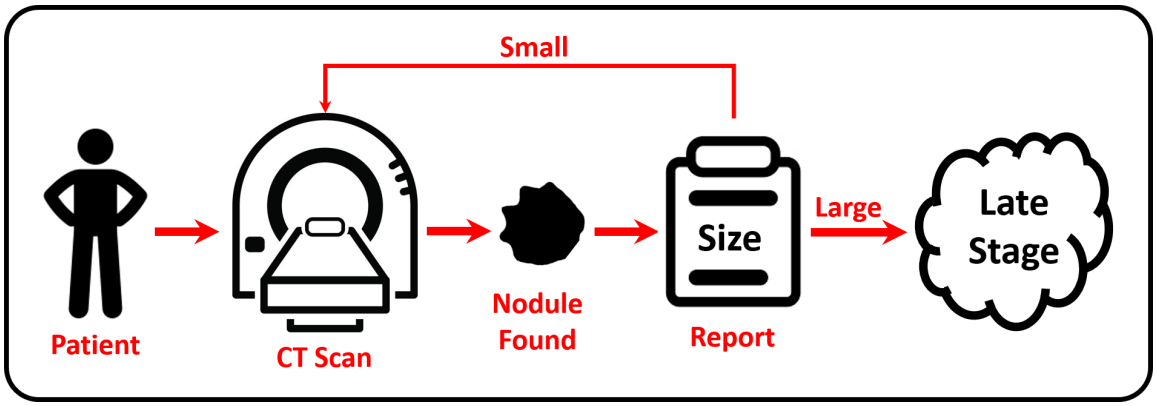

FIGURE 7: Illustration of the traditional procedure of the lung nodule diagnosis.

this dissertation at first stage was to develop a new non-invasive diagnostic system for the classification of lung nodules (whether it is benign or malignant) using single CT scans. Then to evaluate the developed CAD system accuracy based on biopsy confirmed diagnosis

and radiologists estimates of the likelihood of malignancy of lung nodules on CT scans.

D. Dissertation organization

The dissertation consists of 5 chapters. The following remarks summarize the scope of each chapter:

- Chapter I introduces some basic concepts about medical images. It also talks about pulmonary nodules and how it indicate the presence of the lung cancer.
- Chapter II overviews the existing methodologies of the computer aided diagnosis (CAD) systems for lung cancer and presents a survey about the challenges and the limitations of the existing methods of pulmonary nodules diagnosis. It also shows how the developed system could overcome these limitations.
- Chapter III presents a novel and noninvasive framework for pulmonary nodule diagnosis using different appearance and shape features.
- Chapter IV gives an overview about the used dataset for validating the developed methodology. It also presents the experimental evaluation measures that are used to evaluate the presented frameworks and each feature individually.
- Chapter V concludes the developed work and outlines the future work.

CHAPTER II
A SURVEY OF MODELS AND METHODS FOR LUNG CANCER DIAGNOSIS

This chapter reviews the recent applications and frameworks utilized for lung cancer diagnosis. Computer-aided diagnosis (CAD) system has a very important clinical application not only because it saves the time of the radiologists but also because it helps in the early detection of the lung cancer and consequently increases the survival rate of the patients [4–37]. Fundamentally the CAD system depends on imaging analysis and pattern recognition techniques. It is used not only for lung cancer diagnosis, but also for different medical applications for different organs [38–138]. It consists mainly from five steps: images preprocessing, lung segmentation, nodule detection, detected nodule segmentation, and finally, nodule classification whether malignant or benign. This chapter will give an overview about each step of the CAD system, and will focus on the last step which is nodule classification or diagnosis as the dissertation subject is about lung nodule diagnosis by giving a detailed survey about the state-of-the-art methodologies and researches about it. Additionally, it will show the advantages and disadvantages of each framework highlighting the obstacles that faces the researchers in that domain and the limitations of each method.

A. Introduction

Lung cancer is a major public health problem all over the world and is the leading cause of cancer deaths in the US. It is estimated in the US for 2020 that the number of the new cases of lung cancer will be about $228,820$ cases ($116,300$ male and $112,520$ female) and that the number of the deaths from lung cancer is about $135,720$ deaths ($72,500$ male

and $63,220$ female). The danger in that decease hide in its late diagnosis, as the majority of the diagnosed cases with lung cancer are more than 65 years old and the average of their ages is approximately 70 years. This means that the early diagnosis of the lung cancer, by identifying the malignant nodules. will lead to an effective treatment and will boost the chance of the patient to survive. The most common imaging modalities that is used for screening the lung and detecting the pulmonary nodules is the CT. The huge amount of data, that are provided by the CT, need an accurate CAD system to utilize all these data to give a precise diagnosis for the detected lung nodules. There are a lot of research papers about the implementation of CAD systems for lung cancer diagnosis. These researches utilize different types of imaging modalities and the performance of these systems could be compared in terms of different measures, such as accuracy, specificity, sensitivity, running time, and the level of automation.

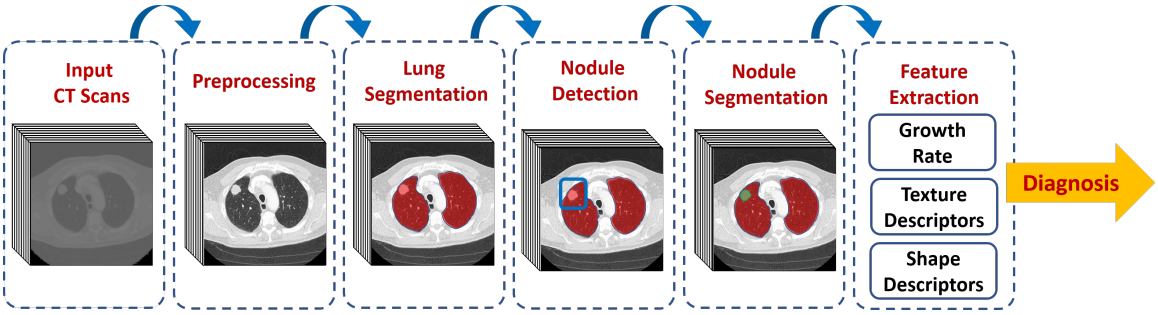

FIGURE 8: The general structure of Computer aided diagnosis system for lung cancer diagnosis. The input of that system is the medical images. Then a preprocessing step to make the images clearer and reduce the noise and artifacts. Lung segmentation is utilized to minimize the searching area. Nodules detection is utilized to suggest nodule candidates and reduce the false positive nodules. Nodules segmentation is responsible of creating a contour around the suspected nodules. Finally a group of features are used to diagnose the nodule based on it.

Figure 8 illustrate the structure of any CAD system. It starts by specifying the type

of the modality images that will be the input for that CAD system. The preprocessing step is very important to reduce the noises and the artifacts in the images. This step also could use different filters depending on the clinical application that will use that system. It is followed by the lung segmentation step to minimise the searching area for lung nodules. The nodule detection works on identifying the lung nodules and reduces the false positive candidates in the lung segmented area. Next, a nodule segmentation step to specify precisely the contour of the lung nodule to be able in the feature extraction step to extract different features to that nodule, such as texture and shape features. Finally, the diagnosis or classification step, that divides the nodules into two groups benign and malignant nodules using different machine learning techniques. In the rest of that chapter a brief talk will be started about each step in the CAD system showing available techniques for implementing it and a detailed survey about the diagnosis step as it is the focus of this dissertation.

B. Lung segmentation

Lungs segmentation is an important task in every lung cancer diagnosis system. This task though is challenging because lung fields have an heterogeneous nature, are close in gray level to different soft tissues (bronchioles, veins, arteries and bronchi), are anatomically variable, and are acquired with different scanning protocols, scanners and dose of radiation. Many researchers oriented their publications toward segmenting lung regions from CT scans. Multiple categories of lung segmentation frameworks evolved and included architectures that are based on deformable boundaries, signal thresholding, shape and edges modeling, and recently deep learning algorithms. Authors validated them with metrics such as: processing time, automation level and accuracy. Some of the latest works include those of [139] who proposed an automatic segmentation of lungs in CT scans based on Convolutional Neural Network (CNN), Mask R-CNN combined with unsupervised and supervised machine learning methods that includes K-means, Bayes, Gaussian Mixture Models (GMMs) and Support Vectors Machine (SVM). They stated that their Mask R-

CNN with k-means kernel method achieved the best results for the lung segmentation task with an average runtime of 11.2 s and an accuracy of 97.68 %.

Another lung segmentation architecture was proposed by Liu et al. [140]. In a first step, authors denoised lung CT images using an image decomposition based filtering strategy. Then they segmented their images using multiple morphological operations with wavelet transformation. To further refine the contour of their segmented lungs and smooth the extracted lung contours, they used a contour correction approach built on a fast corner detection technique. Authors validated their algorithm with the Jaccard's similarity index that achieved 94.91% and the Dice similarity coefficient that achieved 98.04% comparing to the groundtruth lung regions.

Comelli et al. [141] proposed a two deep learning methods for the lung segmentation task: U-Net and E-Net. They used to test their algorithms 42 studies of patients where 32 are used for training. They compared the performance of their algorithms with the groundtruth, based on the similarity metric. They concluded that the E-Net deep learning algorithm could be a good fit for this task where it achieved a clinically acceptable segmentation with a dice similarity coefficient of 95.90%.

Hofmanninger et al. [**?**, 142] compared four generic deep learning approaches (U-net, Dilated Residual NetworkD-22, ResU-net, and Deeplab v3+.) to two available lung segmentation algorithms (Progressive Holistically Nested Networks (P-HNN) and the Chest Imaging Platform (CIP)). They tested their algorithms on three public datasets and on a routine imaging data that contain six different diseases. They proved that the Dice similarity coefficients (DSC) didn't vary over 0.02 for all deep learning methods. The U-Net algorithm achieved the best classification results where training on the routine achieved a DSC of 0.97, training on the Lung Tissue Research Consortium public dataset achieved a DSC of 0.94 and training on the Anatomy 3 public dataset achieved a DSC of 0.92.

Tan et al. [143] implemented a deep learning Generative Adversarial Network (GAN)-based lung segmentation framework for the lung segmentation task. They stated that their

method could be generalised to different neural networks. They tested their algorithm on multiple datasets including the Quantitative Imaging Network (QIN) and the LIDC-IDRI collection. Their system has been evaluated using two metrics: shape similarity and segmentation quality. For the QIN dataset , the best shape similarity achieved a value of 2.449 and the best segmentation quality achieved a value of 0.978. For the LIDC-IDRI dataset, the best shape similarity achieved a value of 3 and the best segmentation quality achieved a value of 0.972.

C. Lung nodule detection

After the extraction of the lungs, the next step is to detect nodules in their search space. Early detection of lung tumors could increase the patients survival rate which makes this task an important one, though challenging because it is sometimes hard to distinguish between nodules and other lung structures such as ribs and vessels. The standard procedures for the lung nodules detection consist of two major steps: selection of initial candidates and then False Positive Nodules reduction. Multiple frameworks for this task are based on morphological and texture features extraction then classification and lately on deep learning algorithms. Some of these works include those of Su et al. [144] who proposed a Faster R-CNN for the lung nodules detection task. They tuned multiple parameters for their network and proved that their results could improve with optimized ones. They reported that the best parameters for their work are: a learning rate of value 0.001, attenuation coefficient of 0.1, batch size of 64 and a value of Dropout of 0.5. Their system reached an accuracy of 91.2% and improved the detection accuracy of some other works by more than 20%.

Another computer aided detection system include those of Tougaccar et al. [145] who used VGG-16, AlexNet and LeNet deep learning models for the lung nodules detection task. During the training phase data augmentation techniques such as horizontal turning and filling, cutting, zooming were applied on the used dataset to increase the clas-

sification accuracy. All used deep learning algorithms are used to extract features from the last fully-connected layer and combined with traditional classfiiers such as: linear regression (LR), k -nearest neighbor (kNN), linear discriminant analysis (LDA) and support vector machine (SVM). The best results were reached by AlexNet model combined with KNN classifier with an accuracy of 98.74%. Authors also used the minimum redundancy maximum relevance (mRMR) feature selection method to select relevant features. When they used the features selection method, they reached a higher accuracy of 99.51% when applying AlexNet with KNN.

Suzuki et al. [146] developed a modified three-dimensional (3D) U-net deep-learning model. They trained their model on the Lung Image Database Consortium and Image Database Resource Initiative (LIDC-IDRI) dataset. They validated their algorithm using an internal model validation with an 89 CT scan not used for training from the LIDC dataset and an external validation using 450 CT scan from the urban university hospital in Japan. Each CT scans include at least one nodule of > 5 mm based on the opinion of an experienced radiologist. They evaluated their system using the competition performance metric (CPM) and the highest results for the internal validation achieved 94.7% while the highest results for the external validation achieved 83.3%.

Cao et al. [147] developed a two-stage convolutional neural networks (TSCNN) for the lung nodules detection task. In the first stage an improved U-Net segmentation network is established. They introduced during this stage, a sampling strategy for training to obtain a high recall rate. In the second stage they applied a 3D-CNN for false positive reduction. They used in this stage, the random mask method for data augmentation and they used ensemble learning to generalize the ability of the model for false positive reduction. Authors tested their algorithm on the LUNA dataset composed of 888 CT scans and achieved a competition performance metric of 0.925.

Another lung nodules detection system was proposed by Veronica. [148]. Authors pre-processed their images then they segmented potential nodules using the Fuzzy C-Means

(FCM). They extracted after that features to classify CT images as normal or with nodules using multiple classifiers such as: Artificial Neural Network (ANN), Naive Base (NB), K-nearest neighbors (KNN), etc. They concluded that the ANN classifier along with the Oppositional based Ant Lion Optimization (OALO) algorithm achieved the best results with a sensitivity of 0.933, a specificity of 0.8 and an accuracy of 0.866.

D. Lung nodule segmentation

After the lung nodules detection task that identifies nodules from other structures, the lung nodules segmentation task is reached, that consists of delineating the extent of focal nodular lesions from CT scans. This task is very important for every CAD system because it may affect the lung nodule diagnosis accuracy in case the segmentation is not optimal. Some of these works include those of Cao et al. [149] who proposed a Dual-branch Residual Network (DB-ResNet). The authors proposed a pooling method named by the central intensity pooling layer (CIP) that extracts features from the central voxel of the block and then they used CNN to get the convolutional features from the center voxel of the block. To select the voxels that belong to the boundary of the nodule, the authors used a weight sampling strategy. They evaluated their system on the LIDC-IDRI dataset that contains 986 nodules. They showed that their method is efficient for such task with a dice similarity coefficient (DSC) of 82.74%.

Another CAD system was proposed by Keetha et al. [150]. Authors proposed an end to end deep learning model for the lung nodules segmentation task that integrates a bidirectional feature network (Bi-FPN) between the encoder and decoder of the architecture. In addition, the model utilizes the class weights of the masks and a Mish activation function to enhance the efficiency of the segmentation. The authors evaluated their system on the publicly available LUNA-16 dataset that is composed of 1186 lung nodules. Their architecture achieved a Dice similarity coefficient (DSC) of 82.82%.

Dong et al. [151] proposed a multi-view secondary input residual (MV-SIR) con-

volutional neural network model for 3D lung nodule segmentation. The proposed model include six sub-models that allows learning of 3D lung nodules sliced into three views of features. By doing this, the 3D lung nodules segmentation model is converted to a voxel model classification that input multi-view patches into the model and influence whether the voxel points is part of the nodule or not. The model was validated using the Dice coefficient and the average surface distance. It achieved a value of 0.926.

Hesamian et al. [152] proposed a deep learning based method that tracks the changes of nodule shapes over continuous slices. The authors elaborated a new synthetic image to study the change in pattern of nodules from slice to another and used the U-Net architecture to reach their objective. They proved that their method is efficient for such task and achieved a Dice Similaryty Coefficient (DSC) of 93.14%, a sensitivity of 91.76% and a positive predictive value (PPV) of 92.18%.

Xiao et al. [153] proposed a lung nodules segmentation based on the 3D-UNet, Res2Net and a novel convolutional neural network called 3D-Res2UNetdeep learning models. They stated that the 3D-Res2UNetdeep model direct multi-scale features with a finer granularity, while rising the receptive field of each layer of the network which resolve the deep level problem. They also stated that the accuracy of the segmentation increased because the network is not under the influence of gradient explosion problems and gradient disappearance. Authors tested their algorithm on the LUNA16 dataset and achieved a dice coefficient index of 95.30% and a recall rate of 99.1%.

E. Lung nodule diagnosis

Lung nodules classification is an important task in every Computer Aided Diagnosis system (CAD). This task consists of determining if nodules are benign or malignant after detecting and segmenting them from the corresponding chest images. Over the past years researchers developed CAD systems that are mainly divided into three categories. The first one relies on traditional handcrafted features (ex: geometrical size, shape, ap-

pearance and texture features) extraction then classification, the second one relies on deep learning algorithms where features are learned during the training process then classified within the same framework and the third category relies on extracting deep features and generative features then fuses them and classifies them with traditional classification algorithms. Generally the performance of systems is evaluated using the Area Under Curve of the Receiver-operating-characteristic (AUC), specificity, sensitivity, precision, F-score and accuracy metrics since it is a two class classification task.

1. Diagnosis of lung nodules based on traditional features extraction then classification

These CAD systems usually follows the same schema: Features are extracted from the defined regions of Interest (ROIs) then classified using traditional classifiers and evaluated by the previously described metrics. Systems differ only on the type of features that are extracted and on the classifiers that are used to classify them. Bellow, systems based on a combination of shape, appearance or/and texture features and diverse classifiers.

In early years, researchers focused on the lung nodule diagnosis task using shape and appearance features. They thought that the difference in size between benign and malignant samples and some shape oriented characteristics could be enough for the classification of both nodule categories. Some of these works include those of Likhitkar et al. [154] who proposed a framework modeled in four steps: image enhancement, segmentation, feature extraction and classification. They used the growth rate, shape, density and boundary of the nodule as input features for the (Support Vector Machines) SVM classifier to distinguish between benign and malignant nodules. Their method was applied to a dataset of 500 images divided into 400 images for training and 100 images for testing and achieved a false acceptance rate (FAR) of 4%, a false recognition rate (FRR) of 3% and a genuine acceptance rate (GAR) of 96%.

Farahani et al. [155] proposed an ensemble-based system to classify each pulmonary nodule by integrating multiple classifiers like SVM, K-nearest-neighbors (k-NN),

and neural networks. The classifiers learned results on five morphological features: Roundness, Circularity, Compactness, Ellipticity, and Eccentricity and their outputs are combined using majority voting. They tested their algorithm on 60 CT scans from the Lung Image Database Consortium (LIDC) dataset [156] and achieved an accuracy of 94.65%, sensitivity of 84.16%, specificity of 97.30%, G-mean of 90.49%, precision of 88.76% and F-measure of 86.40%.

The CAD system proposed by Firmino et al. [157] distinguished between malignant and benign lung nodules from the LIDC dataset. They used the scores provided by the radiologists for each nodule in the used dataset as features (Calcification, Internal structure, Lobulation, Margin, Sphericity, Spiculation and Texture) along with three different classification algorithms: Fisher's Linear Discriminant (FDA), Gaussian Naive Bayes (NB) and SVM using both 10-fold cross-validation and leave-one-out validations measures. They validated their algorithm on 304 malignant and 116 benign nodules. Since each nodule from the LIDC dataset have been ranked by radiologists with scores going from 1 to 5 with 1 is the score of a benign nodule given their opinion and 5 is the score of a malignant nodule given their opinion, authors divided their categories as follow: nodules highly unlikely of being malignant, nodules moderately unlikely of being malignant, nodules with indeterminate malignancy, nodules moderately suspicious of being malignant and nodules highly suspicious of being malignant. They reported that the SVM classier achieved the best AUC with 10-fold cross-validation with an AUC of 0.91 for nodules highly unlikely of being malignant, 0.80 for nodules moderately unlikely of being malignant, 0.72 for nodules with indeterminate malignancy, 0.67 for nodules moderately suspicious of being malignant and 0.83 for nodules highly suspicious of being malignant. Same as for the leave-one-out validation measure, the SVM classifier achieved the best classification results with: an AUC of 0.93 for nodules highly unlikely of being malignant, 0.78 for nodules moderately unlikely of being malignant, 0.69 for nodules with indeterminate malignancy, 0.67 for nodules moderately suspicious of being malignant and 0.85 for nodules highly suspicious of

being malignant.

Shewaye et al. [158] proposed an automated system to diagnosis benign or malignant nodules in CT images. Experimental results were validated using this combination of histogram and geometric features: nodule diameter, nodule aspect ratio, nodule area, approximate nodule perimeter and gray scale histogram and classified using different linear and non-linear discriminant classifiers. The linear ones consist of Logistic Regression and Linear SVM classifiers and the non-linear ones are: K-Nearest Neighbor, Discrete AdaBoost, and Random Forest classifiers. They experimentally validated their proposed approach on a selection of the LIDC dataset composed of 458 malignant and 107 benign samples. The selected features along with Adaboost algorithm achieved the highest classification results with an accuracy of 82% in predicting malignant nodules, an accuracy of 93% in predicting benign nodules, an AUC of 0.94, an accuracy of 84% and a F-score of 0.87.

Narayanan et a1. [159] proposed a method based on features extracted from nodules from CT scans and given as input to artificial neural networks for classification. Features that have been extracted are the area, perimeter, mean, centroid, irregularity index and eccentricity. The used features are input to a feed forward network. It consists of three layers i.e. an input, one hidden and an output layer. The size of the hidden layer is set to 10. It uses tansigmoid transfer function for both hidden and output layers. Authors tested their algorithm on 279 nodules from the LIDC dataset where 70% of the data is used for training, 15% of the data is used for validation and 15% is used for testing. The overall accuracy of the system was 92.2%.

In later years researchers turned toward texture features for the lung nodules diagnosis task. Their main focus was oriented toward counting the difference in texture between benign and malignant nodules taking advantage of them in the classification process. Knowing that malignant nodules' grow rapidly compared to benign nodules, they concluded that their texture and density are not uniform and that this non-uniformity will

result in variations in the HU values. Some of the works that used texture features only for the lung diagnosis task include those of Huang et al. [160]. They proposed a system to differentiate malignant from benign pulmonary nodules based on fractal texture features from Fractional Brownian Motion (FBM) model. They used for that, 107 CT images obtained from 107 different patients. They achieved an accuracy rate of classification of 83.11% and an AUC of 0.8437 when using the SVM classifier along with the 5-cross-validation validation measure.

Han et al. [161] compared between 3 texture features (Haralick, Gabor and Local Binary Patterns (LBP)) for the lung nodules diagnosis task with the SVM classifier. They used 2D slices from the LIDC dataset to extract 2D features. Since each nodule from the LIDC dataset has been ranked by radiologists with scores going from 1 to 5, with 1 is the score of a most likely benign nodule and 5 for a most likely malignant nodule, they tested their algorithms on 2 different collections where the first collection consider a nodule of score 3 as a malignant nodule and the second collection consider a nodule of score 3 as a benign nodule. In their experiment the Haralick feature achieved the best classification results with both collections, that's why they extended their study to a 3D plane using 3D extracted Haralick features instead of 2D ones. Using a 3D volume instead of 2D slices improved their results when an appropriate number of direction of computation of Haralick features is found. Over all, the best AUC results they obtained when comparing the three different features and when comparing 2D and 3D Haralick features was 92.70% using the second collection.

Other CAD systems include those of Wang et al. [162] who used extracted nodules' Haralick texture features from CT scans and utilized SVM, Extreme Learning Machine (ELM), Multilayer Perceptron (MLP), and Probabilistic Neural Network (PNN) methods for classification. Since ELM gave the best classification results over MLP, PNN and SVM, authors generalized their method by developing a pulmonary nodules computer aided diagnosis algorithm based on semi-supervised ELM (SS-ELM). Their method allowed both

labeled and unlabeled classes to be for training. Their idea was to evaluate a system that provides a solution that allows the use of uncertain class data and ameliorate the testing accuracy of both benign and malignant classes. They tested their algorithm on 1439 sets of thoracic CT images from the LIDC dataset and proved that SS-ELM achieve better classification results comparing to previously introduced algorithms with an accuracy of 97%, a sensitivity of 97.3% and a specificity of 95%.

Nishio et al. [163] used a variant of the Local Binary Pattern features to classify lung nodules. They tested their algorithm using the SVM and XGBoost classifiers. Parameters for both used classification algorithms was optimized using Tree Parzen Estimator (TPE). Authors tested their algorithm on 99 lung nodules (62 lung cancers and 37 benign lung nodules) selected from publicly available datasets using the Leave-one-out cross-validation evaluation technique. AUC values was computed 10 times and the average was reported. The best averaged AUC of SVM and XGBoost was 0.850 and 0.896 respectively. Authors reported AUC values of two board-certified radiologists on the same data that are: 0.898 and 0.822 and proved that their algorithm achieved comparable results.

The CAD system implemented by Arulmurugan et al. [164] was based on Wavelet features and Artificial Neural Networks. They computed Entropy, Autocorrelation, Energy and Contrast after applying wavelet transform and input them to the Neural Network classifier. Authors designed their network based on training functions (Traingdm, Traingd, Traingda, and Traingdx). They used feed forward back propagation network and feed forward neural network in their framework and proved that feed forward back propagation neural network achieved better results than feed forward. Their system achieved a mean square error of 0.978, a sensitivity of 91.2%, a specificity of 100% and an accuracy of 92.6%.

Safta et al. [165] proposed a Multiple Instance Learning approach without predefined regions of interest for lung nodules classification on samples from the LIDC dataset. In their work LBP and GLCM features have been extracted from volumes of different sizes

(instances) surrounding the center of mass of each nodule then assembled into the same bag. These bags of features are then input to the SVM for Multiple-Instance Learning classifier. Authors tested their algorithm on a total of 371 nodules (275 benign and 96 malignant nodules) using the 5-cross-validation technique and proved that their technique improved the results over SVM classifier applied on the delineated groundtruth of samples as a Single Instance Learning technique. This method achieved an accuracy of 91.11%, an AUC of 0.9696, a specificity of 98.55% and a sensitivity of 69.79%. In their future work [166] they extended the number of used samples to 435 (225 malignant and 210 benign nodules) from the same dataset to overcome the unbalanced data issue they encountered in their previous work. They applied the GLCM feature as input to the SVM for Multiple-Instance Learning classifier using the same technique they used in [165]. Similarly to their previous work they proved that their method is efficient for the lung nodules classification task where they beat the results of Single Instance Learning methods. They achieved an AUC, Specificity, Sensitivity and Accuracy of: 0.9767, 95.24%, 91.11% and 93.10% respectively.

Rodrigues et al. [167] developed a novel structural co-occurrence matrix (SCM)-based approach to classify nodules into both malignant or benign nodules and their malignancy levels. They created eight different configurations after applying SCM on grayscale and Hounsfield unit images with four different filters: sobel, Laplace, Gaussian and mean. They tested their algorithm on 1000 nodules (500 malignant and 500 benign) of the LIDC dataset and classified samples using three different classification algorithms: SVM, k-nearest neighbors and multi-layer perception following two strategies: Classify samples into benign and malignant and classify samples into malignancy levels (1 to 5). They compared their method to four other feature extraction methods: GLCM, LBP, central moments, and statistical moments. Their method gave better classification results over all tested methods, for both studied tasks where it achieved 96.7% for both accuracy and F-Score metrics in the first task, and 74.5% accuracy and 53.2% F-Score in the second.

To take advantage of both characteristics learned from appearance and shape fea-

tures and the difference in texture for both benign and malignant nodules, some researchers turned toward combining both type of features trying to get the most out of this fusion. Some of these CAD systems include those developed by Dhara et al. [168]. In this work, authors segmented nodules using a semi-automated technique which requires only a seed point from the end user. From these segmented samples, they extracted a combination of 2D and 3D shape based features as (sphericity, spiculation, lobulation, area, perimeter, etc), and 2D and 3D texture based features as (GLCM and Histogram of oriented gradients (HoG)) and classified them using SVM. They used to validate their algorithm 891 nodules from the LIDC dataset. Since each nodule from the LIDC dataset have been ranked by radiologists with scores going from 1 to 5 as described in [157], authors decided to compose three different configuration by varying the score of samples that belong to each collection. Configuration 1 consider to be benign nodules that have a score of "1" and "2" and malignant nodules that have a score of "4" and "5", configuration 2 consider to be benign nodules that have a score of "1", "2" and "3" and malignant nodules that have a score of "4" and "5" and configuration 3 consider to be benign nodules that have a score of "1" and "2" and malignant nodules that have a score of "3"."4" and "5". Their system achieved an AUC of 0.9505, a specificity of 86.36% and a sensitivity of 89.73% for configuration 1 that is composed of 279 benign and 263 malignant nodules, an AUC of 0.8822, a specificity of 80.73% and a sensitivity of 82.89% for configuration 2 that is composed of 628 benign and 263 malignant nodules and an AUC of 0.8488, a specificity of 74.91% and a sensitivity of 76.14% for configuration 3 that is composed of 279 benign and 612 malignant nodules.

Other CAD systems include those of Huang et al. [169] who used statistical tests (t-test and p-value) on 374 feature parameters extracted from IBEX (Imaging Biomarker Explorer) to evaluate which features can differentiate between benign and malignant samples. From these features 238 features were found efficient in the classification task with a p-values less than 0.05. They used after that a forward search algorithm to select the best set of features for the classification task which end up choosing a total of 9 features.

They classified their samples based on the selected features using the logistic regression algorithm over 10-fold cross-validation. Their algorithm achieved an accuracy of 79% and an AUC of 0.81.

Gong et al. [170] classified benign and malignant nodules from CT images. They used in their work 243 nodules that were divided into 76 benign, 81 stage I and 86 stage III malignant cases. They did three sets of experiments including for the first one all nodules, the second one benign and stage I malignant nodules and the third one stage III malignant and benign cases. They computed for each experiment 66 3D features including GLCM (gray level co-occurrence matrix), GLRLM (gray level run length matrix), GLSZM (gray level size zone matrix), NGTDM (neighborhood gray tone difference matrix), histogram features as minimum, maximum, mean, median, standard deviation, etc. and shape features as surface area, volume, surface to volume ratio, compactness, etc. Authors compared the classification results for three different classifiers named: SVM, Linear discriminant analysis (LDA) and naive Bayes classifier (NBC) with the leave-one-case-out cross-validation method integrated with the Relief-F feature selection algorithm. They reported results for the 3 classification algorithms for all three experiments. As example, the best classification results were attributed for SVM and LDA classifiers for the second experiment that include stage I malignant samples and all benign nodules with an AUC of 0.91. Similarly, for the second experiment too, they compared the overall classification accuracy and sensitivity scores generated by all classifiers under two specificity values of 80% and 90%. The LDA algorithm achieved the best sensitivity results with 86.42% and accuracy of 83.44% for a specificity of 80% and both SVM and NBC achieved the best sensitivity results with 80.25% and accuracy of 84.71% for a specificity of 90%.

Tu et al. [171] applied radiomics features and machine learning classification mechanics for lung nodule diagnosis. In their study, they used a total of 122 nodules (48 benign and 74 malignant) from which 374 radiomics features including shape, intensity-direct, intensity-histogram, intensity-histogram Gauss fit, graylevel co-occurrence matrix

and neighbor intensity difference have been extracted. They tested their method with multiple classifiers as logistic regression, Sequential Minimal Optimization (SMO), J48 decision tree, random forest, and IBK from the Waikato Environment for Knowledge Analysis free software using the 10-fold cross-validation metric. Based on the the two-tailed t-test and the p-value feature selection approach, they found out that 238 of the total features are useful. These useful features include among them CT density, uniformity, sigma and entropy. Among all tested classification algorithms the best results were achieved by the logistic classifier with an accuracy of 79%, a false positive rate of 0.36, an AUC of 0.80 and a positive predictive value of 0.80.

Some recent works include, besides standard feature extraction and classification techniques, new components to optimize their developed CAD systems. Some of these works include those of Wu et al. [172] who classified lung nodules into benign versus malignant using Random Forest combined with clustering analysis by applying class decomposition and tuning weights based on shape features as lobulation, compactness, gray features as Fourier descriptor and texture features as GLCM. Authors used for their analysis 952 nodules from the LIDC dataset. They tested their algorithm on the same three collections that have been used in [168]. The best classification results have been reached by collection 1 with an AUC of 0.9702, accuracy of 92.37%, specificity of 90.27% and sensitivity of 94.28%.

A fusion framework between PET and CT features has been proposed by Guo et al. [173]. They studied the clinical value of tumor heterogeneity measured with 18 F-FLT as a biomarker for lung cancer diagnosis and staging and compared it with other traditional features. They used in their study the SVM classifier on both features extracted from PET and CT images including heterogeneity. They proved that The heterogeneity measure derived from the 18 F-FLT images succeed to distinguish between benign and early stage malignant nodules and between early stage and advanced stage malignant nodules compared to SUVmean and CT texture that didn't show similar capability. Overall SVM

classifier achieved the best classification results when all features were combined and authors succeed to prove that intra-tumor heterogeneity has promising results when it comes to the diagnosis of different stages of lung cancer.

Dilger et al. [174] developed expanded quantitative CT feature extraction techniques that includes volumetric Laws texture energy measures for the parenchyma and nodule, rubber-band straightening, border descriptors using ray-casting, histogram features characterizing densities, and global lung measurements. They used leave-one-case-out and stepwise forward selection cross-validation and a neural network for classification. When authors applied their algorithm on 50 nodules with the 52 extracted features (8 nodule, 39 parenchymal, and 5 global) results improved. Nodule-only features achieved an AUC of 0.918 including nodules size and an AUC of 0.872 excluding nodule size. Inclusion of the parenchyma features with nodule features improved the results and the algorithm got an AUC of 0.938 comparing to an AUC of 0.932 when including all studied features. Their method confirmed that results could improve when features from parenchyma are included along with nodule features.

Wei et al. [175] proposed a content-based image retrieval (CBIR) scheme to classify nodules using the Mahalanobis distance metric. They looked based on the used distance to the most similar reference nodules for each queried one considering 26 extracted GLCM features. They utilized majority votes after that to predict the likelihood of the queried nodule as benign or malignant. Authors tested their algorithm on 746 balanced cases (375 malignant nodules and 371 benign nodules) from the LIDC dataset. They evaluated the performance of their proposed CBIR scheme using a leave-one-nodule-out method with a classification threshold of 0.5 and achieved a precision, recall and F-score of 0.86, 0.889 and 0.874 respectively for benign nodules and 0.893, 0.866, and 0.879 respectively for malignant nodules. Their further work [176] on the same dataset highlighted a method based on a spectral clustering algorithm to classify nodules using the same GLCM features used in their previous work. They constructed a new Laplacien Matrix by incorporating a regu-

larization term in local kernel regression models (LKRM) to utilize the locally and globally discriminative information between benign and malignant nodules. They proved that their results achieved better results than some unsupervised and supervised algorithms with a precision, recall and F-score of 0.882, 0.825 and 0.853 respectively for benign nodules and 0.837, 0.891, and 0.863 respectively for malignant nodules.

2. Diagnosis of lung nodules based on deep learning algorithms

CAD systems based on deep learning algorithms raised lately because of the noticeable achievements of unsupervised deep learning feature extraction and classification algorithms in diverse domains counting medical imaging. All along the training phase, deep learning framework learns both image features and classifier parameters in order to find the most representative features for the classification task. Most used techniques that have been used for the lung nodules classification task includes multi-view 2D CNN (Convolutional Neural Network) [177], 2D CNN [178] and 3D CNN [179, 180] as being proved efficient in computer vision tasks. Other proposed methods used transferable multi-model ensemble, Residual blocks, transfer learning and Optimal Deep Neural Network.

Some works that include the use of 2D CNN in their methods was introduced by Hua et al. [181] who developed models of a deep belief network and a convolutional neural network (CNN) for the lung nodules classification task. They compared in their work both introduced models with 2 traditional handcrafted features then classification algorithms to highlight the usefulness of deep learning methods in the lung nodules diagnosis task. The first handcrafted method relies on Scale-invariant feature transform (SIFT) and LBP to quantitatively profile a two-dimensional ROI in a nodule. Dimension reduction techniques were applied to reduce the feature and K-nearest neighbor method was then utilized for the classification task. The second handcrafted technique was based on the fractal analysis technique. In this method the fractional Brownian motion model was utilized to estimate the Hurst coefficient, which was proven to be linearly correlated with the fractal dimension,

at a defined neighborhood. At this stage, Five coefficients were computed with respect to the neighborhood radius of 3, 5, 7, 9, and 11, respectively and formed the feature vector. Authors used SVM classifier to separate between benign and malignant samples based on computed features. They tested their deep learning algorithms on 2545 nodules from the LIDC dataset and used the leave one out cross-validation to validate their technique. The training samples were resized to a 32 by 32 box surrounding each nodule and input to both previously cited deep learning algorithms. Their experimental results suggested that deep learning methods could achieve better discriminative results over handcrafted features models in general and that deep belief network is better than CNN for such task where it achieved a sensitivity of 73.4% and a specificity of 82.2%.

Other methods include those of Sun et al [182] who used deep learning algorithms for benign/malignant classification on the LIDC dataset. After rotating and downsampling, they collected $174,412$ samples with 52×52 pixel each and the corresponding ground truth. They designed and implemented 3 deep learning algorithms named by Deep Belief Networks (DBNs), CNN, and Stacked Denoising Autoencoder (SDAE). The performance of deep learning algorithms was compared with a traditional CAD system which was designed with 28 image features and a SVM classifier. Accuracies of CNN, SDAE and DBNs, were 79.76%, 79.29% and 81.19% respectively and accuracy of the traditional CAD was 79.40%, which was lower than CNN and DBN. This proved that their deep learning models achieved better performance than traditional models.

Song et al [183] developed 3 types of deep neural networks (eg, CNN, Deep Neural Network(DNN), and Stacked Autoencoder (SAE)) for lung cancer classification. All three proposed models are trained on 28×28 image patches where the nodule is located in the center. CNN network is formed by two convolution layers with 32 filters and kernel size 5 followed by 2 pooling layers of CNN network with kernel size of 2. The DNN is formed by fully connected layers. The 28×28 input image is mapped into 7841. The second layer is a fully connected layer of 512×1. The third layer is a fully connected layer of 256×1,

followed by a dropout layer, with a parameter of 0.6, in which the unit will be hidden in 40%. The fourth and last layer is a fully connected layer of 64×1 with a RELU activation function. Similarly to DNN, SAE is formed by 3 fully connected layers followed by a softmax layer. Authors evaluated those networks on 4581 nodules from the LIDC dataset divided into 2265 benign and 2311 malignant over 10-cross-validation. The experimental results showed that the CNN network reached the best performance with an accuracy of 84.15%, sensitivity of 83.96%, and specificity of 84.32%.

De et al. [184] used image processing and pattern recognition techniques to separate between benign and malignant nodules by studying their patterns. They employed in their work standardized and index basic taxic weights followed by a convolutional neural network for the classification process. The CNN architecture is composed of two convolutional and two pooling layers intercalated, and finally a fully connected layer. Authors tested their methodology on an unbalanced data from the LIDC dataset composed of $50,580$ nodule ($36,396$ benign and $14,184$ malignant). They showed that their method is efficient for the lung nodule diagnosis task and achieved a sensitivity of 90.7%, an AUC of 0.934, an accuracy of 92.63% and a specificity of 93.47%.

An other CAD system that uses 2D CNN was proposed by Lin et al. [185] along with Taguchi parametric optimization for lung cancer classification. They improved their results by using the Taguchi parametric eight control factors and 36 experiments of mixed levels to find out the best parameters that fits the classification task. Their results improved when using the Taguchi parameter optimization comparing to the original 2D CNN only without optimization parameters on the LIDC dataset and on other dataset from the International Society for Optics and Photonics with the support of the American Association of Physicists in Medicine (SPIE-AAPM). Authors proved the efficiency of their method when comparing between the accuracy of 2D CNN with Taguchi parameter optimization and the original 2D CNN. Their algorithm achieved an accuracy of 98.83% and 2D CNN achieved an accuracy of 91.97% when tested on the LIDC dataset compared to an accuracy

of 99.97% and 94.68% respectively for the SPIE-AAPM dataset.

Suresh et al. [186] proposed a CNN architecture for the classification task. The architecture is composed of eight layers and three sub-sampling layers intercepted with ReLu, batch normalization, and max-pooling for efficient feature extraction, and one fully connected layer with softmax function connected to 3 neurons as output layer. They used 5188 images from the LIDC dataset to test their algorithm where images were pre-processed and patches surrounding nodules of 52×52 pixels were extracted and augmented using transformations such as rotation and translation. Along with the CNN architecture, they generated additional images with similar characteristics as pulmonary nodules to augment their data by generative adversarial networks (GANs). When authors validated their algorithm over 10-fold cross-validation, they achieved an accuracy of 93.9%, an average sensitivity of 93.4%, an average specificity of 93% and an AUC of 0.934.

Some researchers tried to overcome the inefficiency of 2D CNN for their lake of exploiting the information attached to the 3D plane while keeping an architecture based on 2D CNN. For that, some of them combined features from in between layers to enhance the diagnosis results, while others turned toward extracting features from intersecting 2D planes for the same nodule. Some of these works were proposed by Shen et al [178], who focused on modeling raw nodule patches without any prior definition of nodule morphology. They proposed a hierarchical learning framework based on Multi-scale Convolutional Neural Networks (MCNN) to capture nodule heterogeneity by extracting discriminative features from alternating stacked layers. Their framework uses multi-scale nodule patches to learn a set of known features simultaneously by concatenating response neuron activations gotten at the last layer from each input scale. Authors tested their algorithm on 880 benign and 495 malignant nodules, and achieved an accuracy of 86.84% over 5 cross-validation. In their future work [187], they oriented their research into implementing a Multi-crop Convolutional Neural Network (MC-CNN) to extract nodule discriminatory features automatically from the raw nodule patches. Their method used a new multi-crop pooling strategy, which

crops different regions from convolutional feature maps, and after that applied max-pooling many times. They tested their algorithm on the same data used in [187] and showed that their method succeed in classifying lung nodules into benign or malignant with an accuracy of 87.14%.

A multiview convolutional neural networks for lung nodule classification (MVCNN) was proposed by Liu et al. [188]. MVCNN handle many views of each nodule unlike the traditional CNN. They used the LIDC dataset (764 benign nodules and 3530 malignant nodules) to tackle the binary classification (benign versus malignant) problem and the ternary classification (benign, primary malignant, and metastatic malignant) and validated their method over 10-fold cross-validation. The results show that, for binary or ternary classifications, the multiview strategy produces higher accuracy than the single view method. Their model achieved an error rate of 5.41% and 13.91% for binary and ternary classifications, respectively. The author used the ROC curve and t-distributed stochastic neighbor embedding algorithm to analyse the model, and concluded that deep features learned by the model have a higher separability than features from the image space and the multi-view strategy that is why results got improved using their strategies.

After studying models based on 2D CNNs, some researchers saw the necessity for architectures that used 3D CNN to emerge. They tried to extend samples and extracted information from them to the 3rd dimension, as it was suggested that single- or multi-view 2D images as used in some methods do not contain a complete 3D information for a lung nodule [179]. Some of these works are introduced by Dey et al. [179], who proposed four two-pathway CNN: basic 3D CNN, a 3D DenseNet, a novel multi-output network, and an augmented 3D DenseNet with multi-outputs. The basic 3D CNN outputs 512 feature maps generated by 3D convolutional filters of size $3 \times 3 \times 3$, and four max pooling layers with filters of size $2 \times 2 \times 1$, each after every two convolutional layers. They used Padding for this structure to maintain the size of feature maps after convolution operators and they applied batch normalization after every convolution layer. The 3D Multi-Output CNN consist

on modifying the basic 3D CNN by introducing early outputs, which provides immediate feedback from an early evaluation of error functions and avoids the algorithm to get stuck in a local optimum. DenseNet structure is formed by dense blocks with direct connections among all the layers in a block. In this architecture, basic 3D CNN is modified by introducing 3D dense blocks. It consists of five dense blocks for each pathway. The first three dense blocks consists of 4, 10, and 20 convolutional layers, respectively. Each convolutional layer has 12 feature maps with 3D filters of size $3 \times 3 \times 3$. The last two dense blocks are formed of 20 layers each and have 24 and 48 feature maps, respectively, which are also generated by 3D convolutional filters of size $3 \times 3 \times 3$. 3D Multi-Output DenseNet (MoDenseNet) adopts the design of the multi-output network to augment the 3D DenseNet. Similarly to the strategy that have been used in the 3D multi-output CNN, in this architecture, outputs are provided after every pooling layer that follows the dense blocks in both pathways and the feature maps before each intermediate outputs are joined along with the features from the last convolutional layers of the two pathways and then sent to the classifier for the final output. The authors evaluated their method on the LIDC dataset by collecting 147 CT scans (37% benign and 63% malignant). The multi-output DenseNet obtained the highest accuracy of 90.40% and an AUC of 0.9548.

A 3D RCNN and U-Net encoder decoder to capture the features of each nodule was designed by Nasrullah et al. [189]. Authors classified nodules using the Gradient Boosting Matching (GBM) with 3D Mixnet. For the classification task, as a first step, volumes of size $32 \times 32 \times 32$ were cropped around the center of mass of each nodule, then a convolutional neural network were used for feature extraction. This group of researchers used 30 3D CMixNet blocks to learn higher-level features and they performed average pooling and used logistic regression to differentiate benign and malignant nodules after two convolutional layers. In a final step, they used GBM on detailed features for classification. They tested their algorithm on 3250 nodules from the LIDC dataset over 10-fold cross-validation and achieved a sensitivity of 94%, a specificity of 90% and an AUC of 0.99.

Polat et al. [190] proposed two CNN-based models: the hybrid 3D CNN with Radial Basis Function (RBF)-based SVM, and Straight 3D CNN with conventional softmax for lung nodules diagnosis. To compare their proposed methods, authors compared their algorithms to well known CNN architectures (3D-AlexNet and 3D-GoogleNet). They proved that both proposed methods achieved better accuracy results over the two well known CNN frameworks and that 3D CNN with Radial Basis Function (RBF)-based SVM achieved the best classification results with an accuracy of 91.81%, precision of 91.91% and sensitivity of 88.53%.

Zhang et al. [191] developed a three-dimensional CNN for both detection and classification of lung nodules into malignant or benign using Open-source datasets (LUNA16, kaggle) and multicenter datasets (data collected from different hospitals) based on pathologically and laboratory proven results. The target of authors in this work is to build a system that can detect and classify both small and large nodules. The nodule cancer diagnostic network simultaneously finds suspicious pulmonary nodules and calculates the probability of detected nodules as being benign or malignant. It combined both nodules detection and classification modalities into one process and proved that it is more effective compared with applying each process alone. They confirmed that their algorithm is efficient for distinguishing nodules with large nodules (10–30 mm) with a sensitivity of 84.4% and a specificity of 83% and that it is efficient in classifying small nodules (≤ 10 mm) with competitive specificity and sensitivity results.

Since deep learning models evolved during the last decade, a lot of new architectures were raised and have been used in many applications. Turning toward these new models has been the objective of some researchers that tried to prove their efficiency in the lung nodules diagnosis task. Some of these works include those of AL-Shabi et al. [192] who proposed a method that fuses between local and global features to predict the malignancy score for the lung nodules diagnosis task. They used Residual Blocks with a 3x3 kernel size to extract local features by applying matrix multiplications between features on

the same feature maps and non-local Blocks to extract global features. They tested their algorithm on the LIDC dataset and excluded from their criteria of selection samples that have been ranked by less than 3 radiologiosts. As a validation technique they used the 10-fold cross-validation, and they achieved an accuracy of 88.46%, a precision of 087.38%, an AUC of 0.9562 and a sensitivity of 88.66%. Nagashima et al. [193] analyzed 73 lung nodules from 60 sets of CT images from the LUNGx Challenge. Their method was based on patch feature extraction using principal component analysis, pooling operations, and image convolution. They compared their method to 3 other systems for the extraction of nodule features: histogram of CT density, 3-dimensional (3D) random local binary pattern, and local binary pattern on 3 orthogonal planes. Their proposed method achieved an AUC of 0.81, the histogram of CT density achieved an AUC of 0.640, the local binary pattern on three orthogonal planes achieved an accuracy of 68.8 and the three-dimensional random local binary pattern achieved an AUC of 0.725. Their results proved that their model captured discriminative characteristics of lung nodules and was effective in distinguishing between both benign and malignant nodules over traditional feature extraction methods then classification.

Kumar et al. [194] used deep features extracted from multilayer autoencoders for the classification of lung nodules. Although they have proved the effectiveness of extracting high-level features from the input data in their experiments, they disregarded the morphological information, for example, perimeter, skewness, and circularity of the nodule, which could not be extracted by the conventional deep models. They used 4303 instances containing 4323 nodules from the LIDC dataset and obtained an accuracy of 75.01%, a sensitivity of 83.35% and a false positive of 0.39/patient over a 10-fold cross-validation.

Other CAD systems include those of Lakshmanaprabu et al. [195] who presented an Optimal Deep Neural Network (ODNN) to classify lung nodules as benign or malignant from CT images. They used the Modified Gravitational Search Algorithm (MGSA) as an optimization framework for the ODNN classifier and Linear Discriminant analy-

sis (LDA) to reduce the dimensionality of extracted features. Extracted features consist of: Histogram features (Variance, Mean, Standard Deviation, Skewness, Kurtosis), texture features (GLCM features) and Wavelet features. They proved that their method is efficient for the studied task after elaborated comparison with other classification algorithms such as: KNN, ANN, RBF, etc and achieved a sensitivity of 96.2%, accuracy of 94.56% and specificity of 94.2% when trained on 70 CT images and tested on 30 CT images.

Transfer learning have been used by Zhang et al. [196] to solve the problem of insufficient samples in the medical domain for the lung nodules classification. They used the LeNet-5 model to classify nodules between benign or malignant and to classify different malignancies of the malignant nodules using the LIDC dataset for validation. They applied the 10- fold cross-validation to test their algorithm on 4927 malignant and 2946 benign nodules and demonstrated the usefulness of transfer learning for such task. Their top accuracies were 97.041% and 96.685% for both malignant versus benign classification and different malignancy stages classification respectively.

Xie et al. [197] utilized the transferable multi-model ensemble (TMME) algorithm to diagnose malignant and benign lung nodules in limited chest CT data. The algorithm transfers the image representation abilities of three ResNet-50 models that they pre-trained on the ImageNet database, to characterize the overall appearance, heterogeneity of shape and heterogeneity of voxel values of lung nodules, respectively. They utilized them to classify pulmonary nodules with an adaptive weighting scheme learned during the error back propagation and validated their work on the LIDC dataset. Experimental results on the proposed TMME algorithm achieved a lung nodule classification accuracy of 93.40%.

De Pinheiro et al. [198] developed different nodule detection and classification models for lung nodules classification based on deep learning and swarm intelligence. They tested seven different swarm intelligence algorithms and convolutional neural networks to see if this approach brings more efficiency than the usual training algorithms, such as back-propagation and gradient descent methods. They proved in their work the efficiency of

swarm trained models over the back-propagation-based models for the lung nodules diagnosis task as three of the seven tested models beat the results of CNN with back propagation. They stated that the best swarm-trained model is 25% faster than the back-propagation model and achieved an accuracy of 93.71%, a precision of 93.53%, a sensitivity of 92.96% and a specificity of 98.52%.

Da Silva et al. [199] developed a combined CNN and genetic algorithm technique to classify lung nodules as benign or malignant on CT scans from the LIDC dataset (1413 malignant and 1830 benign nodules) without computing texture and shape features. Used CNN architectures follow a usual architecture with convolutional layers, fully connected layers, max pooling layers and drop out layers. Since CNN networks with back propagation are used for multiple applications and might not always be effective in some of them, authors in this paper thought that a good way to overcome this dilemmas and develop an effective framework for the lung nodules diagnosis task is to optimize their CNN parameters such as number of filters in the convolutional layers and number of neurons in the MLP using the Genetic algorithm (GA). They achieved a sensitivity of 95.14%, an AUC of 0.949 and an accuracy of 94.78%.

Kalaivani et al. [200] developed a classification framework for lung nodules based on DenseNet and adaptive boosting algorithms. The training and testing of images are done when images are pre-processed and feature extraction and feature selection of images are elaborated. Once training and testing part is over, the CNN algorithm classifies the input lung image either as normal or abnormal and the output will be displayed. They tested their algorithm on 201 lung images where 85% of them were used for training and 15% for testing. Their algorithm achieved an accuracy of 90.85%.

Ren et al. [201] developed a manifold regularized classification deep neural network (MRC-DNN) for the lung nodules classification task encouraged by the fact that real structure among data is often embedded on a low-dimensional manifold. They emphasized that it is expected from the concise manifold representation to reveal important data structure

that could enhance the classification and use regularization that impose natural constraints while the network is training to prevent overfitting. The proposed method achieved an efficient manifold learning with a reconstruction error of 30 HU on 1226 nodules (431 malignant and 795 benign nodules) collected from the LIDC dataset and got an accuracy on testing data of 90% a sensitivity of 81% and a specificity of 95%.

Another CAD system based on an ensemble of 3D Dual Path Networks was developped by Jiang et al. [202]. In a first step they improved the representativeness of deep features by modeling the contextual correlations among adjacent locations when dividing the contextual attention. In a second step, they used a spatial attention mechanism to find the important regions for the nodules classifications. Finally, they improved the prediction efficiency by using several models. They tested their algorithm on 1004 nodules (450 malignant and 554 benign) from the LIDC dataset over 5-fold cross-validation and achieved an accuracy of 90.24%, a sensitivity of 92.04%, a False Positive Rate of 11.06 and an F-score of 90.45.

Shrey et al. [203] introduced a cascaded architecture that segments and classifies lung nodules into benign or malignant. They introduced a segmentation network where they trained their model on a public dataset to identify images that include nodules using transfer learning then classify them. When they validated their system, the authors trained their algorithm on 1186 nodule from the LIDC datset and they tested their algorithm on 204 nodule (102 benign and 102 malignant) from Keimyung University Dongsan Medical Center, South Korea. They achieved an AUC of 0.9567, and an accuracy of 97.96%.

3. Diagnosis of lung nodules based on the fusion of handcrafted and learned features then classification

Deep learning algorithms have been proved to be very efficient in the lung nodule diagnosis task. As nodules doesn't need to be annotated by radiologist, models rely only on 2D patches or 3D volumes surrounding each nodules and classification results are pretty

impressive, researches turned toward them more frequently during the past few years to avoid the consuming time and intensive labor of getting delineated regions by radiologists. Despite this fact few works but still existent that fuses between learned features and traditional handcrafted features emerged as a way to prove that both features combined, having independently their proper advantages could actually be more efficient and increase the diagnosis results. One of these works was proposed by Kim et al. [204] who developed Stacked Denoising AutoEncoder (SDAE) to extract abstract information inherent in raw handcrafted imaging features. At this point, the learned representation is used with the raw imaging features to train the classifier. Their method is based on features augmentation by concatenating output values of the top hidden units of their network along with the original dimensional morphological features. From each nodule, authors extracted 96 morphological features: area, mean Hounsfield Units, standard deviation, mode, min, max, perimeter, circularity diameter, integrated density, median, skewness, kurtosis, raw integrated density, ferret angle, min ferret, aspect, ratio, roundness, solidity, entropy, run length matrix and gray-level co-occurrence matrix. Proposed SDAE is composed from 5 layers with 3 hidden layers. The number units in the three hidden layers were 300, 200, and 100. When training their model they used back propagation algorithm with a mini batch size of 50. Data that have been used to validate their method was collected from 20 patients and Pulmonary nodules were manually segmented by a radiologist. In total, they obtained 178 malignant and $3,420$ benign nodules but used only random 200 benign nodules to balance their data. Beacuse of SDAE, their feature vector have been augmented from 96 to 196 and samples have been classified over 5 cross-validation with an SVM classifier. Using SDAE to obtain global deep features and fusing them with morphological features proved the efficiency of such features in the lung nodule diagnosis task. Authors got an accuracy of 95.5%, a specificity of 96.5%, a sensitivity of 94.4% and an AUC of 0.987 comparing to an accuracy of 93.4%, a specificity of 95.5%, a sensitivity of 91% and an AUC of 0.982 when using morphological features only.

Another group [205] developed a new interpretable deep hierarchical semantic convolutional neural network (HS-CNN) to classify nodules into benign versus malignant, that overcome the lack of interpretability related to traditional deep learning algorithms. Their algorithm provides two levels of output: low-level semantic features, and high-level prediction for each nodule. The low-level output features define the features that are provided by radiologists. The information from low level outputs with the features learned by CNN are then combined and used to outcome the high level output. This architecture learned all the parameters within a joint framework when it is trained to optimize a global loss function including both low- and high-level tasks. Authors used 4352 nodules from the LIDC dataset to validate their framework and compared their results to the 3D CNN algorithm. They showed that the proposed method not only produces interpretable lung cancer predictions, but also achieved better results compared to using a 3D CNN alone with a sensitivity of 070.5%, a specificity of 88.9%, an accuracy of 84.2% and an AUC of 0.856.

Zhang et al. [206] proposed a classification framework based on hybrid features. They fused between LBP-based texture features, HoG-based shape features and 3D deep dual path network (DPN) features for the lung nodules diagnosis task. Authors based their framework on DPN because it is a convolutional neural network that combines the assets of aggregated densely convolutional network (DenseNet) for investigating new features and residual transformations (ResNeXt) for feature re-utilization. They combined it with LBP and HOG in an attempt to improve the classification results. To test their algorithm authors used 1004 nodules from the Lung Nodule Analysis 2016 (LUNA16) dataset and achieved an accuracy of 93.78% and an AUC of 0.9687.

Another CAD system was elaborated by Xie et al. [207] who proposed an algorithm that fuses between shape, deep model-learned information and texture features for lung nodules diagnosis from the LIDC dataset. They used GLCM features as a texture descriptor to extract features for each nodule, a deep convolutional neural network (DCNN) to learn the feature representation of nodules and Fourier shape descriptor as shape features

characterizing each nodule. An AdaBoosted back propagation neural network (BPNN) is then trained with each feature independently and the results are fused at the decision level. They used to test their algorithm the same collections that have been applied in [168]. When authors validated their Fuse-TSD algorithm over 10-fold cross-validation, it achieved an AUC of $.09665$, 0.9445 and 0.8124, respectively for the three tasks.

4. Diagnosis of lung nodules using clinical bio-markers

Detection of lung cancer bio-markers from saliva, urine, blood, and exhaled breath of patients is a developing modality for non-invasive diagnosis. Li et al. [208] demonstrated that genetic deletions of HYAL2, FHIT, and SFTP in saliva can be used as diagnostic markers for non-small cell lung cancer (NSCLC). LRG1 has been proposed as a candidate bio-marker for diagnosis of NSCLC in urine [208]. Oxidative stress produced by the variable redox environment within cancer is thought to increase the production of various volatile organic compounds (VOCs). Hanai et al. [209] used the urinary VOCs to potentially identify lung cancer. Begum et al. [210] identified six genes (APC, CDH1, MGMT, DCC, RASSF1A, and AIM1) in blood which could be used as a bio-marker for lung cancer diagnosis. Antibodies in patient blood has also been proposed as a bio-marker for lung cancer in an early stage [211]. Early diagnosis of lung cancer using quantitative analysis of carbonyl VOCs in exhaled breath has been recently reported [212–216]. Analysis of bio-markers is usually quantitative and inexpensive. However, despite three decades of research and thousands of reports of bio-markers, very few bio-markers have established clinical utility.

5. Summary and discussion

Developing efficient methods for lung cancer classification is very important since it assists radiologists in the diagnosis process and allows them to reduce the intensive labor

and time consuming that this task requires. This chapter summarized an overview of more than 50 articles that addressed the challenges faced by such application. It resumes the current approaches associated with the lung nodules diagnosis task and their sturdiness and limitations. This final section summarize the outlining of the research challenges faced for the lung nodules classification application.

Several challenges and aspects faced the CAD systems for lung cancer diagnosis. These challenges are summarized as follows:

- Some methods depend on the Hounsfield unit (HU) values as the appearance descriptor without taking any spatial interaction into consideration
- Some methods depend on traditional shape features are very sensitive to prior steps, e.g., segmentation which may not always be accurate
- Some methods just depend on raw data and disregard the morphological information
- Deep learning based methods take as input fixed patches or volumes when nodules size may vary significantly from one sample to another. This may not be the optimal method and results may improve if inputs to the models are of different sizes.

CHAPTER III
PROPOSED METHODOLOGY

A. Introduction

This chapter introduces the details of the developed models that are used to generate descriptive and discriminative features from computed tomography (CT) images. These features will be used later for the diagnosis of lung nodules as malignant or benign. The proposed diagnosis methodology is based on a novel framework for the lung nodules classification from chest CT images, that integrates two or more of the CT markers: (*i*) novel appearance models of the lung nodules using 3D histogram of oriented gradient (3D-HOG), 3D spherical sector isosurfaces histogram of gradient (3D-SSIHOG), 3D adjustable local binary pattern (3D-ALBP), 3D Resolved Ambiguity Local Binary Pattern (3D-RALBP), Multi-View Analytical Local Binary Pattern (LBP), and Markov-Gibbs random field (MGRF). (*ii*) novel shape models of the lung nodules using Multi-views Peripheral Sum Curvature Scale Space (PSCSS), spherical harmonic expansion and some basic geometric features. In the following sections, each of these models will be explained in more details.

B. Appearance-based Features

Because of the malignant nodules' rapid growth rate compared to benign nodules, their texture and density are not uniform. This non-uniformity will result in variations in the HU values and will be modeled using different appearance models to capture these irregularities. In this dissertation, different robust and accurate appearance models have

been developed. Details of these appearance models are described below.

1. 3D Histogram of oriented gradients (HOG)

To have a good description for the lung nodules' appearance and to involve the spatial information for the voxel's neighbors in this model, the HOG feature vector is calculated for each nodule to distinguish between benign and malignant nodules. The steps to calculate the 3D HOG are depicted in Figure 9 and described in details below.

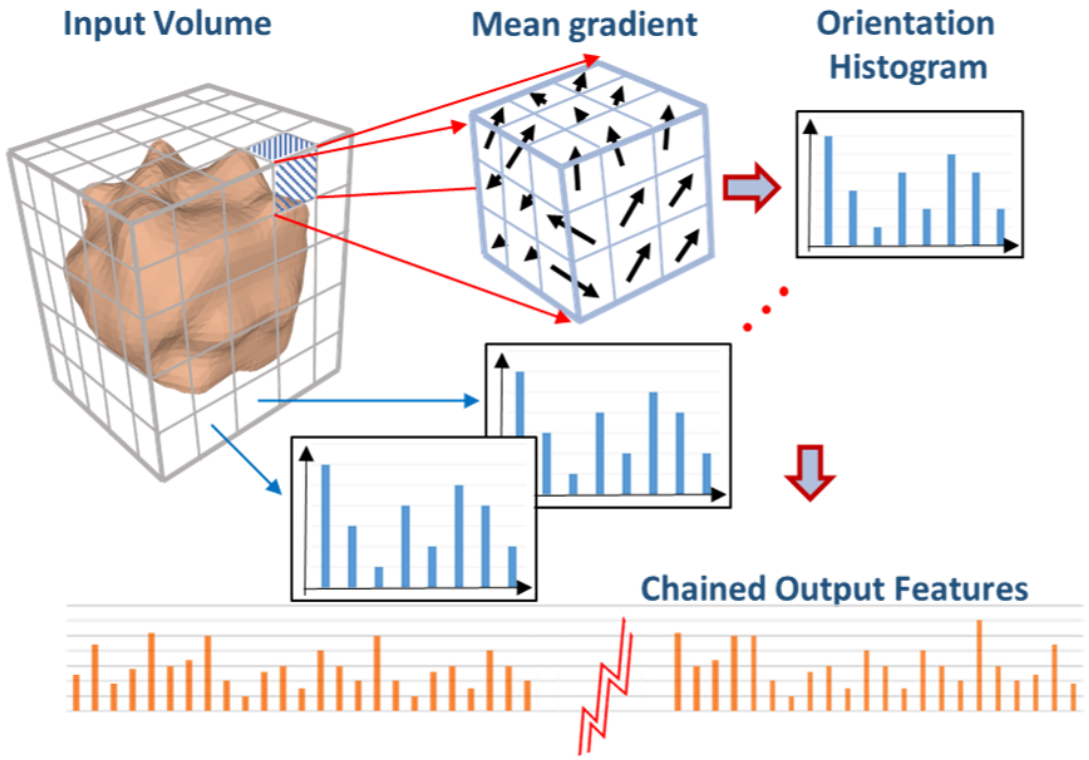

FIGURE 9: 3D Histogram of oriented gradient illustration

a. Mean gradient computation: Gradient computation is the first step of the 3D HOG calculations. It needs to be done in an efficient and rapid way, not only because it is calculated for 3D volumes, but also it is calculated throughout the algorithm many times for different regions and with different dimensions. To overcome these massive repeated calculations a transitional representation is developed for the volume gradient vector that is

called integral gradient volume, which is an evolution for the integral image [217].

The integral gradient volume for a voxel at x, y, z equals the sum of the partial derivative of the up, above, and the left voxels of x, y, z. The values of this gradient vector is calculated using the following equations:

$$\overline{intVol} = (intVol_x, intVol_y, intVol_z) \tag{1}$$

$$intVol_x = \sum_{\acute{x}\leq x,\acute{y}\leq y,\acute{z}\leq z} V_{dx}\left(\acute{x},\acute{y},\acute{z}\right) \tag{2}$$

$$intVol_y = \sum_{\acute{x}\leq x,\acute{y}\leq y,\acute{z}\leq z} V_{dy}\left(\acute{x},\acute{y},\acute{z}\right) \tag{3}$$

$$intVol_z = \sum_{\acute{x}\leq x,\acute{y}\leq y,\acute{z}\leq z} V_{dz}\left(\acute{x},\acute{y},\acute{z}\right) \tag{4}$$

Where V_{dx},V_{dy},V_{dz} denote the partial derivatives with respect to x, y, z, respectively. It is more efficient to be calculated in one pass over the volume gradient vector for V_{dx} using the following recurrences:

$$line(x, y, z) = line(x, y - 1, z) + V_{dx}(x, y, z) \tag{5}$$

$$plan(x, y, z) = plan(x - 1, y, z) + line(x, y, z) \tag{6}$$

$$intVol_x(x, y, z) = intVol_x(x, y, z - 1) + plan(x, y, z) \tag{7}$$

where $line(x, y, z)$ is the accumulative row sum, $plan(x, y, z)$ is the accumulative plan sum, for initialization: $line(x, -1, z) = 0$, $plan(-1, y, z) = 0$, and $intVol_x(x, y, -1) = 0$. After getting the integral gradient volume, to calculate the mean gradient $\overline{\mathbb{G}}$ for any 3D sub-volume Q that is determined by its base point V_1 and its width(W), height(H), and length(L), as shown in Figure 10 (a), it could be used the following equations:

$$\overline{\mathbb{G}} = \overline{D} - \overline{H} \tag{8}$$

$$\overline{D} = \overline{V_8} - \overline{V_6} - \overline{V_7} + \overline{V_5} \tag{9}$$

$$\overline{H} = \overline{V_4} - \overline{V_2} - \overline{V_3} + \overline{V_1} \tag{10}$$

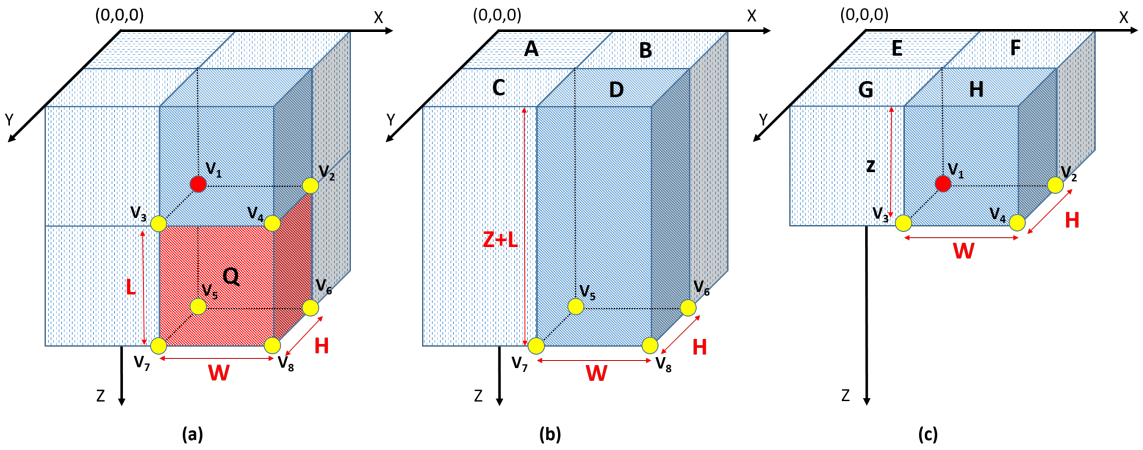

FIGURE 10: Mean gradient computation for a sample sub-volume Q using integral gradient volume.

b. Orientation binning: The next step after calculating the mean gradient is to create the cell orientation histogram. This is done by making each voxel in the cell poll to the direction bins. This poll is weighted based on the gradient magnitude. In 2D, it could be figured out that the histogram channels are divided eventually from 0 to 360 degrees, which could be considered as the directions of the sides of regular polygon or the directions from polygon center to each vertices of it. The number of bins determines the number of the sides in the used polygon. To make the binning process in 3D, a polyhedron is extended from the polygon considering that the direction of each bin is corresponding to the direction of the vector that goes through the polyhedron origin and each of its vertices. A regular and convex polyhedron that is constructed from congruent polygonal faces is used to make the bins eventually divided. Only five polyhedrons meet these criteria, namely: tetrahedron (4 vertices), octahedron (6 vertices), cube (8 vertices), icosahedron (12 vertices), and dodecahedron (20 vertices). The process starts by making resolution for the mean gradient vector $\overline{\mathbb{G}}$ on the axes directed from the origin of the polyhedron and all of its vertices. This resolution is done by the dot product and simplified by matrix multiplication. Let C be the

matrix of vertices coordinates c_1,c_2,...,c_n.

$$C = \begin{pmatrix} c_1 \\ c_2 \\ . \\ . \\ c_n \end{pmatrix}, c_i = (x_i, y_i, z_i) \tag{11}$$

The dodecahedron could be presented by its following 20 vertices coordinates:

$(0, \phi-1, \phi), (-1, 1, -1), (0, \phi-1, -\phi), (1, 1, -1), (0, 1-\phi, \phi), (1, -1, -1), (0, 1-\phi, -\phi),$

$(1, -1, 1), (\phi, 0, \phi-1), (\phi, 0, 1-\phi), (-1, -1, -1), (-\phi, 0, \phi-1), (1, 1, 1), (-\phi, 0, 1-\phi),$

$(\phi-1, \phi, 0), (-1, -1, 1), (\phi-1, -\phi, 0), (-1, 1, 1), (1-\phi, \phi, 0), (1-\phi, -\phi, 0)$

where ϕ is the golden ratio.

The normalized component P of $\overline{\mathbb{G}}$ is calculated as follows:

$$P = \begin{pmatrix} p_1 \\ p_2 \\ . \\ . \\ p_n \end{pmatrix} = \frac{C.\overline{\mathbb{G}}}{\|\overline{\mathbb{G}}\|} \tag{12}$$

Thus, each p_i hold the normalized component of $\overline{\mathbb{G}}$ on axes through the vertex c_i. In order to have the required binning, a thresholding has to be made for the components that are available now in P to meet two criteria: *(i)* each vector has a maximum of three components in the nearest bins, *(ii)* ensure that the aligned vector to an axis has only one bin which is the one that is aligned with. This threshold is determined by getting the component of any axis on the adjoining axes. For all the platonic solids, it will be the same for every one. For the dodecahedron, the threshold was 1.291, and for the icosahedron it was 1.618. After removing the threshold value from each bin with magnitude greater than this threshold and

setting the bins with values less than that threshold to zero, the magnitude of each bin after the normalization could be calculated using the following equation:

$$\tilde{P} = \frac{\left\|\overline{\mathbb{G}}\right\| .P}{\|P\|} \tag{13}$$

In the analysis, the dodecahedron was discovered as the most suitable polyhedron for nodule diagnosis application binning. After getting the histogram, all of these ones could be added for the cells in the same block and normalized to have the histogram of oriented gradient features for each block.

2. 3D Spherical Sector-Isosurface Histgram of Oriented Gradient, (3D-SIHOG)

To describe the nodule's appearance and respect the correlations and patterns of the adjoining voxels, SIHOG was developed to extract descriptive markers that will be utilized in the diagnosis process.

a. Mean gradient computation and spatial configuration: The 3D-SIHOG is implemented to deal with the problems of CT scans, like motion artifacts and quantum mottle, as well as achieving a precise texture appearance modeling. The steps to determine the 3D-SIHOG are depicted in Figure 11 and described in details below. The direction of the gradient in the original HOG is determined by the angle between the gradient and the x axis. This means that if the gradient at certain point P has the direction θ, it will be changed to a new direction $\hat{\theta}$ when the volume is rotated by any angle. This makes the HOG descriptor a rotation variant feature. To overcome this problem, the cartesian coordinate is changed to spherical coordinates. Moreover, using a rectangle window for the detection in the original HOG affects the rotation invariant property of the descriptor, as the final feature vector is obtained by chaining all these features from top to bottom and from left to right. In the proposed SIHOG, the nodule is divided into central isosurfaces and spherical sectors, considering their intersections as a cell to calculate the mean gradient. For isosurfaces, a 3D distance map is used to divide the nodule into a certain number of isosurfaces, and the

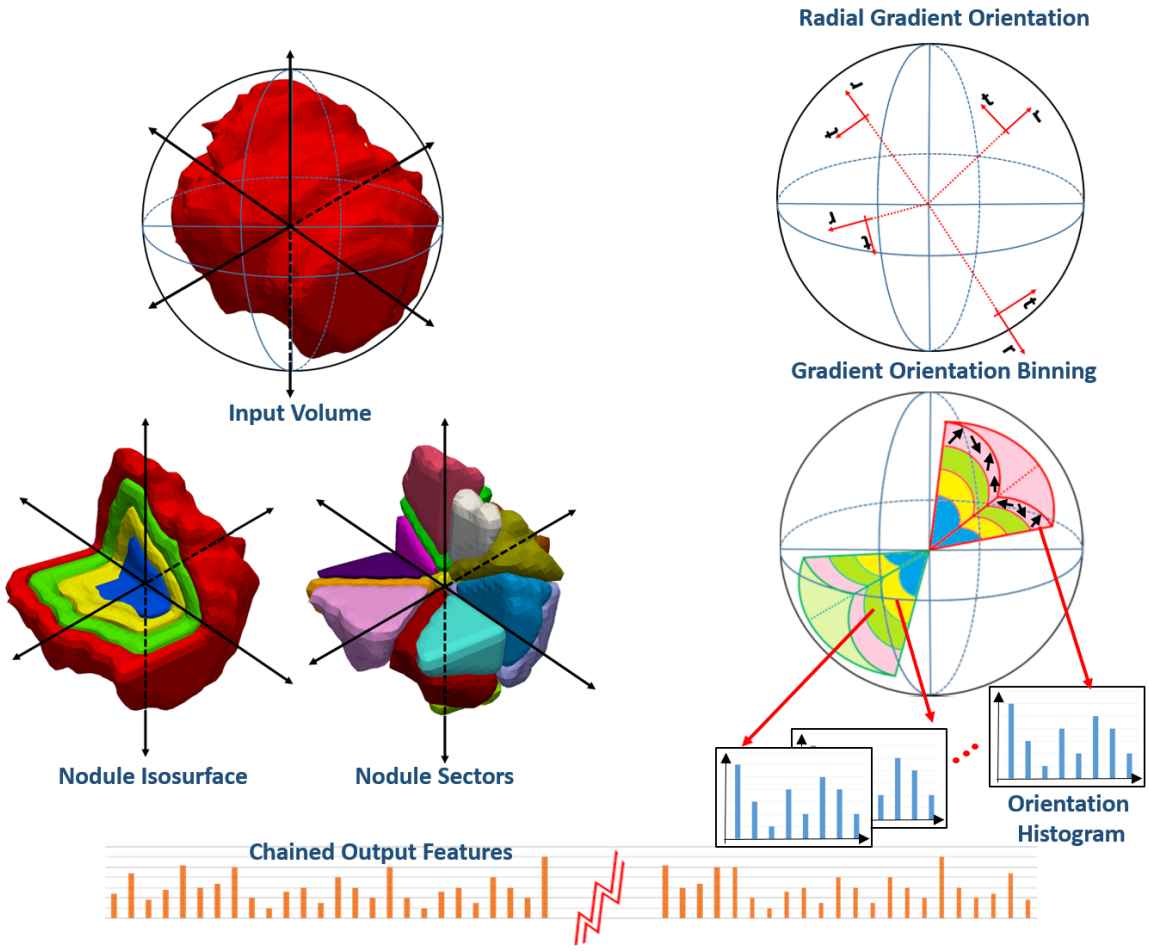

FIGURE 11: Spherical Sector-Isosurface Histogram of Oriented Gradient illustration

sectors' centers is defined on the polyhedron vertices vector directions. The projection of each voxel over the polyhedron vertices decides which sector the voxel belongs to, and based on that, the mean gradient is calculated for the voxels in the same spherical sector and isosurface. In other words, the voxels assigning to cells could be defined as follows:

$$Cell(S, I) = (Voxels \in Sector_S) \cap (Voxels \in Isosurface_I). \tag{14}$$

For rotation invariant, the rotation matrix, R, that aligns the radial direction to the x axis for every voxel is determined to rotate the gradient and get its new direction to allocate it in the binning process. To get R, the unit vector that represents the radial direction of the

vector is calculated, then the reflection function is defined as follows:

$$Ref(A, n) = A - 2n\frac{(n^T A)}{(n^T n)} \tag{15}$$

where A is the matrix being reflected in the hyperplane through the origin, orthogonal to n. Ref could be used to calculate the matrix R that will align the unit vector u to the x axis using this equation:

$$R = Ref(Ref(I, u + v), v) \tag{16}$$

where I is the identity matrix and v is the x axis unit vector. After the inner reflection $Su = -v$ and $Sv = -u$, the outer reflection negates $-v$, giving $v = Ru$.

b. Accumulated histogram of edge directions: This technique is defined by generating a histogram of cell orientation, where every voxel that belongs to a cell votes for an orientation bins. This vote is weighted using the magnitude of the corresponding gradient. The bins of the histogram are partitioned in the range of 360 degrees in 2D. These bins are aligned with the polygon sides' directions and the number of polygon sides is determined by the number of the required bins. The 3D binning is made using a polyhedron that is composed of congruent polygonal faces, in order to generate equally distributed bins. The components of the mean gradient vector $\overline{\mathbb{G}}$ is extracted along the axes of the polyhedron vertices starting from its centroid. These components are obtained by multiplying matrices, where the matrix of vertices coordinates is denoted by

$$C = \begin{pmatrix} c_1 \\ c_2 \\ . \\ . \\ c_n \end{pmatrix}, c_i = (x_i, y_i, z_i) \tag{17}$$

For example, the vertices of a dodecahedron coordinates are:

$(0, \phi{-}1, \phi), (-1, 1, -1), (0, \phi{-}1, -\phi), (1, 1, -1), (0, 1{-}\phi, \phi), (1, -1, -1), (0, 1{-}\phi, -\phi),$

$(1,-1,1),(\phi,0,\phi-1),(\phi,0,1-\phi),(-1,-1,-1),(-\phi,0,\phi-1),(1,1,1),(-\phi,0,1-\phi),$
$(\phi-1,\phi,0),(-1,-1,1),(\phi-1,-\phi,0),(-1,1,1),(1-\phi,\phi,0),(1-\phi,-\phi,0)$

where ϕ is the golden ratio. After using the previous formula to get the components of the gradient, these components need to be thresholded using the unit vector components in the direction of any vertices along any one of the adjoining axes. This thresholding ensures that there is no vector that has more than three components and that the vector that totally aligned to any axis will have only one component along that axis. Finally the feature vector will be built through the following formula :

$$\tilde{P} = \frac{\left\|\overline{\mathbb{G}}\right\| .P}{\|P\|} \tag{18}$$

where P is the normalized components after getting thresholded and could be calculated through the following formula:

$$P = \begin{pmatrix} p_1 \\ p_2 \\ . \\ . \\ p_n \end{pmatrix} = \frac{C.\overline{\mathbb{G}}}{\left\|\overline{\mathbb{G}}\right\|} \tag{19}$$

The experimental study showed that dodecahedron was the most appropriate polyhedron for the suggested binning. The next step is to regroup and normalize all the resulted histograms for the cells in order to obtain the suggested SIHOG features that belong to each block.

3. 3D Adjustable Local Binary Pattern (3D-ALBP)

In order to describe the pulmonary nodule texture, and taking into account the spatial interaction of the surrounding voxels, a novel descriptor 3D-ALBP is developed to identify both malignant and benign nodules through their texture appearance. Each nodule

is represented as a set of 3D-ALBP feature vectors that should be distinguishable between benign and malignant nodules to give a successful classification at the end.

The details of how to get the 3D-ALBP feature vector for each nodule are shown below (Figure 12).

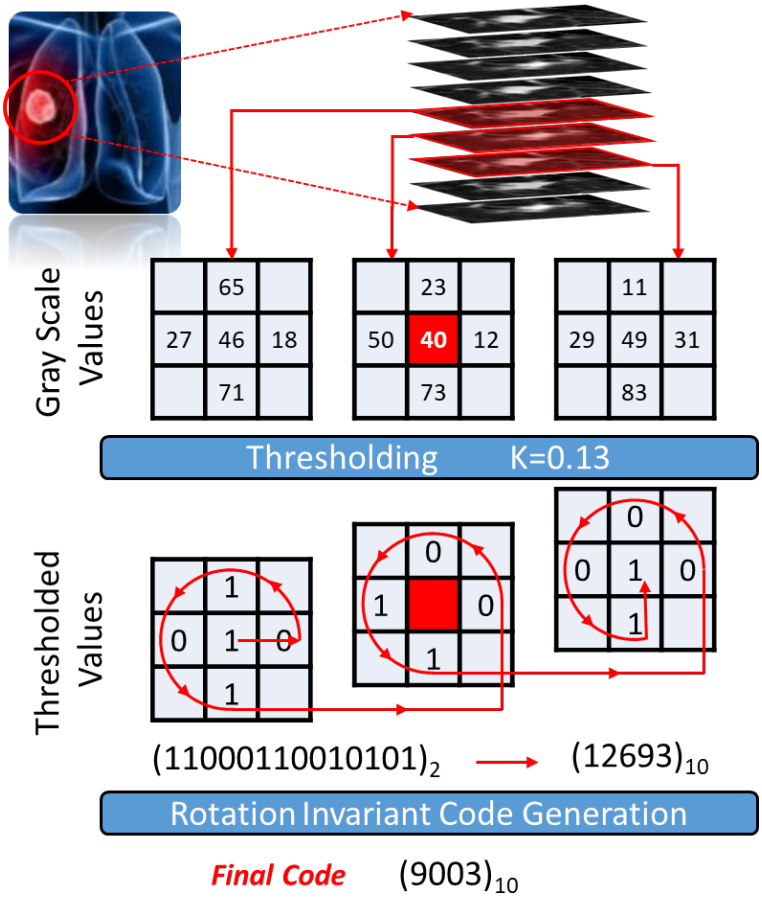

FIGURE 12: 3D-ALBP calculation procedure

a. Original 3D local binary pattern descriptor: Original LBP feature vector is calculated by dividing the image into small cells, then comparing the mid-pixel M of the cell to each of its eight neighbors pixels $P_1, P_2, ...P_8$. where the mid-pixel's value is greater than the neighbors' value, coded "0". Otherwise, coded "1". This procedure results in eight-digit binary code, which will be transformed to decimal to make it easy to represent. Finally, concatenating the code of all cells will result in the feature vector for the

whole image. The following equation shows how to calculate the 2D-LBP code:

$$LBP = \sum_{i=1}^{8} 2^{i-1} * s(P_i - M) \tag{20}$$

where

$$s(x) = \begin{cases} 1 & \text{if } x \geq 0 \\ 0 & otherwise \end{cases} \tag{21}$$

The LBP features vectors could deal with 3D images by taking in to consideration the neighbors' pixels in the upper and lower layers of the candidate cell.

b. 3D-Adjustable LBP: In CT scans, inherited challenges such as noise, partial volume effect, and blurring in addition to low quality of some CT scanner machines are the most important factors that affect the anatomical and pathological structure visualization and processing. All these factors make the usage of the 3D-LBP descriptor in its original version not acceptable because of its rigid inspection for the surrounding voxels which will result in defects in the following situations:

(i) If a minute blur or noise affects the surrounding voxels in a regular texture appearance of benign nodules, the 3D-LBP will set different codes for each voxel (some of them are assigned to "0" and some of them to "1"). This will lead to an unstable attitude for the LBP descriptor and make it inappropriate for this medical application.

(ii) In the situation of having a mid-Voxel with HU value such as 200 that have two neighbors voxels with HU values of 202 and 400, the 3D-LBP will assign the code "1" for both of them. This will lose the information that one of them is just greater than the mid-voxel and the other one is much greater than the mid-voxel.

In order to beat these defects, a modified 3D-LBP is developed based on a threshold ψ as following:

$$LBP = \sum_{i=1}^{26} 2^{i-1} * s(P_i - M) \tag{22}$$

where

$$s(x) = \begin{cases} 1 & \text{if } x \geq \psi \\ 0 & otherwise \end{cases} \tag{23}$$

Modifying the original 3D-LBP, using the threshold ψ, makes the 3D-LBP more robust to blurring and noise, and helps to solve the instability that could be caused by the small changes in the HU values in the case of benign nodules. The problem that was raised after modifying the 3D-LBP equation is the suitable value that should be assigned to the threshold ψ. Assigning a fixed value for the threshold ψ, disregarding how much that value is, will result in an inapplicable solution. For example, if the mid-voxel value is 300, while the surrounding voxel value is 310, assigning the threshold ψ a value of 10 will lead to set the code of that voxel to "1". Also, if the mid-voxel value is 10, while a surrounding voxel value is 20, in case the same threshold ψ is used with value 10, that also will lead to set the code for that voxel to "1". Maybe the difference between the voxels' values are exactly the same value, but the two examples are not identical. The differences in the first example are not notable compared with the mid-voxel value but it is not the case in the second example. This problem will lead us to an important question which is: what is the "just noticeable difference"? The just noticeable difference in psychology could be referred to the minimal simulation level that a person can distinguish 50 percent of the time. As an example, if a person is asked to carry two different objects with two different weights, the minimal difference in weight between both objects that the person could discern half of the time is what is called the just noticeable difference. Weber-Fechner's Law [218], advocates that the just noticeable difference is used in an expanded diversity of senses such as : hear, touch, smell, sight and taste and could be applied to many things such as: sweetness , noisiness, weight, brightness and pressure among other things. The previously described law states that the just noticeable difference is a constant proportion of the original stimulus. In lung nodule diagnosis application, this law could be used by dealing with the original stimulus is the gray level of the HU value for the mid-voxel and the change in the stimulus is the

adjustable threshold ψ. So the threshold that is used could be defined as follows: $\psi = M * k$ where k is the Weber fraction. Utilizing Weber-Fechner's Law for setting the threshold ψ for each mid-voxel value will make the descriptor very perceptive to the notable differences. The effect of changing the Weber fraction will be discussed in details in the experimental result section.

c. Achieving Rotation Invariance: Although the 3D-LBP efficiently captures the texture appearance of the pulmonary nodules, it is not rotation invariant. In other words, if two nodules have the same texture appearance but one of them is rotated, each one of them will have a various signature code which will direct to inexact diagnosis in the classification process. In order to map the signatures that have the same appearance texture to the same bin in the histogram, all the possible shifting for the binary code are checked, from all these possible codes, that get produced from the shifting. The minimum one of them is selected to be the representative bin of that code in the histogram. Because the system input is 3D volumes for the pulmonary nodules, each layer in the z direction is shifted separately then combined together with respect to their weight to get the minimum code. The following formula show how the histogram bin, that the code will be mapped to finally, could be decided.

$$RI - Bin = min\{B_0 + \sum_{l=1}^{3} CLS(D_l, i) * 2^{1+(l-1)*4} + B_{13} * 2^{13}\}, \forall i = 0, 1, 2, 3 \quad (24)$$

where D_l is the decimal code for the bits in the layer l, and $CLS(D, i)$ is a circular left shift function for the number D i times when represented in binary on 4-bit. For example, suppose that the following bin codes that come out after applying the 3D-ALBP: $(10001100101011)_2$, $(10010001110101)_2$, $(10100011001011)_2$, and $(11000110010101)_2$, all these codes should go originally for the bins: 9003, 9333, 10443, and 12693 respectively, although when the developed rotation invariant scheme is applied, for the original bin codes, it could be figured out that all of that binary codes will be assigned to bin 9003 which is the minimum one.

4. 3D Resolved Ambiguity Local Binary Pattern (3D-RALBP)

The RALBP feature vector is introduced as another way for the enhancement of the original LBP, and calculated it for each nodule to classify. The 3D-RALBP is developed to handle the inherited challenges in the CT scans, e.g., noise, and artifacts, in addition to achieving an accurate modeling of the nodule appearance. The steps to calculate the 3D RALBP could be divided into the following steps which are depicted in Figure 13 and will be described below.

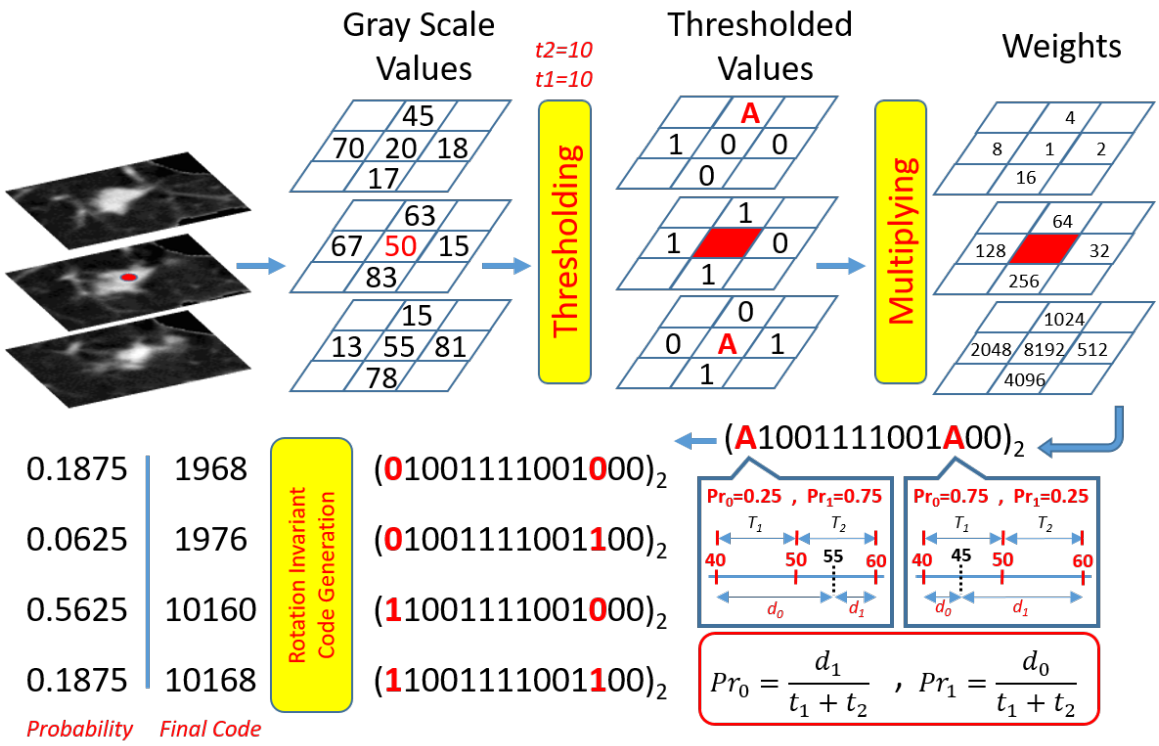

FIGURE 13: 3D Resolved Ambiguity LBP code Calculation

a. 3D Resolved Ambiguity LBP: To avoid the aforementioned problems, two thresholds were added, t_1 and t_2, to be the lower bound of the differences of the voxels that will assign 0 and 1 respectively, in addition to an ambiguous state, a, which is assigned to the voxels that are not either 0 or 1, which changes the condition for The original LBP equation to be as follows:

$$RALBP_{N,R} = \sum_{i=1}^{N} 2^{i-1} * f(g_p - c) \tag{25}$$

where

$$f(x) = \begin{cases} 1 & \text{if } x \geq t_2 \\ a & \text{if } -t_1 < x < t_2 \\ 0 & \text{if } x \leq -t_1 \end{cases} \tag{26}$$

These two thresholds, t_1 and t_2, will remove the influence of the noise. The Codes 0 and 1 will serve as two solid codes where the voxel differences are really noticeable whether negative or positive where it is not applicable to be changed from 1 to 0 or from 0 to 1 because of the noises. Code a serves as an ambiguous code where the voxel difference is not noticeable, which makes it very sensitive to the noise that could change the difference sign and as a result of that will change the code from either 0 to 1 or vice versa. This new developed coding strategy will make the descriptor less sensitive to the noise. However, the main issue is how to resolve the code ambiguity and transfer it to a solid code. The idea is to assign the ambiguous code into the two solid codes, 0 and 1, taking into account the probability that this code tends to be 0 or 1 using the following equation: $P(0) = \frac{c-g+t_2}{t_1+t_2}$, $P(1) = \frac{g-c+t_1}{t_1+t_2}$ where c is the central voxel value, g is the voxel value, and t_1, t_2 are the lower bound of the differences of the voxels that will assign 0 and 1, respectively. Now, for all ambiguous codes, the different combinations for the solid code will be generated. If there are m bits with an ambiguous code, this will result in 2^m codes and the probability of each code could be calculated by multiplying the used solid code probability. For example, if the code is $(A11000111001A0)$, these two ambiguous codes in bits number 2 and 14 will result in 4 codes, which are (01100011100100),(01100011100110),(11100011100100), and (11100011100110) and the probability of each code could be calculated as follows $P(b_{14} = 0)*P(b_2 = 0)$,$P(b_{14} = 0)*P(b_2 = 1)$,$P(b_{14} = 1)*P(b_2 = 0)$, and $P(b_{14} = 1)*P(b_2 = 1)$ respectively. See Figure 12 for detailed illustration.

b. Rotation invariant 3D LBP: The 3D-RALBP is designed to be a rotation invariant descriptor, to handle the different codes that get generated for the same appearance if rotated, and to avoid the miss-classification in the diagnosis phase that results from this issue. Te idea is to match all the rotated appearances to the same bin in the histogram by trying all the suitable codes by shifting the original one and getting the minimum code and assigning all different shifting combinations to that bin. As the inputs to the system are 3D volumes, the shifting process is done separately to each plane and then get the weighted sum of bits to get the minimum code. This minimum code could be obtained using the following formula.

$$RI - CODE = min\{b_0 + \sum_{l=1}^{3} CRS(X_l, i) * 2^{1+(l-1)m} + b_{N-1} * 2^{N-1}\}, \forall i = 0, 1, ..m-1 \tag{27}$$

where X_l is the decimal representation for the bits in the layer l, m is the number of the neighbors in the same layer, and $CRS(X, i)$ is a circular right shift function for the number X with i times when represented in binary on m-bit.

5. Multi-View Analytical Local Binary Pattern (LBP)

A Multi-view ALBP descriptor is developed to accurately model the nodule texture and to add the spatial datum of the voxel's neighbors. This descriptor is an improvement for the traditional LBP to reduces the noise effect on the CT scans and to give a precise model for the nodule texture.

a. Analytical Local Binary Pattern In order to overcome the mentioned problems, instead of comparing the central pixel to the surrounding neighbors, some information about the distribution of the surrounding pixels' gray levels are computed and compared to the average of theses information, such as: mean, standard deviation, median, maximum, and minimum. The calculations for the feature vector are illustrated in Fig-

ure 14 and could be divided into three phases as follows:

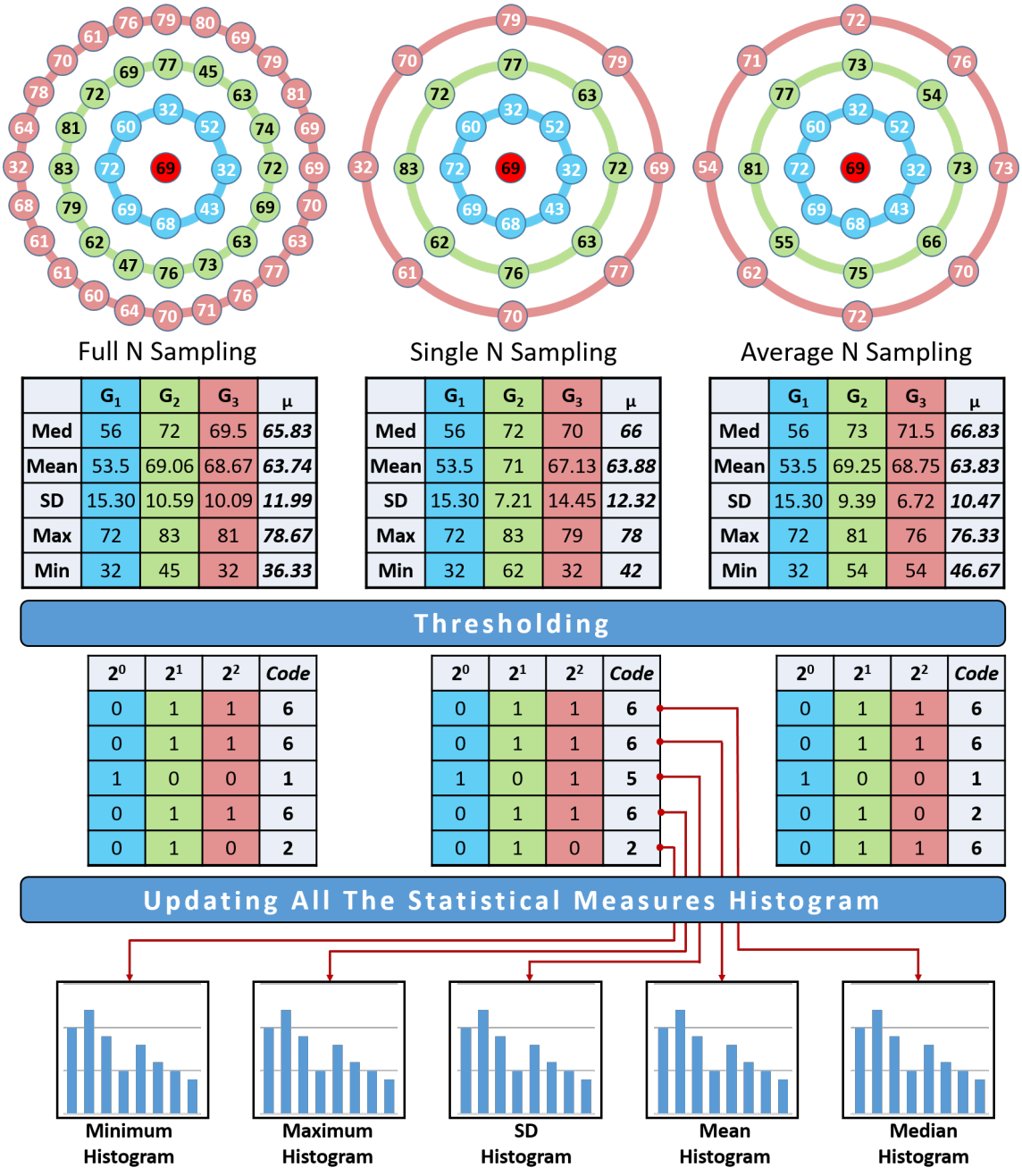

	G_1	G_2	G_3	μ
Med	56	72	69.5	*65.83*
Mean	53.5	69.06	68.67	*63.74*
SD	15.30	10.59	10.09	*11.99*
Max	72	83	81	*78.67*
Min	32	45	32	*36.33*

	G_1	G_2	G_3	μ
Med	56	72	70	*66*
Mean	53.5	71	67.13	*63.88*
SD	15.30	7.21	14.45	*12.32*
Max	72	83	79	*78*
Min	32	62	32	*42*

	G_1	G_2	G_3	μ
Med	56	73	71.5	*66.83*
Mean	53.5	69.25	68.75	*63.83*
SD	15.30	9.39	6.72	*10.47*
Max	72	81	76	*76.33*
Min	32	54	54	*46.67*

2^0	2^1	2^2	*Code*
0	1	1	6
0	1	1	6
1	0	0	1
0	1	1	6
0	1	0	2

2^0	2^1	2^2	*Code*
0	1	1	6
0	1	1	6
1	0	1	5
0	1	1	6
0	1	0	2

2^0	2^1	2^2	*Code*
0	1	1	6
0	1	1	6
1	0	0	1
0	1	0	2
0	1	1	6

FIGURE 14: Different examples for the resampling techniques

(i) Surrounding pixel resampling

To get more information about the surrounding pixels, different levels of neighbor-

hood are involved using different values for the radius R. For each level R, there is a vector G_R that contains all the central pixel neighbors that are evenly distributed on the circle with the specified radius. When the level R increased, more pixels are expected to get involved in the calculation. There are three sampling methodologies that are used to resample the surrounding pixels, namely; full N, single N, and average N (see Figure 15). The full N

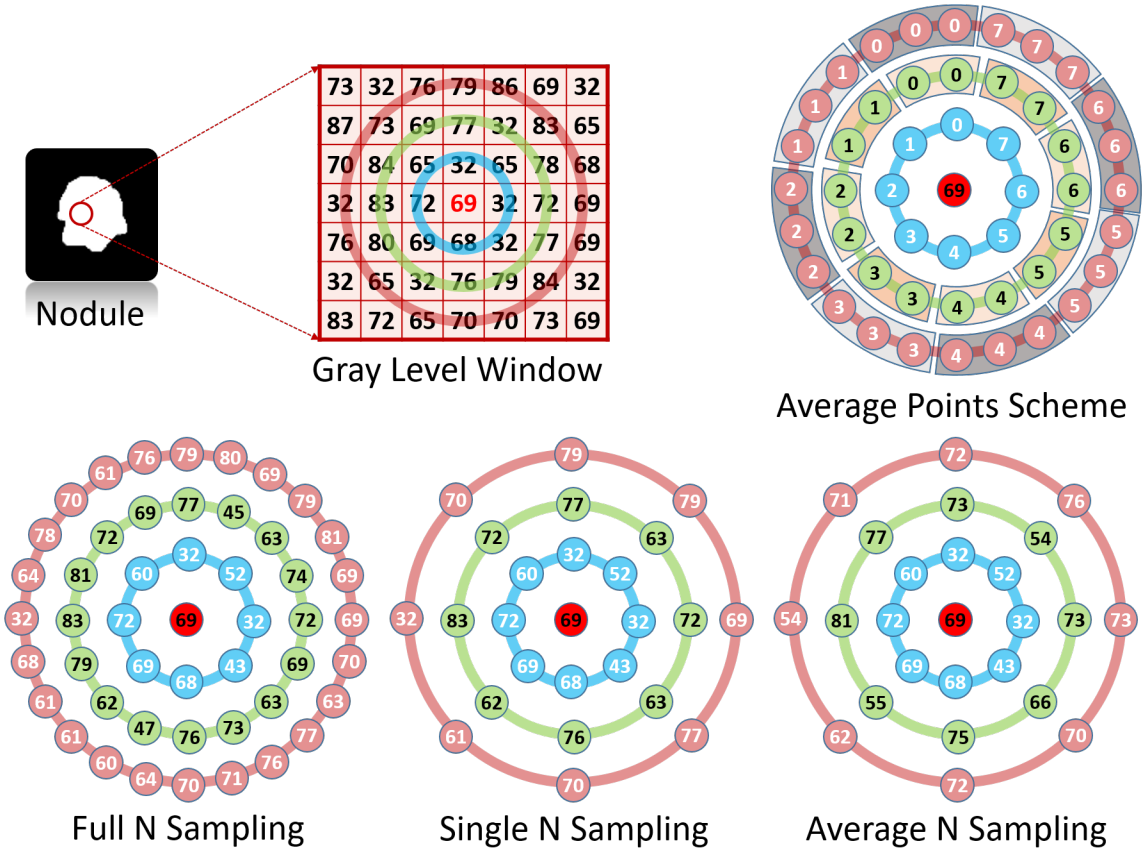

FIGURE 15: Different examples for the resampling techniques

resampling is trying to involve all the points on the circle around the center. Of course, it is impossible to add all the points on the circle, as it is an infinite number. The number of points that will be used in each level will increase with respect to the level number. In the full N resampling, the number of points at any level R will be $8 * R$. In other words, every time the level is increased by one, more 8 points are added. The drawback of this technique

is the huge amount of computations, specially when the R is large and for the points that needs bilinear interpolation. To overcome this issue, the single N resampling technique could be utilized, as it will only involve a fixed number of pixels (8 pixels on each level regardless of the R). This technique will solve the problem of the computation cost but will lose a lot of data, especially for the large values of R. To overcome this issue and to compromise between the previous two techniques, an average N resampling could be used. Average N resampling uses all the pixels and calculate the average to 8 sets of the pixels. This technique allow us to use the complete available data and reduce them to the same number of the single N resampling. All these resampling techniques are experimented and compared together to obtain the highest classification accuracy.

(ii) Gray level distribution analysis

Adding more than one level of pixels will increase the dimensionality. So, there is a real need to reduce it without losing any texture information. The statistical analysis of the gray level distribution will reduce the dimensionality after taking into account the whole information and present it in a way that make it easy to analyze. The median value that separates the largest half from the smallest half is one of the used measures. The main disadvantage of that measure is not taking into account the whole data (the median value will remain the same regardless the increase of the highest value or the decrease of the lowest value). So, more measures need to be added like the mean, which indicates the data average and the standard deviation that shows how much the data differs from the average. The maximum and minimum has been also added to the list of the statistical measure that is calculated for the gray level of the neighborhood pixels. All these measures will give a summarized information about the gray level distribution that will enable to distinguish between the homogeneous texture and nonhomogeneous one that characterize the benign and malignant nodules respectively. For every level R, a set of the mentioned statistical measures are calculated for the vector G_R. This representation reduces the dimensionality from any domain size to $\mathbf{R}^5$. The expected output from this phase is the vectors $\mathbf{D}_R$ for

each level radius R.

(iii) Construction of the feature vector

As mentioned before, the traditional LBP and most of its variations are using the central pixel to threshold the surrounded neighbor pixels. Here, the surrounded pixels gray level are replaced by the distribution analysis measures vector which is calculated from the previous phase. This vector is thresholded using the average of every statistical measure all over the levels. This thresholding vector is denoted by μ and could be calculated using the following equation:

$$\mu = \frac{1}{R} \begin{bmatrix} \sum_{i=1}^{R} Median_i \\ \sum_{i=1}^{R} Mean_i \\ \sum_{i=1}^{R} SD_i \\ \sum_{i=1}^{R} Min_i \\ \sum_{i=1}^{R} Max_i \end{bmatrix} \tag{28}$$

The binary code signature will be calculated for every statistical measure separately and its histogram will be updated separately. For example, the binary code for the mean could be calculated using the following equation:

$$ALBP_R = \sum_{i=1}^{R} 2^{i-1} * f(mean(G_i) - \mu(mean)) \tag{29}$$

where:

$$f(x) = \begin{cases} 1 & \text{if } x \geq 0 \\ 0 & otherwise \end{cases} \tag{30}$$

6. Markov Gibbs Random Field (MGRF)

Malignant nodules, due to their high growth rate, have a non-uniform density (signal non-homogeneity) compared to benign nodules, which is reflected as varying Hounsfield units (HU) in the CT scan. HU is a unit of measure that represents the different density levels of tissues as visualized in the CT images. The appearance analysis is modeled for

the 3D nodule volumes in a way that the differences between the HU of a voxel and its neighbors are represented as Gibbs energy using a 7^{th} order Markov Gibbs Random Field (MGRF). This model tackles the inherited challenges within the CT images that stem from partial volume effect, different acquisition parameters, and scanner types while preserving ordinal signal relations to keep the visual appearance. Besides, the $7^{th}-$ order MGRF model uses the partial ordinal interaction instead of the complete ordinal ones to reduce the cardinality and makes the model more computationally feasible. Grayscale patterns of the nodules are considered as samples of a trainable translation- and contrast-offset-invariant 7^{th}-order MGRF. In this model, the relation between the Gibbs energy, $E_7(g)$, voxel-wise HU, g(r), and an image texture, $g = (g(r) : r \in \mathbb{R})$ in a general-case exponential family distribution as follow:

$$P_z(\mathbf{g}) = \frac{1}{Z}\exp(-\sum_{a=1}^{A}\sum_{\mathbf{c}_{\mathrm{a:r}}\in\mathbb{C}_a}\mathbf{V}_{\mathrm{a}}(g(\mathbf{r}') : \mathbf{r}' \in \mathbf{c}_{a:r}))) \tag{31}$$

Where the Gibbs energy $E_7(g) = \sum_{\mathbf{c}_{\mathrm{a:r}}\in\mathbb{C}_a}\mathbf{V}_{\mathrm{a}}(g(\mathbf{r}') : \mathbf{r}' \in \mathbf{c}_{a:r})$, and the function Z normalizes the distribution over the parent population $Z = \sum_{g\in\mathbb{G}}\exp(-E(\mathbf{g}))$, and the interaction structure is a system, $\mathbb{C}$, of $A, A \geq 1$, clique families, $\mathbb{C}_a$. The origin voxel, $\mathbf{r} \in \mathbb{R}$ and a K-variant Gibbs potential function $\mathbf{V}_a(g(\mathbf{r}') : \mathbf{r}' \in \mathbf{c}_{a:r})$ depends on the ordinal relationships between the origin voxel and the 7 neighbours, $\mathrm{r}' \in \mathbf{c}_{a:\mathrm{r}}; \mathbf{r}' \neq \mathrm{r}$.

The signal interactions is modeled between each voxel and the 7 neighbors at a distance, ρ, from that voxel. The Gibbs potentials of the 7-voxel subsets, are learned from the training nodules, g°, to be used in com putting the energy $E_7(g)$. The learning process uses the maximum likelihood estimates (MLE) that generalize the analytical approximations of the 2^{nd}-order MGRF potentials in [219]:

$$\upsilon_{7:\rho}(\beta) = \frac{F_{7:\rho:core}(\beta) - F_{7:\rho}(\beta : \mathrm{g}^o)}{F_{7:\rho:core}(\beta)\left(1 - F_{7:\rho:core}(\beta)\right)} \; ; \; \beta \in \mathbb{B}_7 \tag{32}$$

Here, β is a coded contrast-offset-invariant relation between the seven signals; $\mathbb{B}_7$ denotes the set of codes for the possible ordinal 7-signal relations; $F_{7:\rho}(\mathrm{g}^o)$ is an empirical marginal probability of the code β ; $\beta \in \mathbb{B}_7$, over all the 7-voxel congurations with the

center-to-voxel distance ρ in g^o, and $F_{7:\rho:core}\,(\beta)$ is the like probability for the core distribution. The computed energy is used as a descriptive feature to discriminate between the malignant and benign nodules (Figure 16).

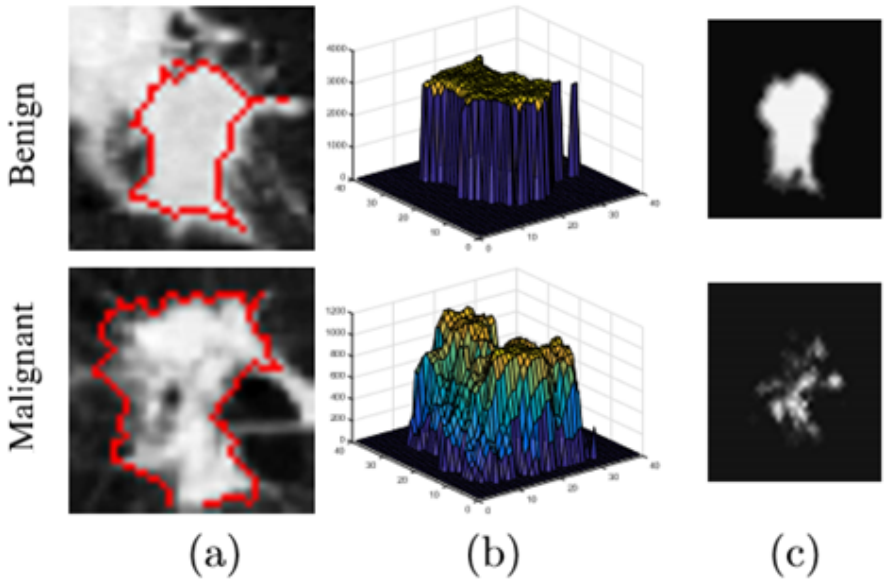

FIGURE 16: A sample of benign (rst) and malignant (second-row) nodules (a), their 3D visualization of HU values (b), and their Gibbs energy which shows high energy for (brighter) for benign and less energy for malignant (darker) (c).

The training nodules, g^o, are used to learn both the potentials and the distance ρ between the central voxel and its neighbors. The output features from the MGRF appearance model is a vector of size 1000 describing the histogram bins of the Gibbs energy for each nodule.

C. Shape-based Features

The pulmonary nodules in general have a spherical shape, but in the case of the malignant nodules (due to its fast growing), it could not keep the original shape of the nodule. This situation leads to a complex shape for the malignant nodule, and will be a

key point for distinguishing between the malignant and benign nodules. Different features are implemented to model the nodule shape and to describe its complexity. Details of these models will be discussed in the following sections.

1. Multi-views Peripheral Sum Curvature Scale Space (PSCSS)

Malignant nodules have a complex shape due to their rapid growth rate and of course the existence of the lobulation compared to benign nodules. This is why the nodules' contour sharpness has a very significant role in the lung nodule diagnosis. The contour sharpness of the nodule is modeled using the developed feature that is called Multi-view PSCSS.

a. Curvature:

The curvature, K, of any curve, C, is defined as

$$K\left(C\right)=\lim_{l\to 0}\frac{\phi}{l}\,, \tag{33}$$

where ϕ is the angle between the tangent vector at the curve point where you want to calculate the curvature and the tangent vector just after this point by distance l (see Figure 17). This is why the curvature shows how fast is the unit tangent vector to the curve rotates. Assume that the Cartesian equation of a plane curve given by the equation $y=f(x)$, the curvature at any point $P(x,y)$ can be calculated using the first and second derivatives of the function $f(x)$ using the following equation:

$$k\left(x\right)=\frac{\frac{\partial^2 y}{\partial x^2}}{\left[1+\left(\frac{\partial y}{\partial x}\right)^2\right]^{\frac{3}{2}}} \tag{34}$$

It is very difficult to have a well defined Cartesian equation for the contour of the nodule. However, it is much easier to have a parametric equation for the contour of the nodules. Let's assume that the parametric equation of a curve is:

$$\Gamma\left(t\right)=\left(x\left(t\right),y\left(t\right)\right), \tag{35}$$

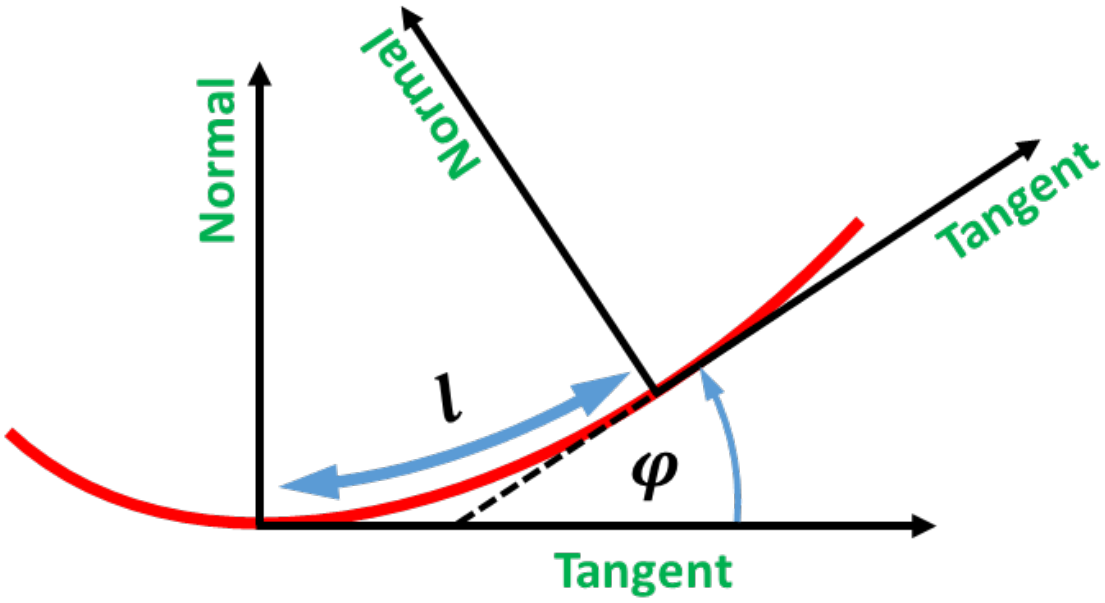

FIGURE 17: Curvature and radius of curvature.

where t is an arbitrary parameter that represent the edge point location, then the curvature of curve $\Gamma(t)$ is derived from the contours points as follows:

$$k(t) = \frac{\frac{\partial x}{\partial t}\frac{\partial^2 y}{\partial t^2} - \frac{\partial^2 x}{\partial t^2}\frac{\partial y}{\partial t}}{\left[\left(\frac{\partial x}{\partial t}\right)^2 + \left(\frac{\partial y}{\partial t}\right)^2\right]^{\frac{3}{2}}} \tag{36}$$

b. The Curvature Scale Space Image:

Extracting the edges of the lung nodule is the first step to get the curvature scale space image. In the used data-set there is a well defined binary mask for each nodule which make the edge detection of the nodule an easy process. There are many algorithms for edge detection that mainly varies in the kind of the used filter for smoothing and the methodology for the edge strength calculation [220]. Different edge detection algorithms were tested, but Canny edge detection algorithm [221] was proved to be the most suitable algorithm to this application. However, this algorithm was implemented with its variations in early days of image processing, it is still a state-of-the-art edge detector. Of course there is some algorithms that works better than Canny algorithms but these ones need very long computation

time comparing with Canny algorithms without a remarkable enhancement. In canny edge detection algorithm, the curve is smoothed by Gaussian kernel with variable width σ. The edge is extracted to each nodule using different Gaussian scale space to guarantee that each edge is much smoother than the one of the previous scale (see Figure 18). It is very obvious that when σ is sufficiently high the nodule edges will turn to be a convex curve. The next

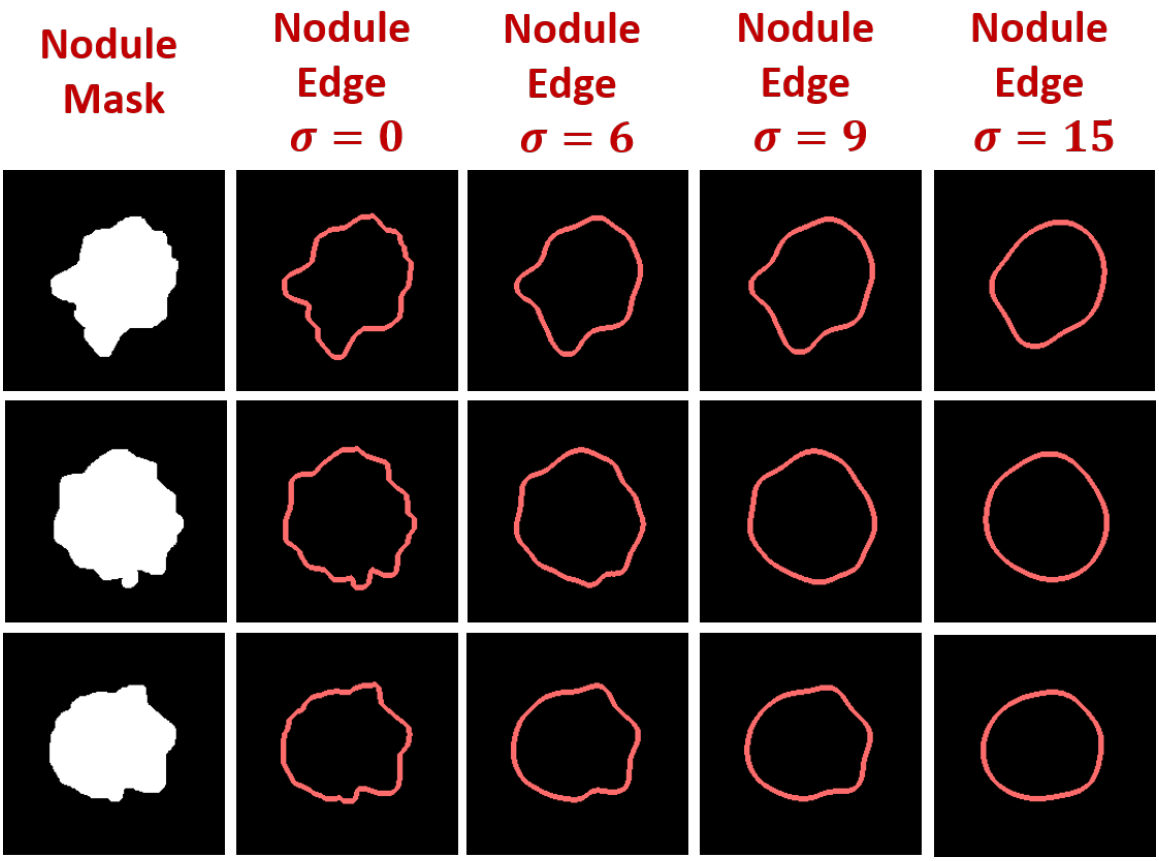

FIGURE 18: Nodules edges at different Gaussian kernel width σ.

step is to go through the edge points in a way that keeps the order of the points along the nodule edge. Then, for each Gaussian scale space (at different degrees), the curvature is computed for each edge using Eq. 36. The curvature calculation at a specific point depends on the points that are just after or before it. This will lead to a very limited and inaccurate curvature as the surrounding pixels can only be one out of eight directions. So, the points

at a certain distance along the contour are used to calculate the curvature (Fig. 19). After calculating the curvature, the interest is not the curvature value, but the points where the curvature changes, which is called the curvature-zero crossings of the edges that describe the shape complexity of the extracted nodule. The curvature-zero crossing happens when the curvature sign changes or crossing the zero line as shown in Figure 19. The curvature function is a rotation invariant as the rotation of the nodule will not affect the surface curvature, but the order of the edge points will vary, which would make the signature of the same nodule vary if it is rotated. To overcome this problem, the suggested peripheral sum (CSS) will correct this by considering the peripheral sums of the nodule CSS signature which makes the algorithm rotation invariant.

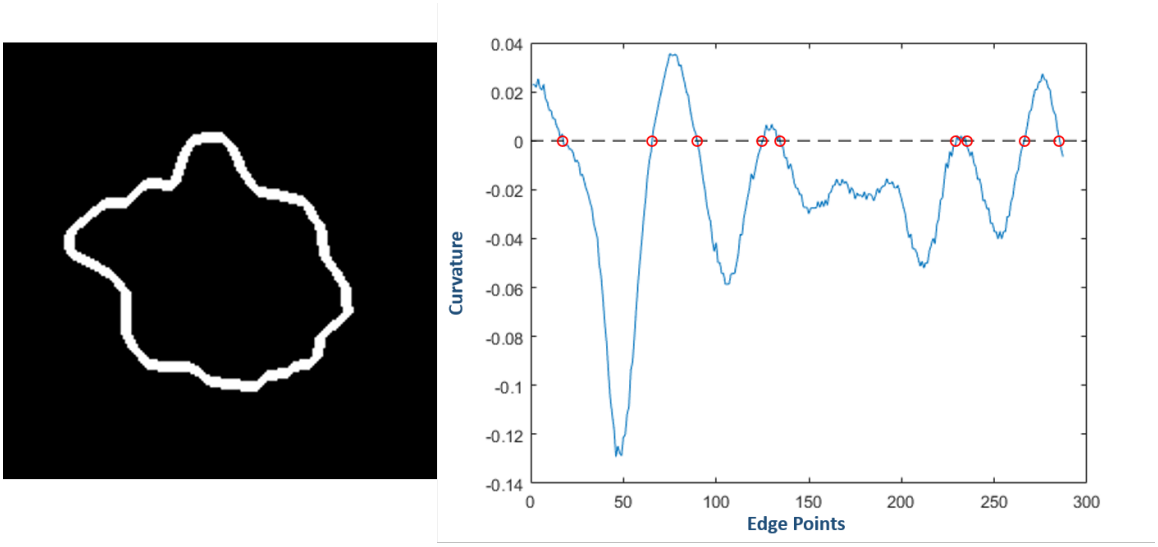

FIGURE 19: Plot of edge curvature of a nodule at zero scale space.

2. Spherical Harmonics

The lung nodules volumes will be reconstructed using Spherical Harmonics analysis to obtain good descriptors related to the shape complexity in order to be used for the classification process between malignant and benign nodules. The spherical harmonics are

periodic functions that described on the sphere surface. It construct a complete set of orthonormal basis, that is why any function defined on the sphere surface can be written as an aggregation of these spherical harmonics. The Spherical Harmonic expansion is considered as a complicated version of Fourier series that express the functions defined on a circle as a sum of sines and cosines. The following subsection shows how the mesh are generated which is the input for the spherical harmonics analysis.

a. Mesh Generation The main requirement to use the Spherical Harmonics analysis is to have a manifold mesh as it can only be applied on a manifold mesh. A mesh in general consists of three types of elements: vertices (the points or the nodes), edges (a contact line between two vertex), and faces (an individual flat surfaces). A mesh is a manifold when it doesn't contain any holes. In other words it satisfies the following two conditions: *(i)* Each edge is incident to only one or two faces. *(ii)* The faces incident to a vertex from a closed or an open fan. Figure 20 shows different examples of manifold and non-manifold meshes. The input binary mask for the nodules is already manifold volume and is ready for the process of mesh generation. TETGEN [222], which is a reliable and rapid software for creating the tetrahedral meshes, is used to generate the lung nodule mesh. This software is implemented for a MATLAB/Octave-based mesh generation toolbox called iso2mesh [223, 224]. This mesh generation system is built on an open source software library called Computer Geometry Algorithms Library (CGAL). The triangulation of this library works by constructing a circumscribing sphere of each cell and successively put triangulation inside this sphere. There is a specific empty sphere property in Delaunay triangulation, which means that every circumscribing sphere shouldn't contain any vertices of any triangulation inside it. These triangulations have a unique definition in general barring the cases where five points are co-spherical. However, the CGAL implementation computes a unique triangulation even in these cases by recomputing the triangulations in the circumscribing sphere. The generated mesh from these procedure is non-rigid with no constrains on the number of the nodes' neighbors. However, the correctly implemented

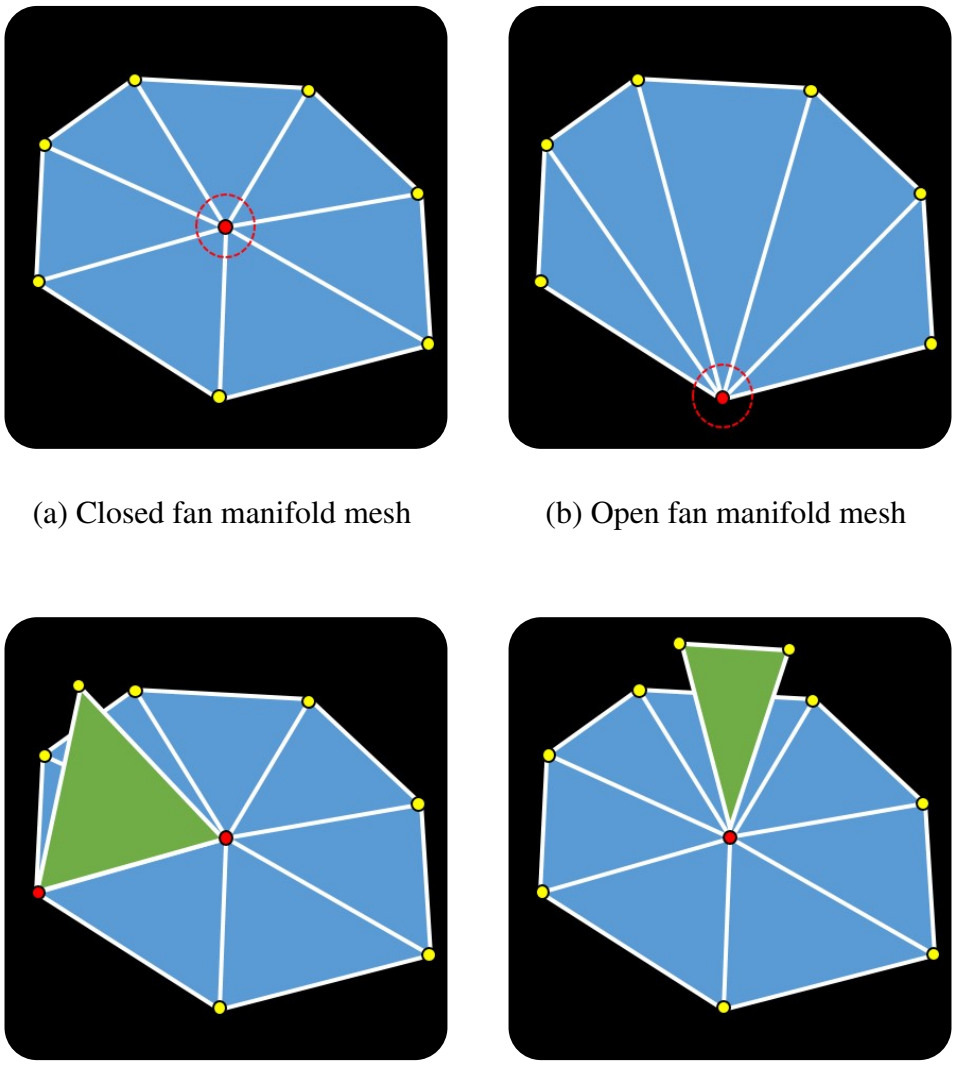

(a) Closed fan manifold mesh

(b) Open fan manifold mesh

(c) Non-manifold mesh

(d) Non-manifold mesh

FIGURE 20: Sample of the different types of meshes: Closed fan manifold mesh (a), open fan manifold mesh (b), and non-manifold mesh (c) and (d).

triangulations nodes must have at least three neighbors and logically three faces with no upper bound for the number of neighbors.When the first mesh is generated, it has to be re-positioned in 3D space and resized (there is no need for resizing in the current case as the used data are preprocessed to be uniformly and isotropic from the beginning). The centroid of the nodule is calculated and used to reposition it so that the center of the mesh coordinates are (0,0,0). The final outputs of mesh generation, which are the nodes coor-

dinates and the faces, are saved on Wavefront object format (see Figure 21). This format

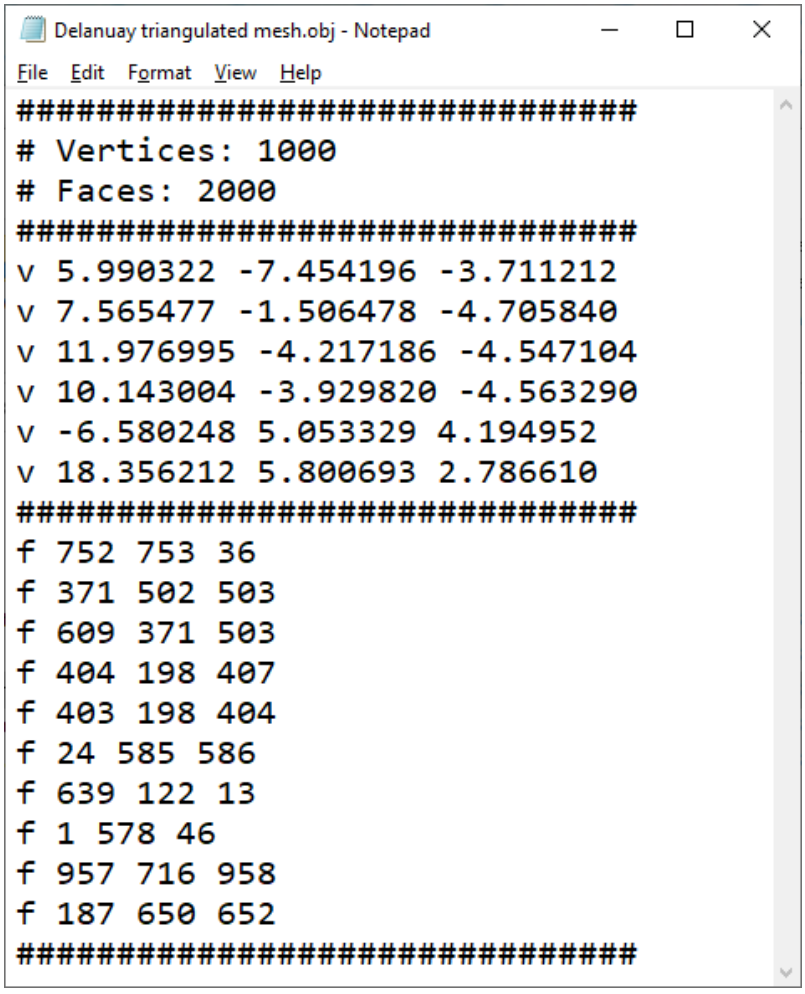

FIGURE 21: Rough outline of part of Wavefront OBJ file format.

is a geometry definition format first developed by Wavefront Technologies. it had a very easy import and export support from most of the computer aided design software, which make it the most dominant format for sharing the 3D models. Also using this format in the developed framework will make the developed algorithm reusable regardless the used method for mesh object generation. The last step before start the spherical deformation for the mesh is the smoothing process. Laplacian smoothing is used for this process to make the mesh more appropriate for the spherical harmonics construction and to keep the spherical shape of the nodule [225]. Laplacian smoothing chooses a new location for each node

in the mesh based on the locations of its adjacent nodes, then move the node to that new location. Specifically, the smoothing equation for a node could be described as:

$$\overline{x}_i = \frac{1}{N}\sum_{j=1}^{N}\overline{x}_j \tag{37}$$

where N is the number of neighbors nodes for node i, $\overline{x}_j$ is the position of the j^{th} neighbor for node i, and $\overline{x}_i$ is the new location for node i. Usually the mesh is smoothed for multiple times before starting the spherical deformation. The number of smoothing times is 1% of the number of the constructing nodes of the mesh.

b. Spherical Deformation Spherical Harmonics plays an important role in describing the nodule shape and its mesh reconstruction. The first step of calculating the Spherical Harmonics is to build the 0^{th} harmonic which is called the base. The nodule mesh deformation into a unit sphere is the main step of constructing the 0^{th} harmonic. The "Attraction-Repulsion" approach is utilized to deform the mesh into the unit sphere mesh and figure 22 Shows a 2D illustration of the re-positioning done by that algorithm. The unit sphere mesh has to satisfy the following conditions: *(i)* the distances between each vertex and its neighbors have to be equal. *(ii)* the distances between each vertex and the nodule mesh centroid have to be the unit distance. The Attraction-Repulsion algorithm consists of two main steps. The first one is the attraction step, which is responsible for centering each vertex location between its neighbors by regulating its position in an iterative manner using the following equation:

$$\mathbf{V}'_{\alpha,i} = \mathbf{V}_{\alpha,i} + C_{\mathbf{A},1}\sum_{j=1;j\neq i}^{J}\Delta_{\alpha,ji}d^2_{\alpha,ji} + C_{\mathbf{A},2}\frac{\Delta_{\alpha,ji}}{d_{\alpha,ji}} \tag{38}$$

where α denote the index of the iteration, $\mathbf{V}_{\alpha,i}$ denote the Cartesian coordinates of the i^{th} node at the α^{th} iteration, J denote the number of node's neighbors, $d_{\alpha,ji}$ denote the Euclidean distance between node i and node j at the iteration α, $\Delta_{\alpha,ji}$ denote the displacement between node j and node i at the iteration α, $C_{\mathbf{A},1}$, $C_{\mathbf{A},2}$ are the attraction constants that regulate the nodes displacement. The second step is the repulsion step, which is responsible

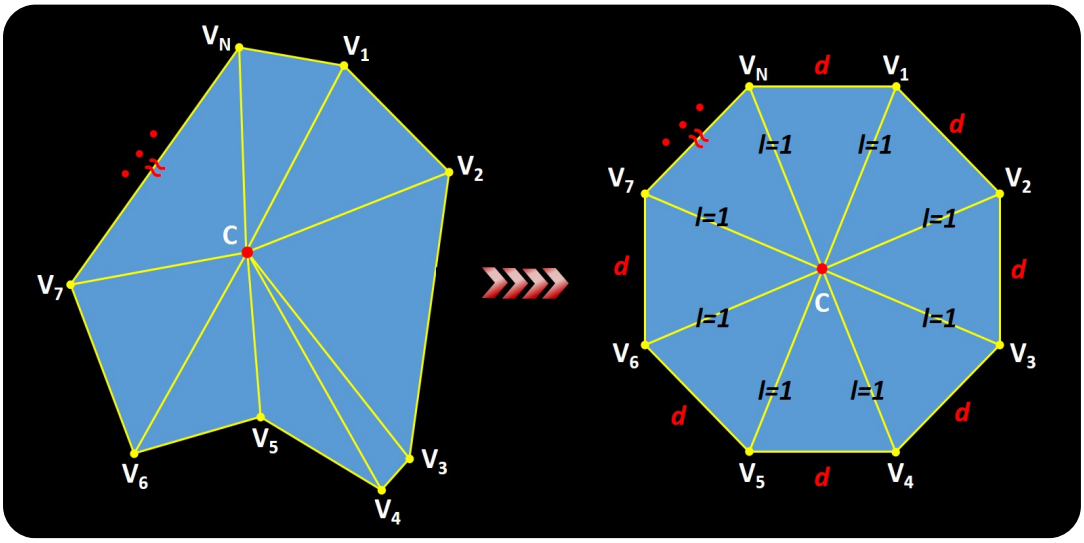

FIGURE 22: Illustration of the Attraction-Repulsion vertices re-positioning in 2D (initial location to the left and the final arrangement to the right).

for enlarging the whole mesh by pushing the nodes outward using the following equation:

$$\mathbf{V}''_{\alpha+1,i} = \mathbf{V}'_{\alpha,i} + \frac{C_R}{2I} \sum_{j=1;j\neq i}^{I} \left(\frac{\Delta_{\alpha,ji}}{|\Delta_{\alpha,ji}|^2} \right) \tag{39}$$

where C_R is the repulsion constant that regulate the nodes displacement.

c. Spherical harmonics shape analysis In order to add more shape classification feature, a spherical harmonics shape analysis is utilized to reconstruct the pulmonary nodules. The mesh reconstruction is done by breaking the object into a group of different linear harmonics. The linear harmonics are generated by solving an isotropic heat equation for the nodule surface on the unit sphere. The lower harmonics describe the basic shape of the nodule, while the higher harmonics shows the complex details of the shape. The deformation of the nodule mesh into the unit sphere maps each voxel $V = (x, y, z)$ to a spherical position that could be represented by the spherical coordinates $S = (sin\theta cos\phi, sin\theta sin\phi, cos\theta)$ where ϕ is the azimuth angle from 0 to 2π and θ is the inclination angle from 0 to π. Y_{lm} is the spherical harmonic of degree l and order m

and is defined as:

$$Y_{lm} = \begin{cases} c_{lm} P_l^{|m|}(\cos\theta) \sin(|m|\varphi), & -l \leq m \leq -1, \\ \frac{c_{lm}}{\sqrt{2}} P_l^0(\cos\theta), & m = 0, \\ c_{lm} P_l^{|m|}(\cos\theta) \cos(|m|\varphi), & 1 \leq m \leq l, \end{cases} \tag{40}$$

where $c_{lm} = \sqrt{\frac{(2l+1)(l-|m|)!}{2\pi(l+|m|)!}}$ and $P_l^{|m|}$ is the associated Legendre polynomials of degree l and order m. The lung nodule is reconstructed using the spherical harmonics obtained from equation 40 by applying the iterative residual fitting procedure developed by Chung et al [226]. The main purpose of using the spherical harmonic expansion is to drive a shape classification feature. The shape classification feature that is extracted from this model is the reconstruction error curve. The reconstruction error curve is a curve that is built for every nodule. It consists of the reconstructions errors for the nodule while reconstructing it using different spherical harmonics orders. This error for a certain mesh node is determined by calculating the Euclidean distance between the surface node location in a certain spherical harmonics order and its original location in the mesh. The final reconstruction error is the summation of the error for all nodes in certain spherical harmonics order.

3. Fundamental Geometric Features

As the lung nodules has different geometric characteristics based on whether it is malignant or benign, accounting for these differences as a discriminating features helps in the differentiation between different nodule types in the classification process. A set of seven geometric features will be extracted from the nodule's binary mask which is provided by the radiologist. The following geometric features are calculated: volume, surface area, convex volume, solidity, equivalent diameter, extent, and the principal axis length. In order to calculate the solidity, a convex hull C is defined around the segmented nodule and the ratio between the volume of the voxels in C and the total volume of the segmented nodule

is calculated. Then, in order to calculate extent, the bounding box around the segmented nodule is used and the dimensions are named dimx, dimy, and dimz and the proportion of the volume of the voxels in the bounding cube to the volume of the voxels of the segmented nodule is calculated. principal axis length is defined as the largest dimension of the bounding cube (max(dimx, dimy, dimz)). These features complement each other to come up with a final score for malignancy classification. To extract these features accurately without being dependent on scan accusation parameters such as pixel spacing and slice thickness, a volume of interest (VOI) of size $40 \times 40 \times 40$ mm3 that is centered around the center of each nodule is extracted and resampled to be an isotropic in the x, y, and z directions.

D. Fusion of multiple features

The proposed CAD system utilizes a feed-forward deep neural network to classify the pulmonary nodules whether malignant or benign, the implemented deep neural network consists of two-stage structure of stacked autoenocder (AE). The first stage consists of an autoencoder-based classifiers for each fused feature or, in other words, each feature that will be involved in the classification needs to have its own autoencoder-based classifier. This classifier will give an initial estimation for the malignancy probability of the input nodule. After that, all the output probabilities for each feature are augmented together to be considered as the input for the second stage autoencoder to give the final estimation of the classification probabilities (see Figure 23 for more details).

Autoencoder is an unsupervised artificial neural network that reduce the input dimensionality and then return it to the original input size back through two process which are the encoding and decoding respectively. It reduces the input size by getting rid of the unimportant features like noise and the redundant information. Autoencoder is a good choice for reducing the dimensionality comparing to the Principle Component Analysis (PCA) because Autoencoder could be a nonlinear transformation for the input vector if a nonlinear activation function is used, while a PCA is always a linear transformation. In the

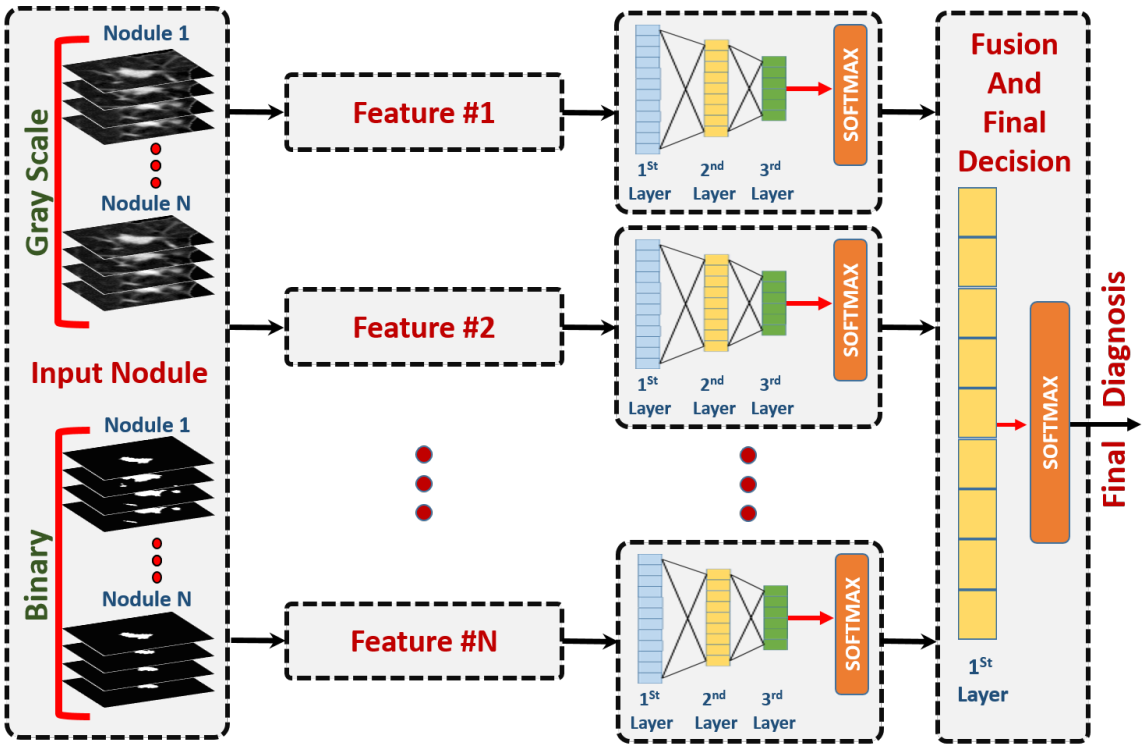

FIGURE 23: The proposed fusion architecture.

presented fusion model Autoencoder is employed in order to diminish the dimensionality of the input data with multi-layered neural networks to get the most discriminating features by greedy unsupervised pre-training. After the AE layers, a softmax output layer is stacked in order to refine the classification by reducing the total loss for the training labeled input.

For each AE, let $W = \{W_j^e, W_i^d : j = 1, \ldots, s; i = 1, \ldots, n\}$ refer to a set of column vectors of weights for encoding, E, and decoding, D, layers, and let T denote vector transposition. The AE change the n-dimensional column vector $u = [u_1, \ldots, u_n]^T$ into an s-dimensional column vector $h = [h_1, \ldots, h_s]^T$ of hidden features such that $s < n$ by nonlinear uniform transformation of s weighted linear combinations of input where $\sigma(.)$ is a sigmoid function with values from $[0, 1]$, $\sigma(t) = \frac{1}{1+e^{-t}}$,

The used classifier is constructed by stacking AE (as shown in Figure 24) which consist of 3 hidden layers with softmax layer for each feature, the first hidden layer reduces the input vector to N_1 level activators, while the second hidden layer continues the reduction

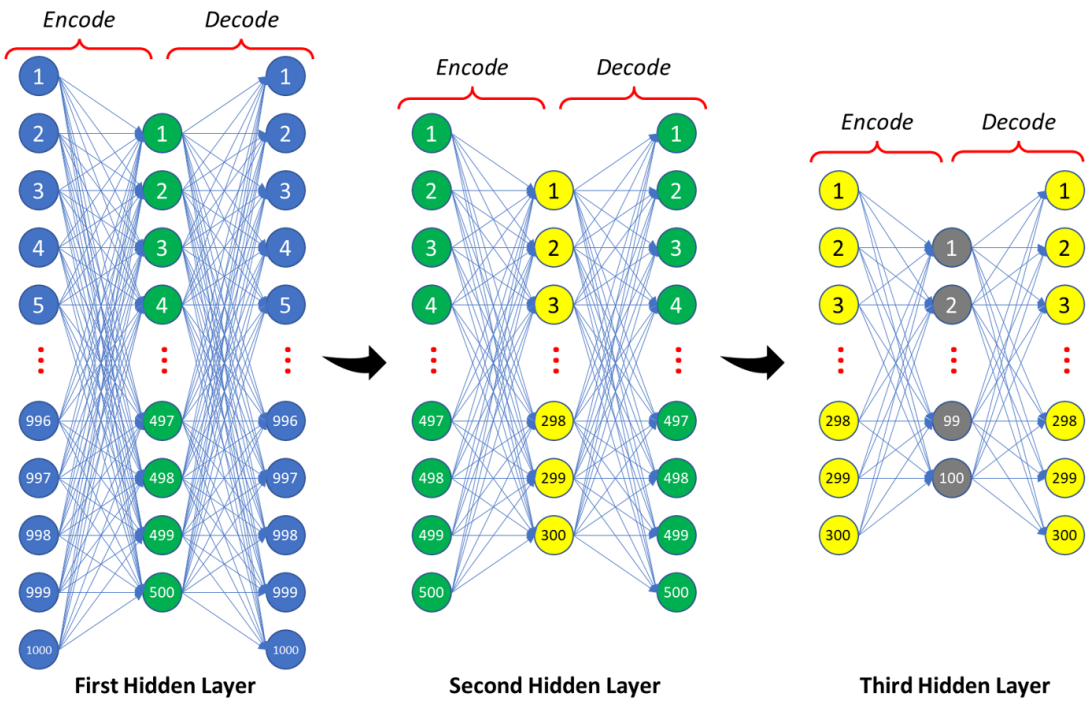

FIGURE 24: The proposed stacked Autoencoder structure when $N_1 = 1000$, $N_2 = 500$, and $N_3 = 300$

to N_2 level activators which are reduced to N_3 after the third layer. Only The fundamental geometric features network consists of the softmax layer only without the Autoencoder network, as the input scale is not large to be in need to use AE with multiple hidden layers to reduce the dimensionality like the other feature vectors (only 9 geometric features). The softmax compute the probability of being malignant or benign through the following equation:-

$$p(c; W_{o:c}) = \frac{e^{(W_{o:c}^T h^3)}}{e^{(\sum_1^c W_{o:c}^T h^3)}} \tag{41}$$

Where $C = 1, 2$; denote the class number $W_{o:c}$; is the weighting vector for the softmax for class c h^3: are the output features from the last hidden layer, (the third layer) of the AE. In the second stage, the output probability obtained from the softmax of all the integrated networks are fused together and fed to another softmax layer to give the final

classification probability. The developed design of the fusion network makes the system very easy to be expanded by adding different components or features. This encouraged me to try to augment the imaging markers with clinical bio-markers. Generally, there are different kinds of bio-markers which are used for lung caner diagnosis, like: breath, urine, saliva, and blood analysis. The breath analysis was a good option to be augmented with the developed clinical imaging markers. The exhaled breath is collected in 1-L Tedlar bags were drawn through a proprietary microreactor chip by applying a vacuum (Figure 25). The surfaces of micropillars of the microreactor chip are coated by 2-(aminooxy)-N, N, N-trimethylethanammonium (ATM) iodide [212]. ATM chemoselectively traps carbonyl compounds in exhaled breath by means of oximation reactions. After the breath sample was completely evacuated from the Tedlar bag, ATM adducts in the microreactor chip were eluted with 100 mL of methanol from a slightly pressurized small vial. The eluted solution was analyzed directly by Fourier transform-ion cyclotron resonance mass spectrometry (FT-ICR-MS) [212]. FT-ICR-MS is a hybrid linear ion trap MS (Finnigan LTQ FT, Thermo Electron, Bremen, Germany) equipped with a TriVersaNanoMate ion source (AdvionBio-Sciences, Ithaca, NY) with an electrospray chip (nozzle inner diameter 5.5 mm) that was used to analyze all breath samples using the eluted solution. A known amount of deuterated acetone completely reacted with ATM (ATM-acetone-d6) in methanol was added to the eluted solution as internal reference for quantification of ATM adducts. The concentrations of all 27 carbonyl VOCs detected in exhaled breath were determined by comparison of the relative abundance with that of added ATMacetone-d6.

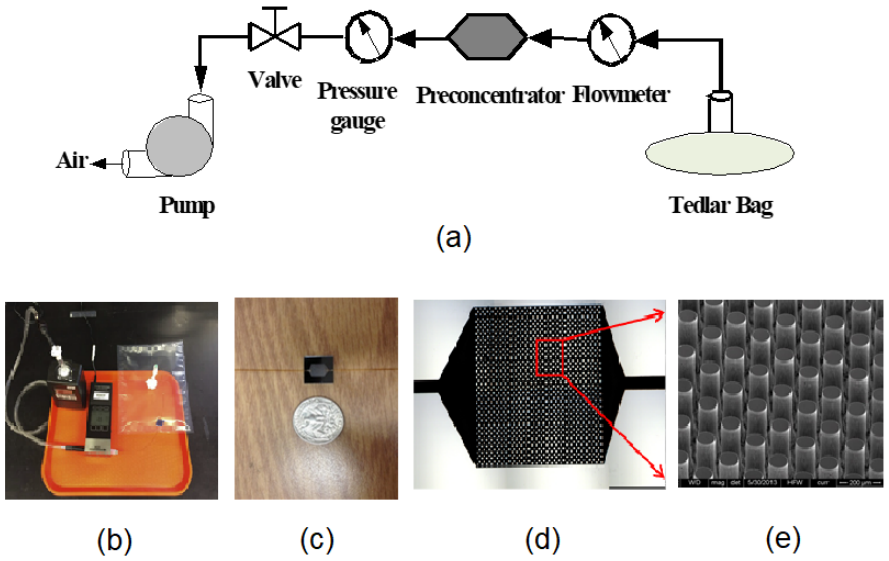

FIGURE 25: (a) Schematic setup for the capture of carbonyl VOCs in exhaled breath; (B) photo of the breath collection system; (c) A microfabricated microchip with fused silica tubes attached to inlet and outlet ports; (d) optical picture of the microchip created by DRIE; (e) SEM micrograph of the micropillar array within the preconcentrator.

The concentration of the 27 carbonyl VOCs is the input vector features that will be augmented with the developed imaging features. It fed to the designed autoencoder network that decreases its dimensionality to 10 followed by a softmax classifier to boost the diagnosis accuracy by limiting the overall loss of the labeled data during the training.

CHAPTER IV
EXPERIMENTAL RESULTS AND DISCUSSION

This chapter reports and discusses the performance of the developed methodologies for the pulmonary nodules diagnosis that were presented in chapter III. It also shows the effect of their integration in a single framework. This chapter starts with a section that presents the experiments setup, by showing the utilized datasets for training and testing followed by the used evaluation metrics to evaluate the proposed methodologies. Finally, the next section reports the evaluation metrics of each proposed methodology and their different combination frameworks.

A. Experiments Setup

1. Datasets

a. LIDC dataset description

The Lung Image Database Consortium (LIDC) and Image Database Resource Initiative (IDRI) [156] is a publicly available reference for the medical imaging research community. It consists of 1018 thoracic CT scans that have been collected from 1010 different patients from eight medical imaging companies (Carestream Health Inc., Fuji Photo Film Co., GE Healthcare, iCAD Inc., Riverain Medical, Philips Healthcare, Siemens Medical Solutions and AGFA Healthcare) and 7 different academic centers (University of California, Weill Cornell Medical College Los Angeles, University of Chicago, University of Michigan, University of Iowa, Memorial Sloan-Kettering Cancer Center and MD Anderson Cancer Center). After removing the scans with slice thickness ≥ 3 mm and the scans

with inconsistent slice spacing, a total of 888 CT scans became available for testing and evaluating the developed CAD system. The LIDC CT scans are associated with an XML file to provide a well descriptive annotation and radiological diagnosis for the lung lesions. This information are provided by 4 thoracic radiologists in a 2-phase image annotation process. In the first phase, each radiologist from the 4 radiologists independently reviewed all cases and this phase is called blind read phase as each one gives their opinion regardless of the other radiologists. The second phase is the final phase as each radiologist gives his final decision after checking the other 3 radiologists' decision, and this phase is called the unblinded phase as all the annotations were made available to all the radiologists before giving their final annotation decision. The radiologists divided the lesions into 2 groups, nodules and non-nodules.

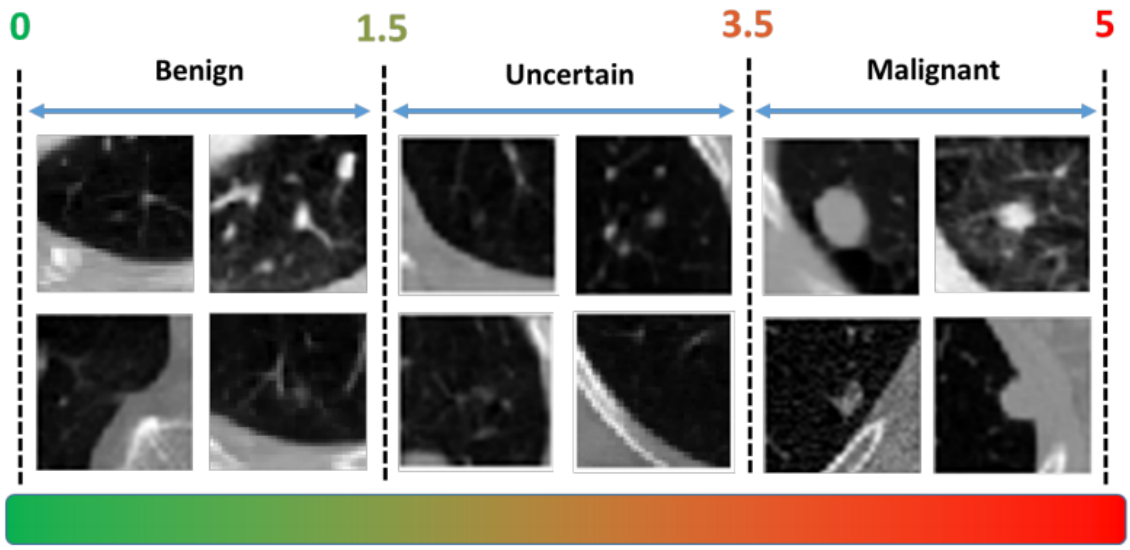

FIGURE 26: 2D axial projection for nodules with low-score, benign, high-score, malignant, and of moderate-score, uncertain.

The database is composed of 7371 nodules ranked by at least one radiologist. Among these nodules 2669 ones were characterized by nodules with a diameter ≥ 3 mm by at least one radiologist and 928 were characterized by nodules with a diameter ≥ 3 mm by four ra-

diologists. The focus will be on the nodules with a diameter ≥ 3 mm that have been ranked by all radiologists. Each nodule of these samples have an annotation that is attributed by all four radiologists where each of them give his unique description of the nodule along with its characteristics. Every nodule description provided by each one of the four radiol-

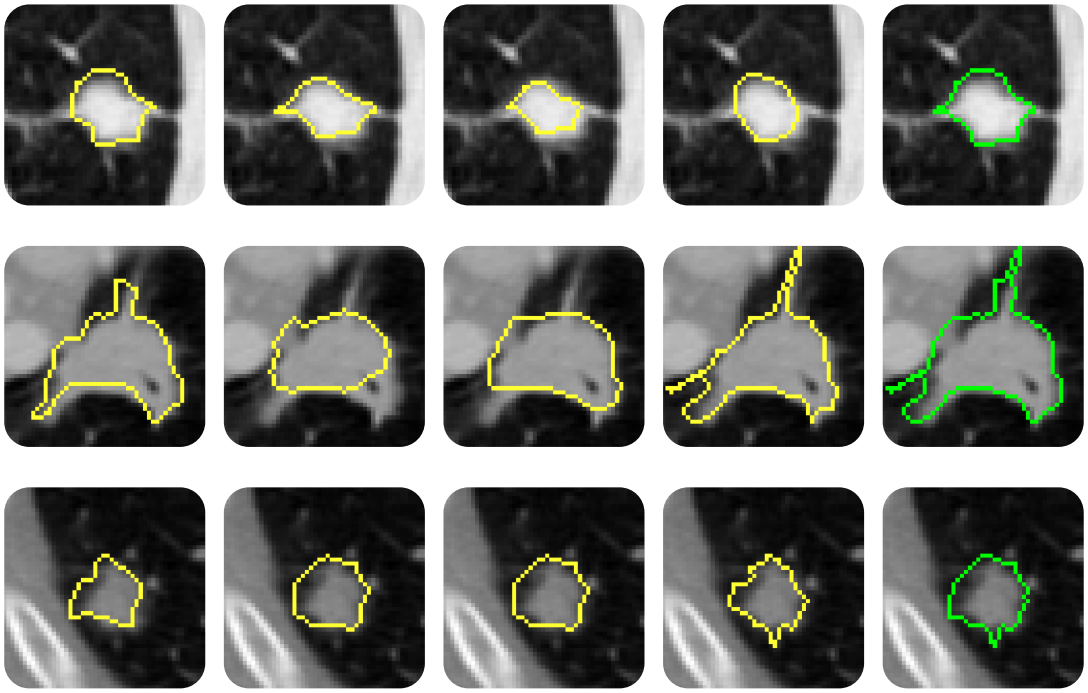

(a) (b) (c) (d) (e)

FIGURE 27: 2D axial projection for three nodules and their masks: *(a)* the mask as annotated by first radiologist, *(b)* the mask as annotated by second radiologist,*(c)* the mask as annotated by third radiologist, *(d)* the mask as annotated by fourth radiologist, *(e)* the combined mask for the four radiologists mask.

ogists is composed of the groundtruth contour of the nodule along the x,y and z direction and a rank of the nodule going from 1 to 5, with a score of 1 for a nodule that is in their opinion most likely to be benign and 5 for a nodule that is most likely to be malignant. It may be concluded that radiologists may disagree on the label of the nodule and its score given the fact that this annotation is only based on looking into the CT scans not on biopsy. This made us turn toward generating our collection based on a majority vote for the four

radiologists. In other words, if the average score of the 4 radiologists for each nodule case is ≥ 3.5 the nodule is labeled as malignant and if the average score is ≤ 1.5 the nodule is considered to be benign. Figure 26 illustrates examples of benign, malignant and uncertain nodules. This way of extracting the used dataset resulted in a total number of 727 nodules (314 malignant and 413 benign) used for training and testing. For each nodule, the union of the 4 radiologists' mask is combined to obtain the final nodule mask that will be used in the experiments as shown in Figure 27 . Samples have been extracted with a $40 \times 40 \times 40mm^3$ volume around the nodule mass center's combined mask.

b. Local acquired CT imaging dataset

CT and breath analysis data were both collected on the same day for every patient from 47 patients in the period from 2016 to 2018 (Table 1,2). The collaborators at the university of Louisville hospital recruited patients with age ranges from 40 to 90 years and collected both a CT scan and a breath test (the diagnosis for most of these patients is biopsy confirmed). Retrospective analyses have an inherent risk of selection bias, despite the inclusion criteria not having any demographic filters that might introduce bias. The research protocol was approved by the Institutional Review Board (IRB) at the University of Louisville and all methods were performed in accordance with the relevant guidelines and regulations.

TABLE 1: Demographics and nodule size of the patients (n=47 patients). D= nodule diameter

	Subject	Male	Female	Nodule Size
Malignant	20	3	17	$4mm \leq D \leq 20mm$
	17	9	8	$20mm \leq D \leq 60mm$
Benign	5	1	4	$4mm \leq D \leq 20mm$
	5	5	0	$20mm \leq D \leq 34mm$

After the patient informed consent was obtained, one liter of mixed tidal and alve-

TABLE 2: Clinical characteristics of the patients

	All patients (N=47)	Male (N=18)	Female (N=29)
Age (years)	48-93	59-93	48-88
Malignant	37	12	25
White race	30	11	19
Height (cm)	152-188	170-188	152-180
Weight (Kg)	39-168	61-156	39-168
Active smoker	21	10	11
Previous smoker	20	7	13
Lifelong non-smoker	6	1	5
Personal history of lung cancer	7	3	4
Personal history of any cancer	19	8	11

olar breath sample was collected into a non-reactive Tedlar bag (Sigma Aldrich, St Louis, Mo) from a single exhalation from each participant [213]. The CT data was collected from the same 47 patients after obtaining the patient informed consent also with a slice thickness of $2.5mm$ reconstructed every $1.5mm$, KV 140, MA 100, and F.O.V $36cm$. The ground truth for nodule detection and segmentation was obtained by the union of the masks of nodules that were manually segmented by three radiologists that have the same level of knowledge (greater than 10 years' experience) and there was no questionable difference between their final decisions. Patient selection was blinded but included patients with both benign and malignant small lung nodules (4 to 20 mm) and large nodules ($> 20mm$). The patient diagnostic conclusions from the radiologists were blinded from the data analysis team for lung cancer diagnosis using both breath test and CT markers. The patients were either biopsied for diagnostic conclusion (these patients does not need follow-up) or followed for up to two years until a final lung cancer diagnosis could be determined based on

current clinical approaches (serial CT scans every 6 months and/or biopsy/bronchoscopy). If there was no change in the CT scan over two years, the nodule was considered benign.

2. Evaluation metrics

There are multiple metrics to measure the performance of the classification methods. These metrics are widely and commonly utilized in CAD systems. These metrics are: True Negative (TN), False Negative (FN), True Positive (TP), and False Positive (FP). TP is the number of correct predictions when the sample is positive. FP is the number of incorrect predictions when the sample is positive. TN is the number of correct predictions when the sample is negative. FN is the number of incorrect predictions when the sample is negative. Based on these metrics, multiple measures can be computed to evaluate the performance of the CAD systems.

a. Accuracy

The Accuracy (Acc) measure is the ratio of the number of correctly classified samples over all samples as shown in the following equation:

$$\frac{TN + TP}{TN + FN + TP + FP} \tag{42}$$

Accuracy alone is not an accurate description for the classification model when the dataset is unbalanced [227], so it needs to be augmented with different measures, like sensitivity, specificity, and precision. Some systems use the term of balanced accuracy, which is the average of the sensitivity and specificity to overcome the confusion of the accuracy in case the dataset is unbalanced.

b. Sensitivity

The sensitivity (Sn) measure refers to the classifier's ability to correctly predict the positive samples. Numerically, sensitivity is the number of true positive samples that are correctly classified over the sum of true positive and false negative samples as shown in the

following equation:

$$\frac{TP}{TP + FN} \tag{43}$$

c. Specificity

The specificity (Sp) measure refers to the classifier's ability to correctly predict the negative samples. Numerically, specificity is the number of true negative samples that are correctly classified over the sum of true negative and false positive samples as shown in the following equation:

$$\frac{TN}{TN + FP} \tag{44}$$

d. Precision

The precision (Prc) measure defines the amount of predicted nodules that are actually associated with the malignant samples. Numerically, Precision is the number of true positive samples that are correctly classified over the sum of true positive and false positive samples as shown in the following equation:

$$\frac{TP}{TP + FP} \tag{45}$$

e. Area Under Curve (AUC) of the Receiver operating characteristic (ROC) curve

AUC measures the performance of classification tasks at multiple threshold settings. ROC define a probability curve and AUC characterizes the degree or measure of separability between classes. It identifies how much it is possible for the model to separate between classes. The ROC curve itself is a plot of sensitivity versus 1-specificity for different threshold values in the model. The AUC is a good indicator for the system performance as the higher the AUC, the better the model is at differentiating between malignant and benign nodules.

B. Experimental Evaluation

1. Appearance-based features result

a. 3D Histogram of oriented gradients (HOG)

The HOG features have multiple parameters that need to be optimized in order to get the highest accuracy measures from this module. These parameters are:

- The number of cells in each block that the mean gradient will be calculated over it.
- The number of blocks that the volume is divided into.
- The number of histogram bins.
- The binning style whether full binning or just half of them.

Table 3 presents different evaluation metrics for the HOG features using 20 full bins. It shows that using $5 \times 5 \times 5$ blocks and $3 \times 3 \times 3$ cells is the optimal for this experiment. Table 4 presents the same evaluation metrics using $5 \times 5 \times 5$ blocks and $3 \times 3 \times 3$ cells for the different binning options. It shows that using the dodecahedron (20 bins) using full binning is the optimum parameters for this experiment. Figure 28 and 29 summarize the reported evaluation metrics for the HOG features for $5 \times 5 \times 5$ and $4 \times 4 \times 4$ blocks, respectively. Figure 30 shows the results of different binning parameters, while using $5 \times 5 \times 5$ blocks and $3 \times 3 \times 3$ cells.

TABLE 3: Comparison between accuracy, sensitivity, and specificity using different configuration of 3D-HOG parameters (number of blocks and cell size).

Number of Blocks	Cell Size	Accuracy	Sensitivity	Specificity
4	3	83.03	80.65	84.80
	4	79.36	72.04	84.80
	5	81.65	74.19	87.20
	8	71.56	60.22	80.00
	10	78.90	68.82	86.40
5	3	**88.17**	**87.26**	**88.86**
	4	86.24	82.80	88.80
	5	83.03	78.49	86.40
	8	84.86	81.72	87.20
	10	80.28	82.80	78.40

TABLE 4: Comparison between accuracy, sensitivity, and specificity using different configuration of 3D-HOG parameters (the polyhedron type and binning style).

Polyhedron	Binning style	Accuracy	Sensitivity	Specificity
Dodecahedron (20 bin)	Full binning	**88.17**	**87.26**	**88.86**
	Half binning	70.80	74.49	68.00
Icosahedron (12 bin)	Full binning	72.61	85.25	63.20
	Half binning	66.56	55.22	75.00

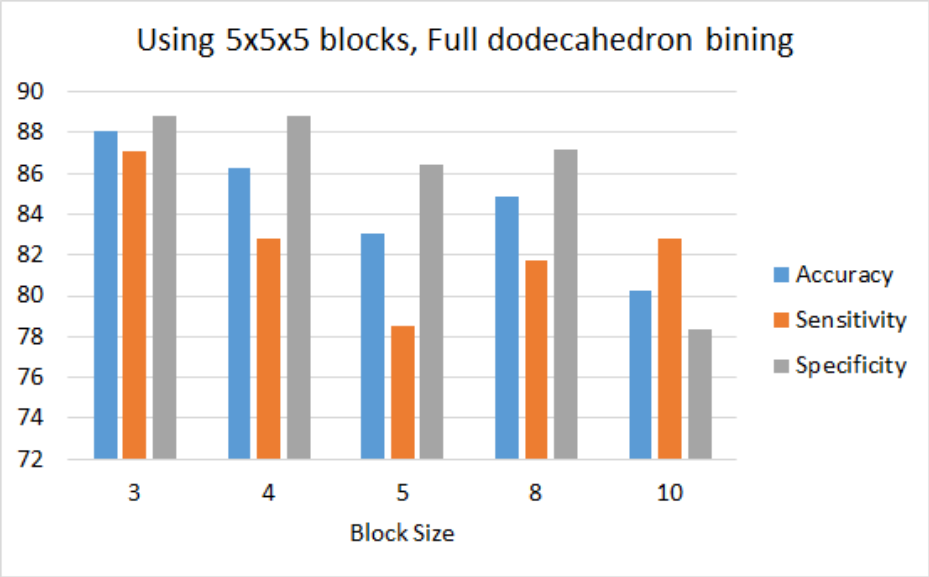

FIGURE 28: Comparison between accuracy, sensitivity, and specificity for $5 \times 5 \times 5$ blocks for the 3D-HOG using different cell size.

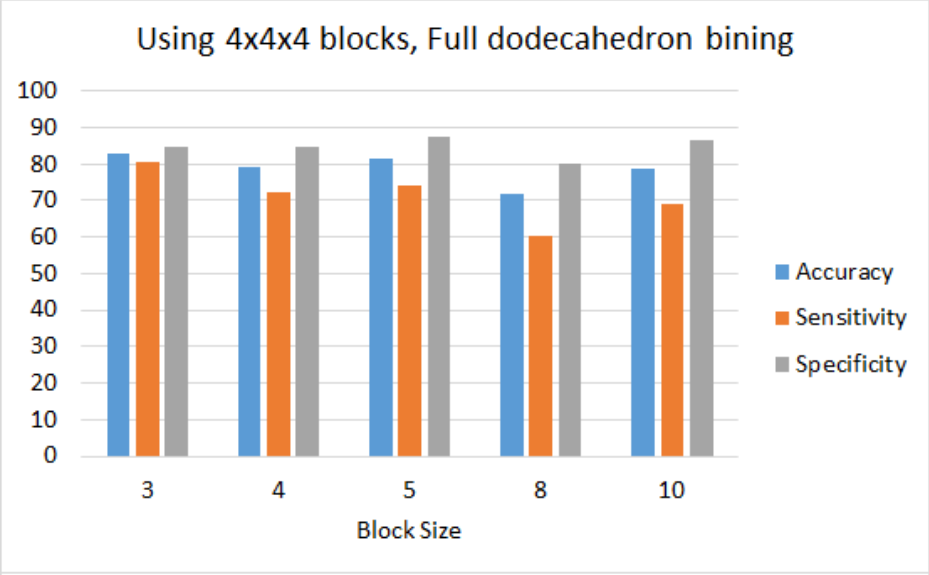

FIGURE 29: Comparison between accuracy, sensitivity, and specificity for $4 \times 4 \times 4$ blocks for the 3D-HOG using different cell size.

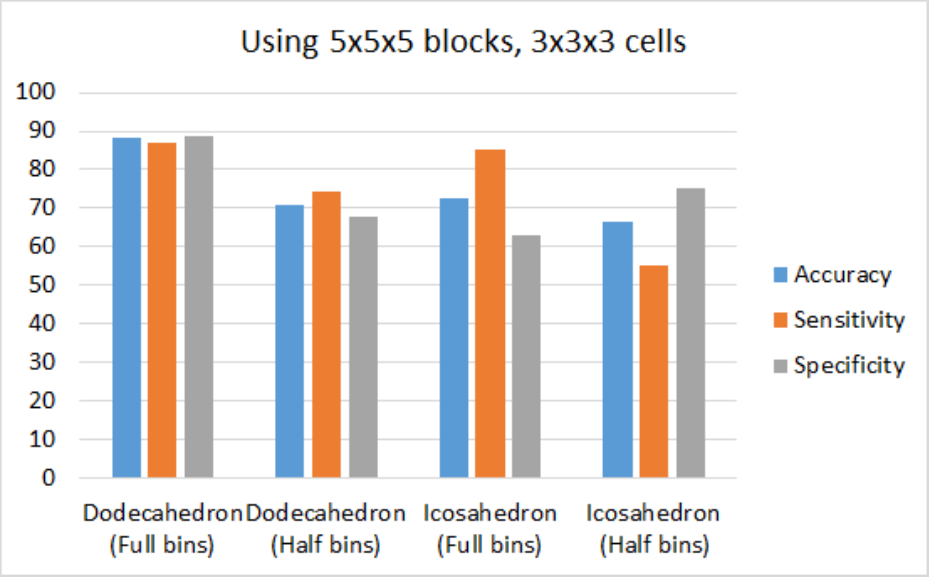

FIGURE 30: Comparison between accuracy, sensitivity, and specificity for $5 \times 5 \times 5$ blocks and $3 \times 3 \times 3$ cells for the 3D-HOG using different binning parameters.

b. 3D Spherical Sector-Isosurface Histgram of Oriented Gradient, (3D-SSIHOG)

For the SIHOG features, there were multiple parameters that need to be optimized in order to get the highest accuracy measures from this feature. These parameters are:

- The number of the utilized isosurfaces.
- The number of spherical sectors that the volume is divided into.
- The number of histogram bins.
- The binning style whether full binning or just half of them.

Table 5 presents different evaluation metrics for the SIHOG features using 20 spherical sector. It shows that using 20 sectors and 4 isosurfaces is the optimal for this experiment. Table 6 presents the same evaluation metrics using 20 spherical sectors and 4 isosurfaces for the different binning options. It shows that using the dodecahedron (20 bins) using full binning is the optimum parameters for this experiment. Figure 31 and 32 summarize the reported evaluation metrics for the SIHOG features for 20 and 12 spherical sectors,

respectively. Figure 33 shows the results of different binning parameters, while using 20 spherical sectors and 4 isosurfaces.

TABLE 5: Comparison between accuracy, sensitivity, and specificity using different configuration of 3D-SSIHOG parameters (number of sectors and number of isosurfaces).

Sectors Number	Isosurfaces Number	Accuracy	Sensitivity	Specificity
20	3	88.07	87.10	88.80
	4	**92.66**	**94.62**	**91.20**
	5	90.83	93.55	88.80
12	3	91.28	93.55	89.60
	4	91.74	94.62	89.60
	5	88.07	87.10	88.80

TABLE 6: Comparison between accuracy, sensitivity, and specificity using different configuration of 3D-SSIHOG parameters (the polyhedron type and binning style).

Polyhedron	Binning style	Accuracy	Sensitivity	Specificity
Dodecahedron	Full binning	**92.66**	**94.62**	**91.2**
(20 bin)	Half binning	89.45	91.40	88.00
Icosahedron	Full binning	90.37	92.47	88.80
(12 bin)	Half binning	72.61	85.25	63.20

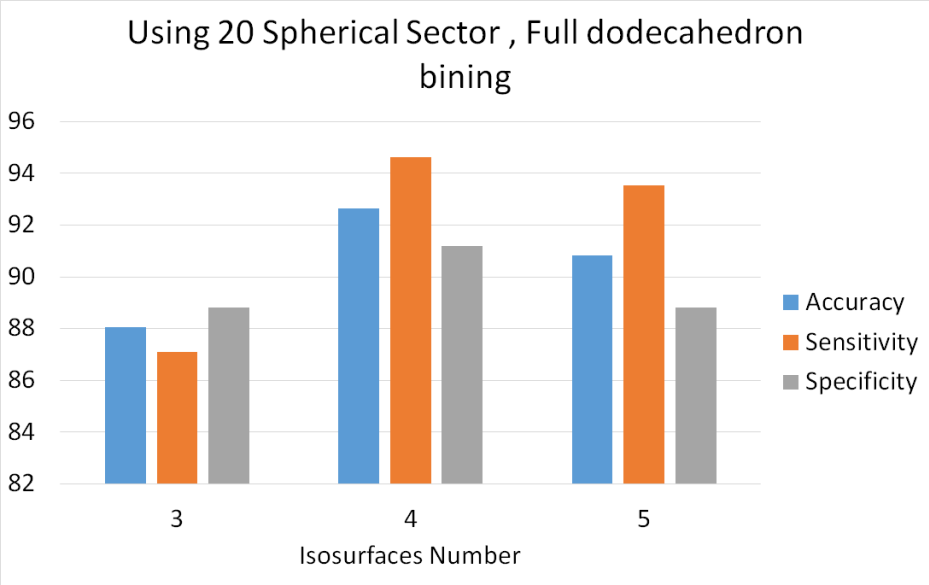

FIGURE 31: Comparison between accuracy, sensitivity, and specificity for 20 spherical sector with Full dodecahedron binning for the 3D-SSIHOG using different isosurfaces number.

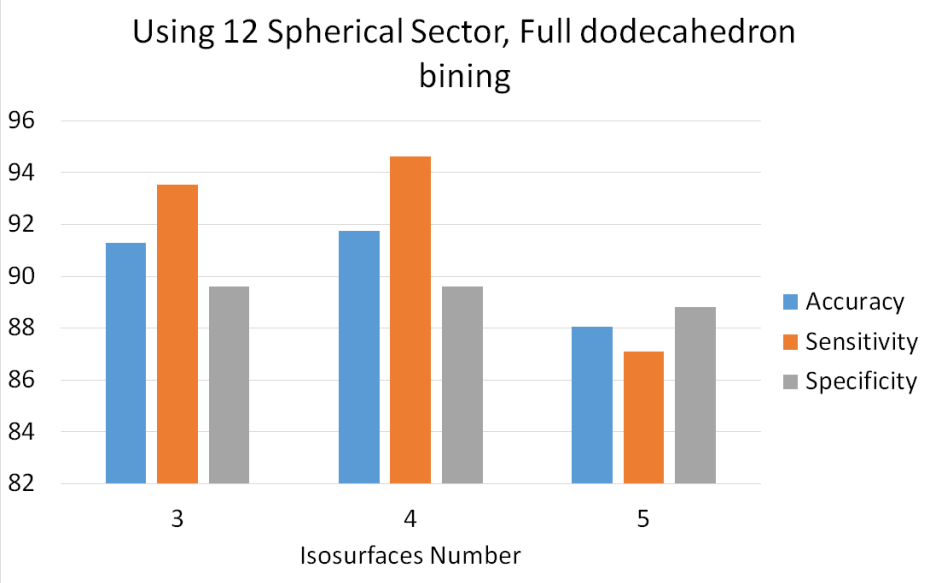

FIGURE 32: Comparison between accuracy, sensitivity, and specificity for 12 spherical sector with Full dodecahedron binning for the 3D-SSIHOG using different isosurfaces number.

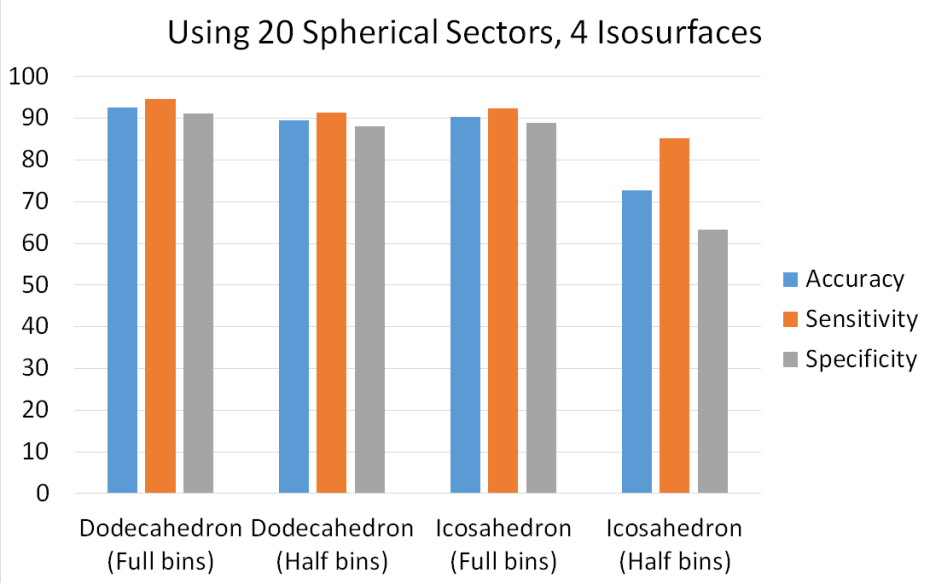

FIGURE 33: Comparison between accuracy, sensitivity, and specificity for 20 spherical sector with 4 isosurfaces for the 3D-SSIHOG using different binning parameters.

c. 3D Adjustable Local Binary Pattern (3D-ALBP)

For the Adjustable LBP features the value of the Weber fraction k is needed to be optimized in order to get the highest accuracy measures from this descriptor. Table 7 presents different evaluation metrics for the Adjustable LBP features using different values of the Weber fraction k. It shows that the optimal Weber fraction value for this application is $k = 0.08$. Figure 34 shows the reported accuracy measure for different Weber fraction k values.

TABLE 7: Comparison between accuracy, sensitivity, and specificity using different configuration of 3D-Adjusted LBP parameter (Weber fraction values).

Weber Fraction	Accuracy	Sensitivity	Specificity
0	86.70	75.27	95.20
0.01	88.07	78.49	95.20
0.05	90.83	94.62	88.00
0.08	**91.74**	**94.62**	**89.60**
0.13	91.28	94.62	88.80
0.16	91.28	94.62	88.80
0.19	90.37	90.32	90.40
0.21	87.16	76.34	95.20

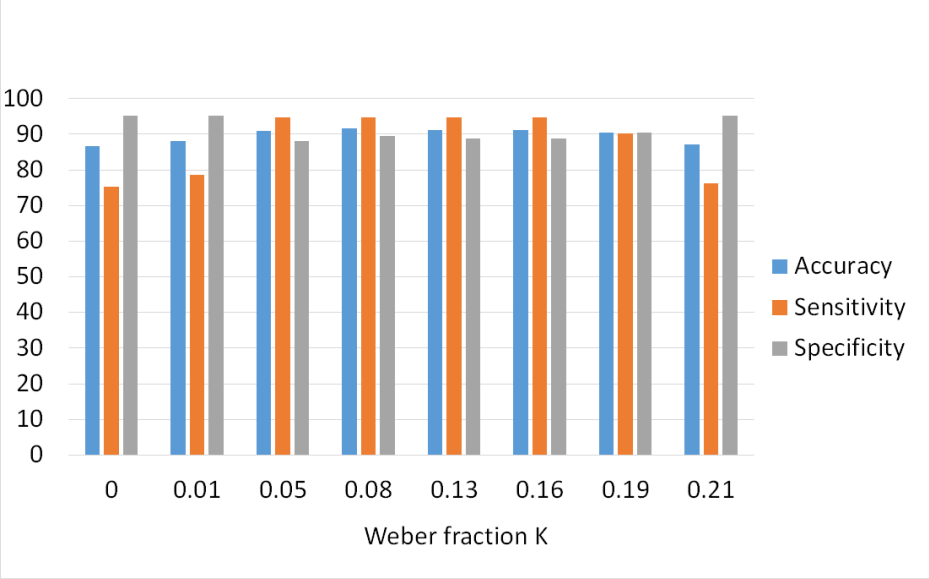

FIGURE 34: Comparison between accuracy, sensitivity, and specificity using different configuration of 3D-Adjusted LBP parameter (Weber fraction values).

d. 3D Resolved Ambiguity Local Binary Pattern (3D-RALBP)

The thresholds selection for the RALBP descriptor is a very important optimization process in order to have the best accuracy from this descriptor. The first experiment is to divide the neighborhood voxel differences after sorting them into three different groups: low, medium, and high differences. Consequently, the average value for each group is calculated; the t_1 threshold is selected as the mean between the averages of low differences and medium differences, and the t_2 threshold is selected as the mean between the averages of medium differences and high differences. The second experiment is to use $k-$mean clustering to divide the voxel differences into the 3 groups and select the threshold based on the same idea as before, but instead of using the average, the center of each cluster will be used.

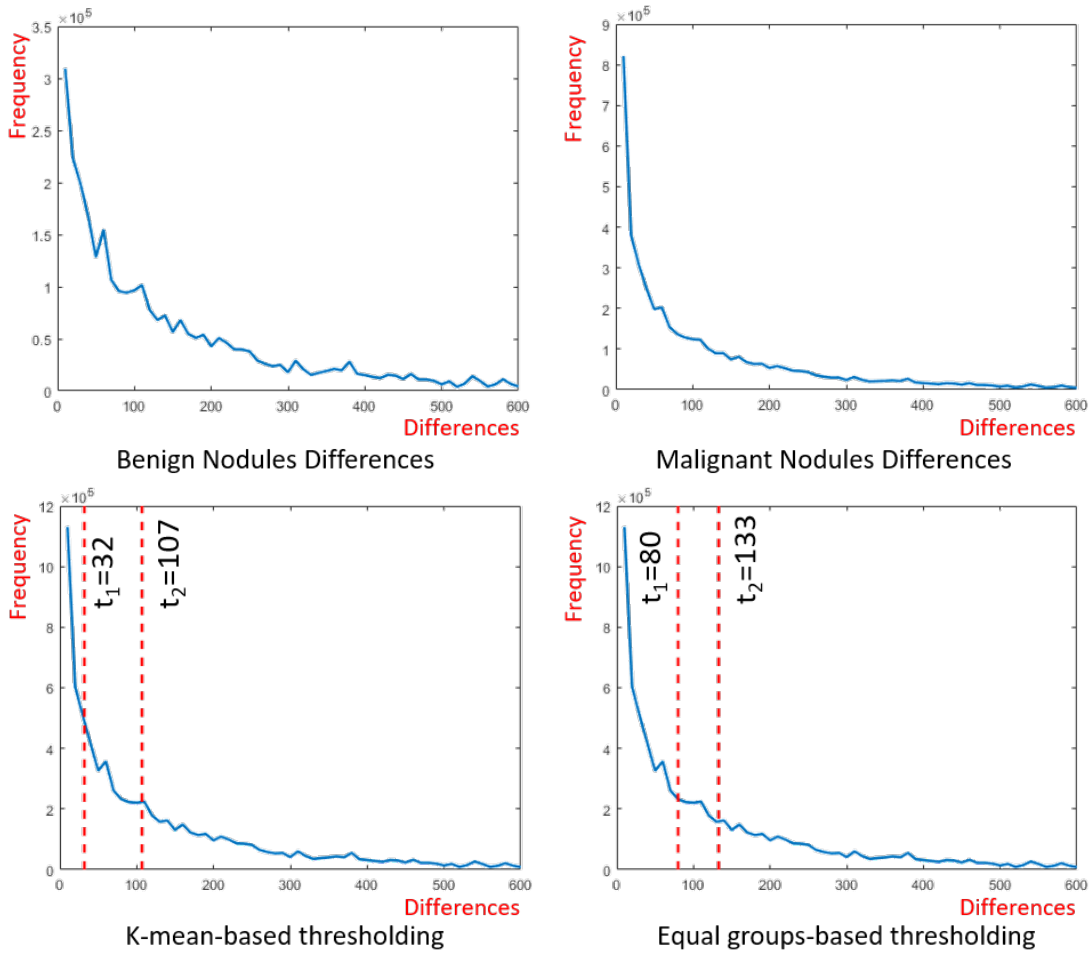

FIGURE 35: Neighborhood voxels differences distribution

Figure 35 shows the voxel differences distribution for malignant and benign nodules, as well as the distribution for all nodules with the different thresholding criteria. In these experiments, the threshold values that achieved the highest accuracy are: $t_1 = 80$, and $t_2 = 133$. The accuracy, sensitivity, and specificity for these thresholds are 91.74%, 94.62%, and 89.60%.

e. Multi-View Analytical Local Binary Pattern (ALBP)

Multi-view ALBP has many parameters that require tuning in order to achieve the best accuracy. These parameters are:

- The number of levels used around the center point.

- The used scheme for resampling.
- The number of extracted 2D-views.

Table 8, 9, and 10 present different evaluation metrics for the Multi-view analytical LBP features using full N resampling, single resampling, and average N resampling scheme, respectively. It shows that using 5 views and 3 levels is the optimal for these experiments. Figure 36, 38, and 37 summarize the reported evaluation metrics for the Multi-view analytical LBP features for full N resampling, single resampling, and average N resampling scheme, respectively. From these figures it could be concluded easily that the single N resampling has the lowest accuracy among all the resampling schemes regardless the other parameters. Moreover, the average N and full N has no noticeable difference in the accuracy which make the average N resampling scheme the best when it is taken into account the calculations cost. Also, The experiments show that the best accuracy is achieved when five views are used for the 3D volume while involving three levels of neighbors around the central pixel.

TABLE 8: Comparison between accuracy, sensitivity, and specificity for full N sampling using different configuration of Multi-View Analytical LBP parameters (number of views and number of levels).

		Full N resampling		
Views Number	Levels Number	Accuracy	Sensitivity	Specificity
3	2	85.13	82.45	88.32
	3	88.53	87.62	88.68
	4	86.32	76.12	91.23
	5	84.86	80.65	85.10
5	2	88.91	87.31	89.37
	3	**90.69**	**91.50**	**89.60**
	4	90.56	91.32	89.40
	5	89.78	87.10	90.65
7	2	87.75	78.33	90.30
	3	87.90	80.17	90.21
	4	86.24	79.11	89.70
	5	85.32	77.30	86.67

TABLE 9: Comparison between accuracy, sensitivity, and specificity for single N sampling using different configuration of Multi-View Analytical LBP parameters (number of views and number of levels).

		Single N resampling		
Views Number	Levels Number	Accuracy	Sensitivity	Specificity
3	2	83.13	80.56	84.70
	3	88.17	87.30	88.56
	4	84.33	81.72	87.30
	5	83.80	81.72	86.40
5	2	86.50	82.80	88.71
	3	**88.71**	**87.60**	**88.93**
	4	87.10	79.85	89.31
	5	84.78	81.33	85.11
7	2	86.50	76.20	90.00
	3	87.10	79.85	88.93
	4	85.95	78.91	87.56
	5	83.80	81.72	86.40

TABLE 10: Comparison between accuracy, sensitivity, and specificity for average N sampling using different configuration of Multi-View Analytical LBP parameters (number of views and number of levels).

		Average N resampling		
Views Number	Levels Number	Accuracy	Sensitivity	Specificity
3	2	84.31	82.86	86.40
	3	88.80	87.51	89.13
	4	85.60	80.36	87.66
	5	86.00	76.73	90.65
5	2	88.81	87.33	89.70
	3	**90.73**	**92.56**	**90.31**
	4	90.18	90.80	89.63
	5	89.90	91.32	88.13
7	2	88.00	87.13	89.70
	3	89.60	88.12	90.57
	4	88.20	87.10	89.73
	5	87.80	80.45	88.44

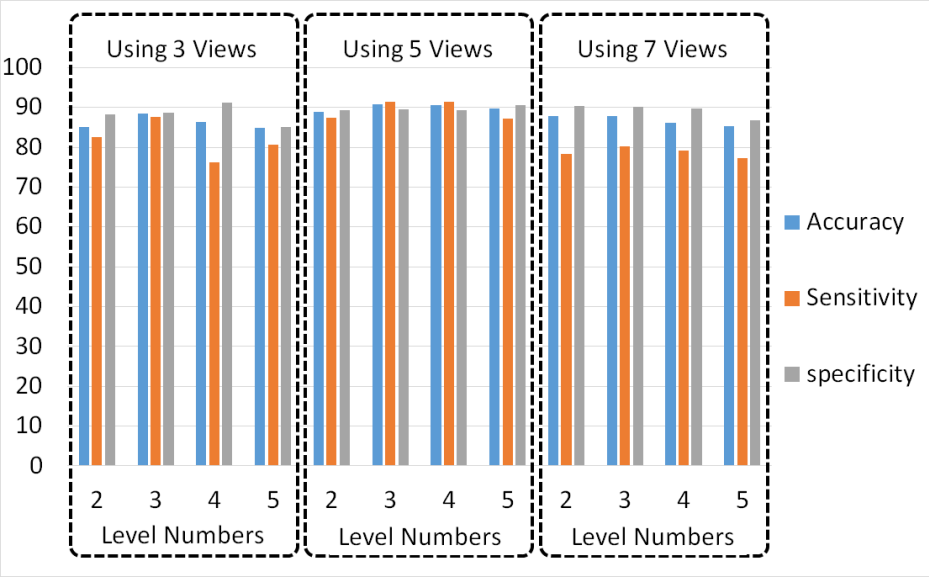

FIGURE 36: Comparison between accuracy, sensitivity, and specificity using different configuration of Multi-View Analytical LBP parameters (number of views and number of levels) for full N resampling scheme.

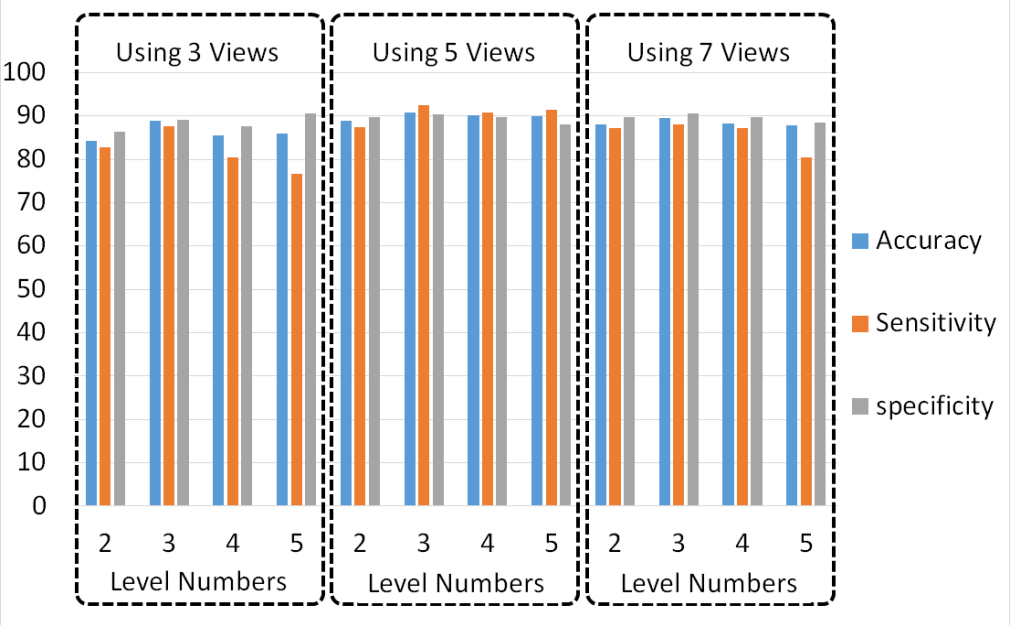

FIGURE 37: Comparison between accuracy, sensitivity, and specificity using different configuration of Multi-View Analytical LBP parameters (number of views and number of levels) for average N resampling scheme.

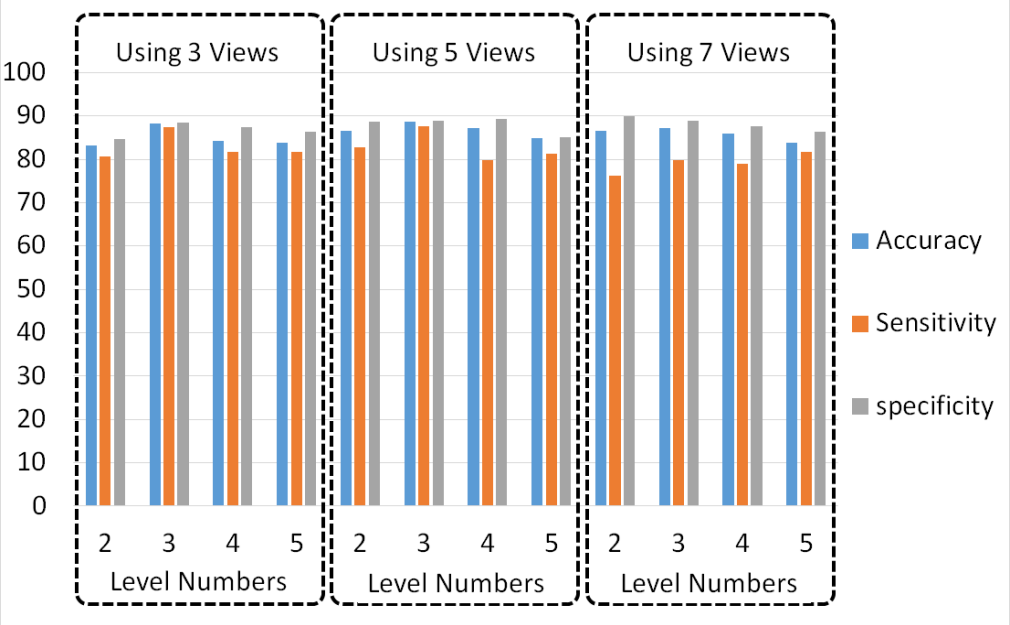

FIGURE 38: Comparison between accuracy, sensitivity, and specificity using different configuration of Multi-View Analytical LBP parameters (number of views and number of levels) for single N resampling scheme.

f. Markov Gibbs Random Field (MGRF)

The output of the MGRF is the Gibbs energy image for the nodule. This image has a high Gibbs energy for benign nodules and a low energy for the malignant ones. The histogram for this image is selected as a representation for this Gibbs energy image. The high energy bins for the malignant nodules have less density comparing with the low energy bins that have high density. The number of histogram bins is the parameter that needs to be optimized. Table 11 shows the reported evaluation metrics for different bin numbers. It could be concluded form this table that there is no noticeable difference in the evaluation metrics when the number of bins changed. This stability in the evaluation metrics regardless the change of bin numbers, makes the MGRF and Gibbs energy a reliable features for distinguishing between the appearance of the malignant and benign nodules.

TABLE 11: Comparison between accuracy, sensitivity, and specificity using different histogram bin numbers for the Gibbs energy image.

Bins Number	Accuracy	Sensitivity	Specificity
400	89.32	92.37	87.94
600	89.83	87.50	92.75
800	89.12	92.11	88.59
1000	89.91	93.55	87.20

2. Shape-based features result

a. Multi-views Peripheral Sum Curvature Scale Space (PSCSS)

The Multi-View PSCSS descriptor parameters that need to be tuned are:

- The pixel jump while calculating the curvature.
- The number of extracted 2D-views.

Table 12 presents different evaluation metrics for the Multi-view PSCSS features while using different values for the number of the extracted views and the pixels jump while calculating the curvature. Figure 39, 40, and 41 summarize the reported evaluation metrics for the Multi-view PCSS features while extracting 3 views, 5 views, and 7 views, respectively. The perfect combination is using 15 pixel jump and 5 2D-views.

TABLE 12: Comparison between accuracy, sensitivity, and specificity using different configuration of Multi-View PSCSS parameters (number of views and gap between points).

Views Number	Points Gap	Accuracy	Sensitivity	Specificity
3	10	87.61	87.10	88.00
	15	88.53	88.17	88.80
	20	85.32	84.95	85.60
	25	84.86	82.80	86.40
5	10	89.91	89.25	90.40
	15	**90.37**	**89.25**	**91.20**
	20	85.78	87.10	84.80
	25	84.40	83.87	84.80
7	10	88.53	87.10	89.60
	15	87.61	87.10	88.00
	20	86.24	84.95	87.20
	25	85.32	82.80	87.20

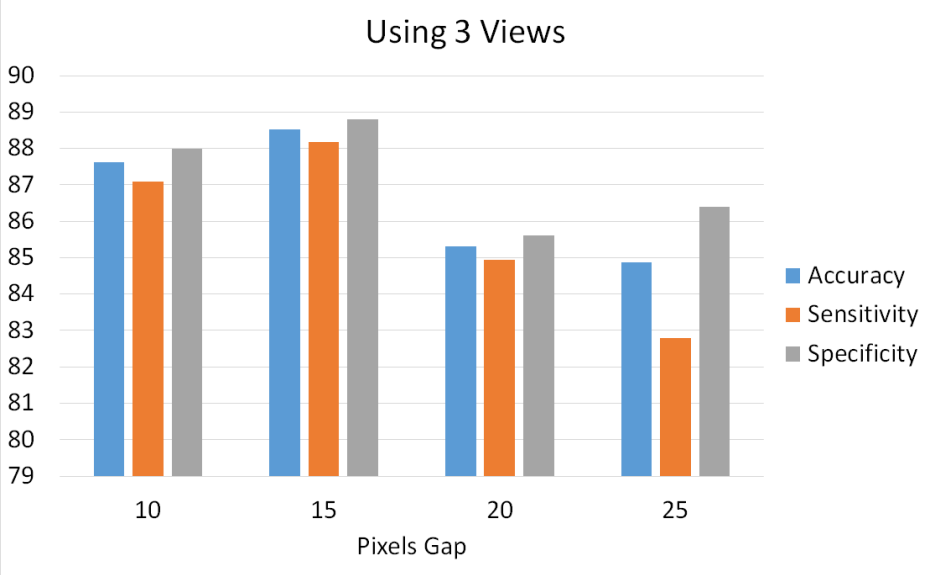

FIGURE 39: Comparison between accuracy, sensitivity, and specificity using different configuration of Multi-View PSCSS parameter (gap between pixels) for 3 views.

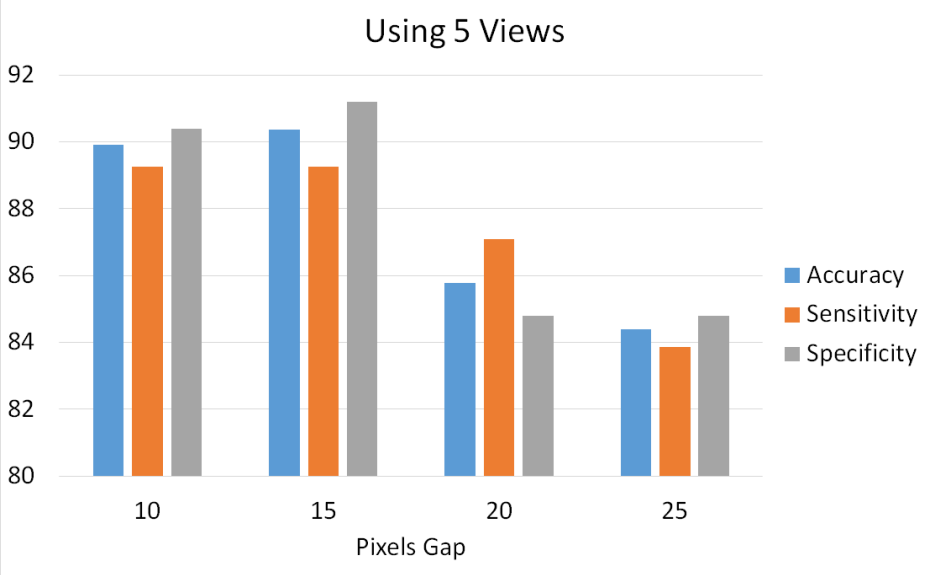

FIGURE 40: Comparison between accuracy, sensitivity, and specificity using different configuration of Multi-View PSCSS parameter (gap between pixels) for 5 views.

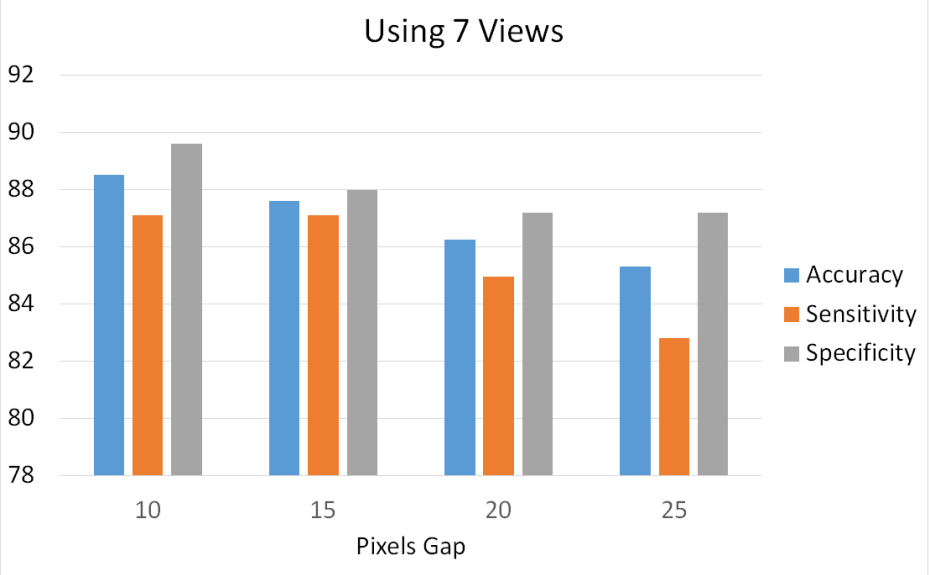

FIGURE 41: Comparison between accuracy, sensitivity, and specificity using different configuration of Multi-View PSCSS parameter (gap between pixels) for 7 views.

b. Spherical Harmonics

The spherical harmonic expansion can use different orders of spherical harmonics to reconstruct the lung nodule. Using higher orders will reduce the reconstruction error comparing with the low orders. The order number of the spherical harmonics is the parameter that needs to be optimized to reduce the redundant calculations during building the feature vector. Figure 42 shows the average error curve for the reconstruction of all the nodule in the LIDC dataset. It could be concluded from the figure that the average reconstruction error is less than 0.1 after 65 spherical harmonics order. However, the 65 order is enough to describe the used data, the feature vector that will be used in the classification will be 70 in order to avoid over fitting for the utilized dataset. Using 70 spherical harmonics orders is able to achieve 89.82, 93.55, 87.20, 84.75, and 0.9642 for the accuracy, sensitivity, specificity, and AUC, respectively.

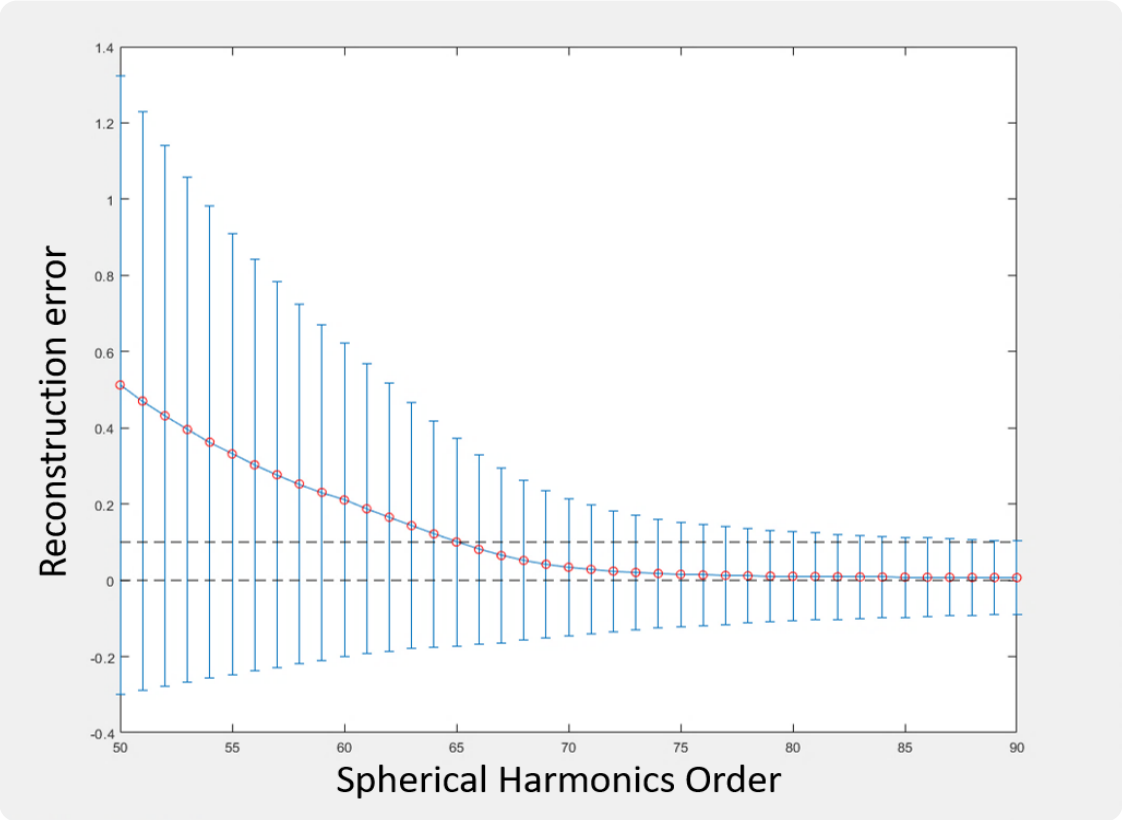

FIGURE 42: Average error curves of the nodule reconstruction using different spherical harmonics orders.

3. The integrated system results after fusion

After validating the developed models separately, this section will report the validation of the fusion of different combinations of the developed models. The fusion has a noticeable increase of performance in terms of the evaluation metrics. The implemented fusion network in section III.D is utilized to combine the developed features. The utilized parameters for each fused model were the parameters that achieved the best evaluation metrics in the previous sections in this chapter.

a. The fusion framework for the appearance features.

The reported accuracy, sensitivity, and specificity for the integration of all the mod-

eled appearance features were 92.87%, 94.66%, and 91.30%, respectively. This framework is depicted in Figure 43 and shows the integration between MGRF, Resolved ALBP, 3D-SSIHOG, 3D-HOG, Adjustable LBP, and Multi-view Analytical LBP features. When these results were compared with those of every appearance model individually, it could be concluded that this integration did not increase the evaluation metrics significantly. Logically, these results make sense, as all of the appearance models are describing the texture appearance of the nodule in order to show the homogeneity of the HU signal in the nodule. This homogeneity of the signal is the key point in differentiating between malignant and benign nodules. However, all these descriptors describe the texture appearance of the nodules, everyone of them has its own way to describe this texture, and this is the reason for this little enhancement for the accuracy measures.

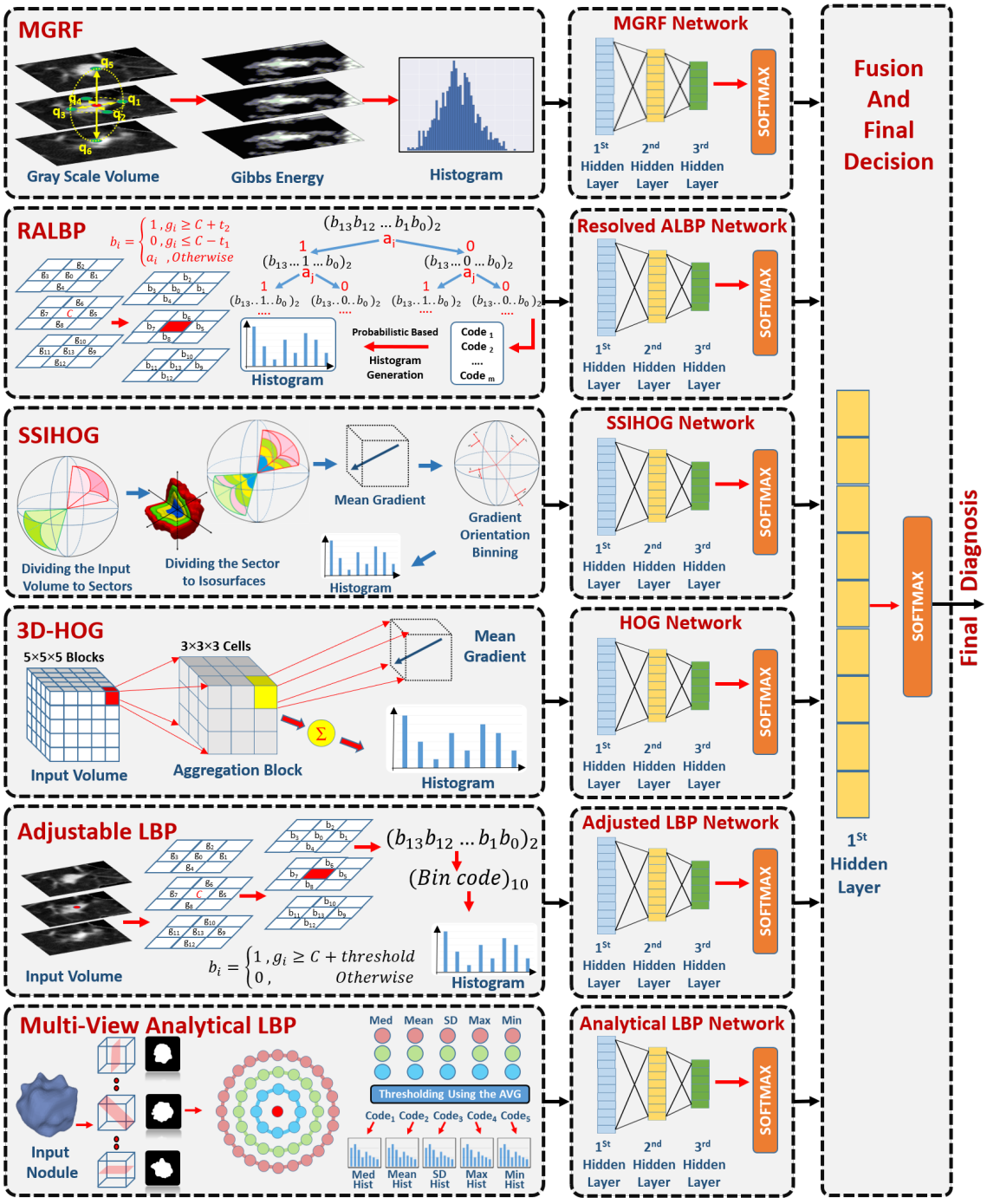

FIGURE 43: The integration framework between the different developed six appearance models.

b. The fusion framework for the shape features.

The reported accuracy, sensitivity, and specificity for the integration of all the modeled shape features were 90.89%, 90.43%, and 91.15%, respectively. This framework is depicted in Figure 44 and shows the integration between Mutli-view PSCSS, spherical harmonics, and fundamental geometric features. When these results were compared with the results of every shape model individually, it could be concluded that this integration did not increase the evaluation metrics significantly. Logically, these results make sense, as all of the shape models are describing the shape complexity of the nodule in order to show the irregularity of the contour of the nodule. This irregularity of the contour is the key point in differentiating between malignant and benign nodules. However, all these descriptors describe the shape of the nodules, everyone of them has its own way to describe this shape complexity, and this is the reason for this little enhancement for the accuracy measures.

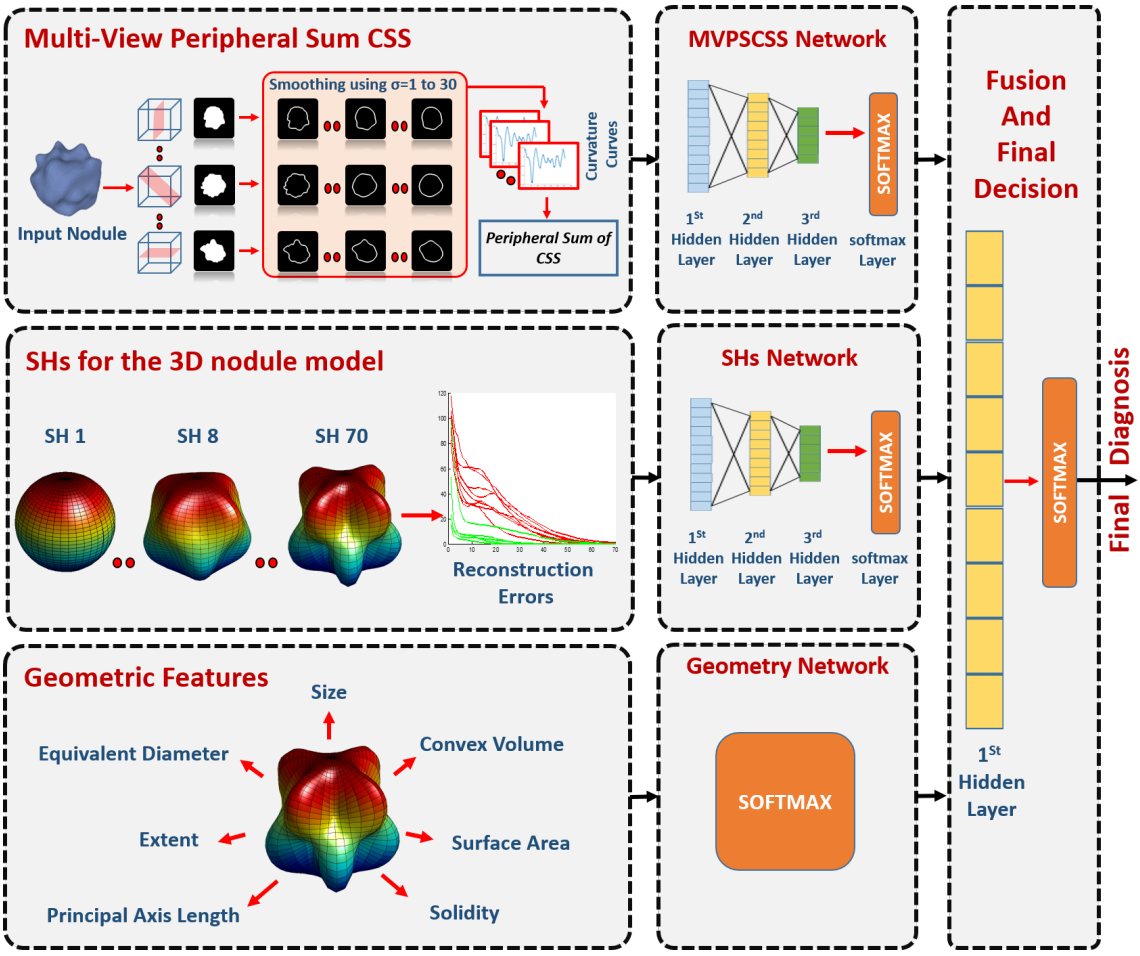

FIGURE 44: The integration framework between the different developed three shape models.

c. The hybrid frameworks integrating the appearance and shape features.

From the previous two sections, it could be concluded that combining different models for the appearance or different models for the shape did not made a big enhancement to the fused frameworks. In this section, a fusion between different combinations of models that describe different characteristics of the lung nodules. There are very huge number of combinations of these models, that will lead to a very huge number of frameworks. This is the reason to be selective in these frameworks. The selection criteria is to use the models that are different in the way of describing the nodule either by appearance

or shape. For example, the 3D-HOG will not be combined with the 3D-SSIHOG, as both of them are depending on the idea of calculating the histogram of oriented gradient, as the 3D-SSIHOG is an improvement to the 3D-HOG on the level of changing the way of dividing the volume into blocks. The same idea for the different enhancements of the LBP algorithm.

The framework I integrates the MGRF model from the appearance models with the geometric features from the shape models. This framework has been published in the International Conference on Image Processing (ICIP) [63]. This framework is illustrated in Figure 45. Table 13 shows the evaluation metrics to this framework and all its components with comparison to some of other published frameworks that uses the same dataset.

TABLE 13: Evaluation of the hybrid framework I that integrates appearance (MGRF) and shape (geometric features) models and its comparison with 4 different recent frameworks that use the same dataset.

	Evaluation Metrics				
	Accuracy	Sensitivity	Specificity	Precision	AUC
Geometric Features	80.73	76.64	84.68	82.83	87.20
MGRF	89.91	93.55	87.20	84.47	96.66
Hybrid Framework I	**92.20**	**92.22**	**92.19**	**89.25**	**96.70**
Orozco et al [228]	82.00	90.90	73.91	-	0.81
Wei et al [176]	87.65	89.30	86.00	86.45	0.942
Costa et al [229]	91.81	93.42	91.21	80.61	0.940
Xie et al [207]	89.53	84.19	92.02	83.78	0.9665

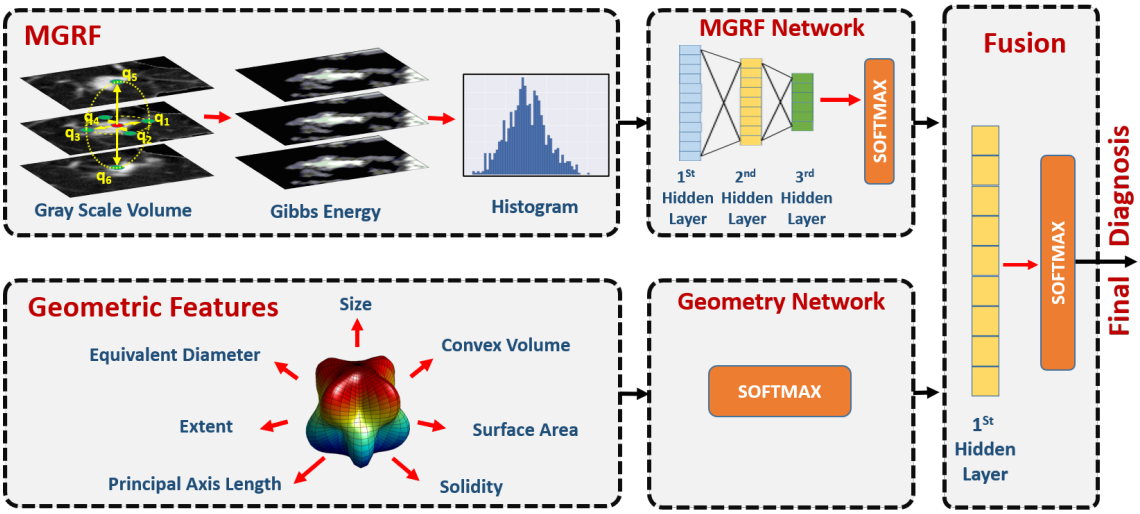

FIGURE 45: The hybrid framework I that integrates the appearance (MGRF) and shape (geometric features) models.

The framework II integrates the Adjustable LBP and MGRF from the appearance models with the spherical harmonics and the fundamental geometric features from the shape models. This framework has been published in the International Symposium on Signal Processing and Information Technology (ISSPIT) conference [64]. This framework is illustrated in Figure 46. Table 14 shows the evaluation metrics to this framework and all its components with comparison to some of other published frameworks that uses the same dataset.

TABLE 14: Evaluation of the hybrid framework II that integrates appearance (MGRF and Adjusted LBP) and shape (spherical harmonics and geometric features) models and its comparison with 4 different recent frameworks that use the same dataset.

	Evaluation Metrics				
	Accuracy	Sensitivity	Specificity	Precision	AUC
Adjusted LBP	91.74	94.62	89.60	87.13	0.9531
MGRF	89.91	93.55	87.20	84.47	0.9666
Spherical Harmonics	89.82	93.55	87.20	84.75	0.9642
Geometric Features	80.73	76.64	84.68	82.83	0.8720
Hybrid Framework II	**92.66**	**95.70**	**90.40**	**88.12**	**0.9636**
Orozco et al [228]	82.00	90.90	73.91	-	0.81
Wei et al [176]	87.65	89.30	86.00	86.45	0.942
Costa et al [229]	91.81	93.42	91.21	80.61	0.940
Xie et al [207]	89.53	84.19	92.02	83.78	0.9665

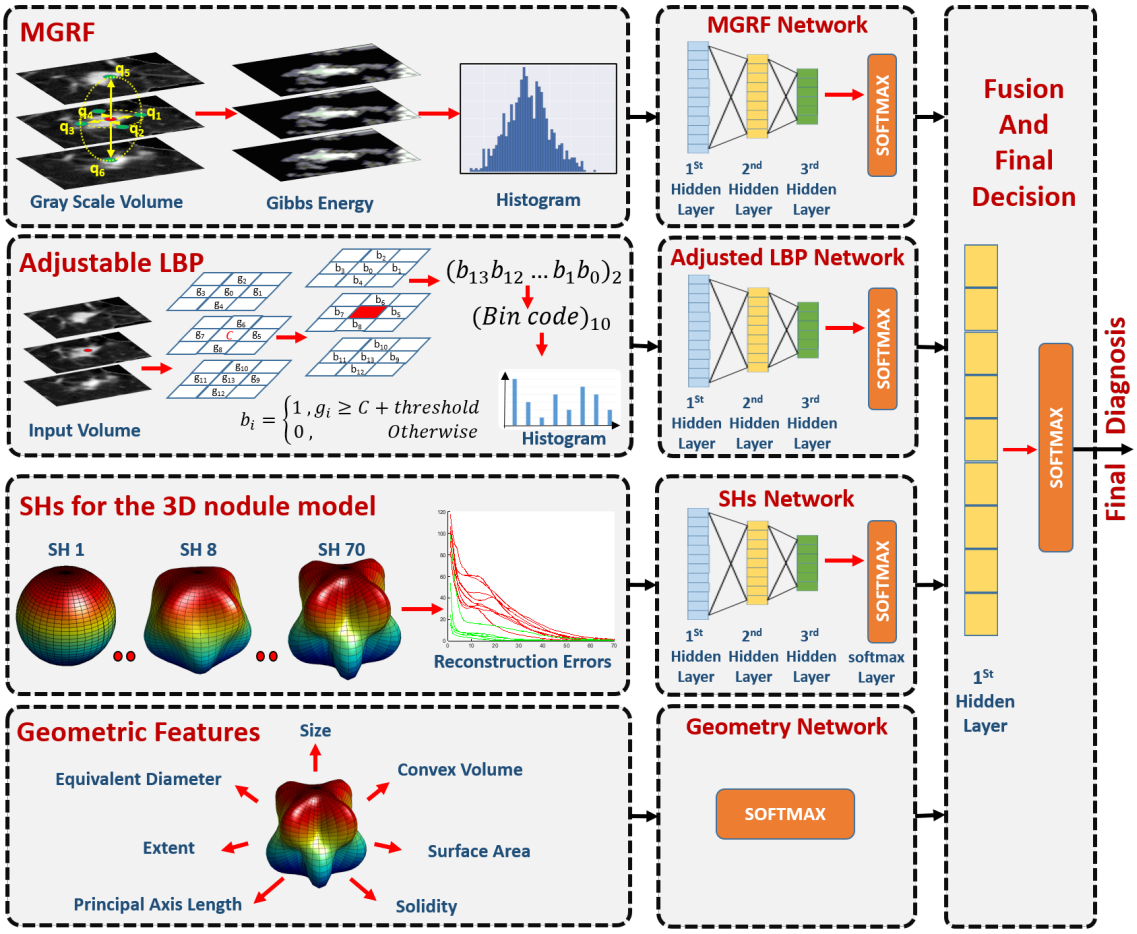

FIGURE 46: The hybrid framework II that integrates the appearance (MGRF and Adjusted LBP) and shape (spherical harmonics and geometric features) models.

The framework III integrates the 3D-HOG and MGRF from the appearance models with the spherical harmonics and the fundamental geometric features from the shape models. This framework has been published in the International Symposium on Biomedical Imaging (ISBI) conference [60]. This framework is illustrated in Figure 47. Table 15 shows the evaluation metrics to this framework and all its components with comparison to some of other published frameworks that uses the same dataset.

TABLE 15: Evaluation of the hybrid framework III that integrates appearance (MGRF and 3D-HOG) and shape (spherical harmonics and geometric features) models and its comparison with 4 different recent frameworks that use the same dataset.

	Evaluation Metrics				
	Accuracy	Sensitivity	Specificity	Precision	AUC
3D-HOG	88.17	87.26	88.86	85.62	0.9462
MGRF	89.91	93.55	87.20	84.47	0.9666
Spherical Harmonics	89.82	93.55	87.20	84.75	0.9642
Geometric Features	80.73	76.64	84.68	82.83	0.8720
Hybrid Framework III	**93.12**	**92.47**	**93.60**	**91.49**	**0.9753**
Orozco et al [228]	82.00	90.90	73.91	-	0.81
Wei et al [176]	87.65	89.30	86.00	86.45	0.942
Costa et al [229]	91.81	93.42	91.21	80.61	0.940
Xie et al [207]	89.53	84.19	92.02	83.78	0.9665

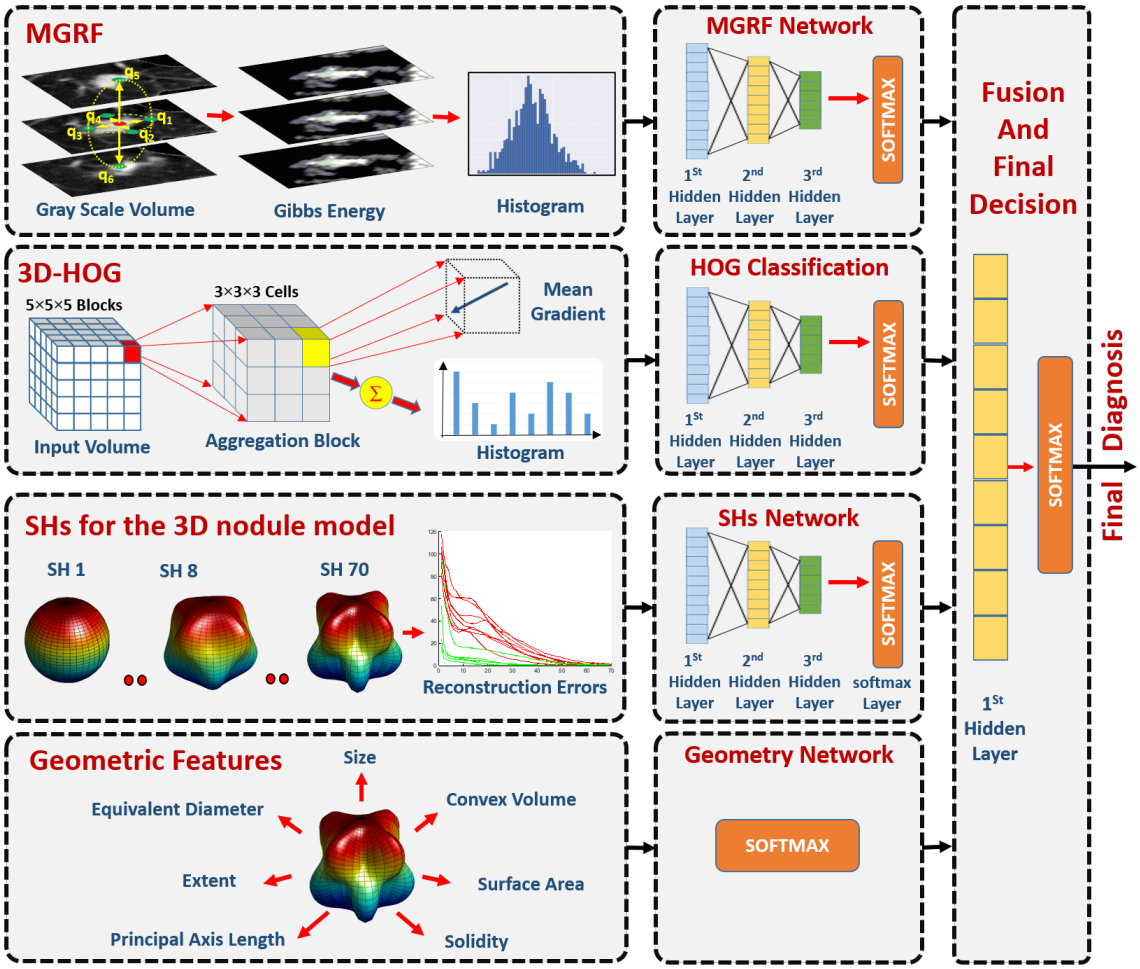

FIGURE 47: The hybrid framework III that integrates the appearance (MGRF and 3D-HOG) and shape (spherical harmonics and geometric features) models.

The framework IV integrates the Multi-view Analytical LBP feature from the appearance models with the spherical harmonics features from the shape models. This framework is illustrated in Figure 48. Table 16 shows the evaluation metrics to this framework and all its components with comparison to some of other published frameworks that uses the same dataset.

TABLE 16: Evaluation of the hybrid framework IV that integrates appearance (Multi-view Analytical LBP) and shape (spherical harmonics) models and its comparison with 4 different recent frameworks that use the same dataset.

	Evaluation Metrics		
	Accuracy	Sensitivity	Specificity
Multi-view ALBP	90.73	90.57	92.19
Spherical Harmonics	89.82	93.55	87.20
Hybrid Framework IV	**93.79**	**94.36**	**92.80**
Gupta et al [230]	81.50	78.11	85.64
Safta et al [166]	93.10	91.11	95.24
Ren et al [201]	90.00	81.00	95.00
Sang et al [189]	92.00	94.00	90.00

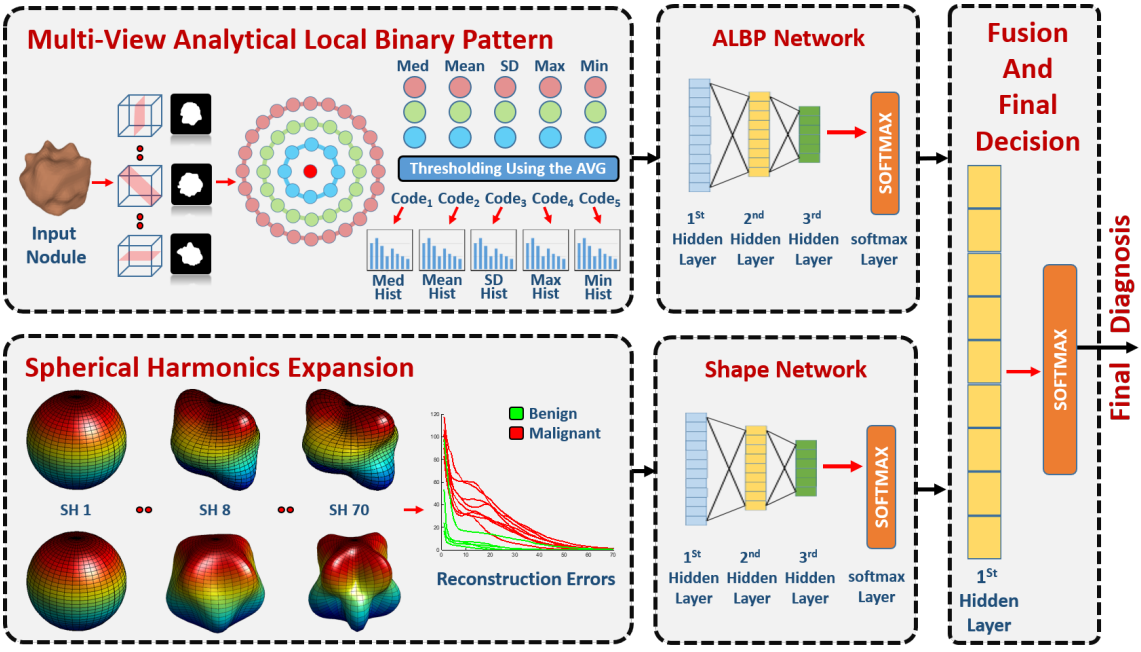

FIGURE 48: The hybrid framework IV that integrates the appearance (Multi-view Analytical LBP) and shape (spherical harmonics) models.

The framework V integrates the 3D-SSIHOG and MGRF from the appearance models with the spherical harmonics and the fundamental geometric features from the shape models. This framework is illustrated in Figure 49. Table 17 shows the evaluation metrics to this framework and all its components with comparison to some of other published frameworks that uses the same dataset.

TABLE 17: Evaluation of the hybrid framework V that integrates appearance (MGRF and 3D-SSIHOG) and shape (spherical harmonics and geometric features) models and its comparison with 5 different recent frameworks that use the same dataset.

	Evaluation Metrics				
	Accuracy	Sensitivity	Specificity	Precision	AUC
3D-SSIHOG	92.66	94.62	91.20	88.89	0.9713
MGRF	89.91	93.55	87.20	84.47	0.9666
Spherical Harmonics	89.82	93.55	87.20	84.75	0.9642
Geometric Features	80.73	76.64	84.68	82.83	0.8720
Hybrid Framework V	**94.50**	**93.55**	**95.20**	**93.55**	**0.9846**
Orozco et al [228]	82.00	90.90	73.91	-	0.81
Wei et al [176]	87.65	89.30	86.00	86.45	0.942
Costa et al [229]	91.81	93.42	91.21	80.61	0.940
Xie et al [207]	89.53	84.19	92.02	83.78	0.9665
Shen et al [205]	84.20	70.50	88.90	-	0.856

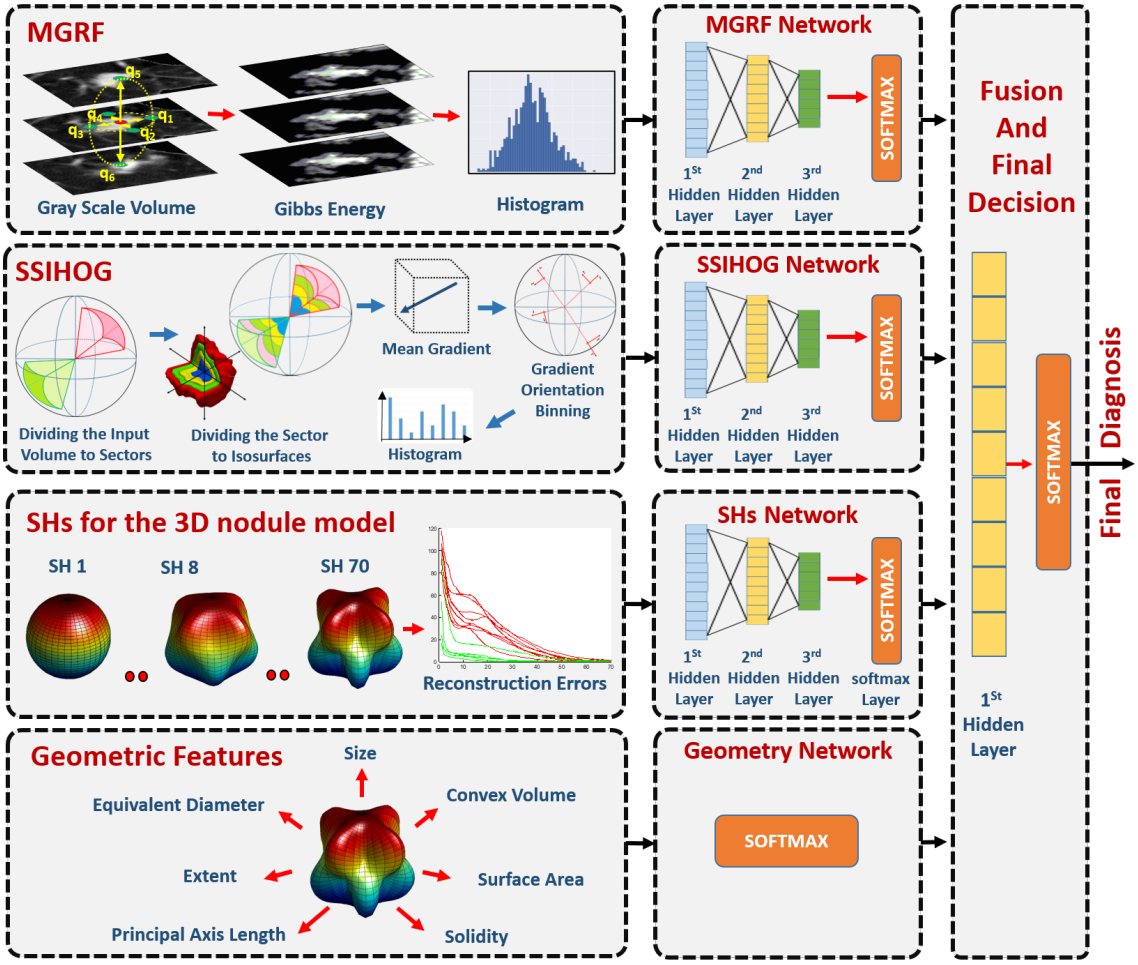

FIGURE 49: The hybrid framework V that integrates the appearance (MGRF and 3D-SSIHOG) and shape (spherical harmonics and geometric features) models.

The framework VI integrates the 3D-SSIHOG from the appearance models with the Multi-view PSCSS from the shape models. This framework has been published in the International Conference on Image Processing (ICIP) [59]. This framework is illustrated in Figure 50. Table 18 shows the evaluation metrics to this framework and all its components with comparison to some of other published frameworks that uses the same dataset.

TABLE 18: Evaluation of the hybrid framework VI that integrates appearance (3D-SSIHOG) and shape (Multi-view PSCSS) models and its comparison with 5 different recent frameworks that use the same dataset.

	Evaluation Metrics			
	Accuracy	Sensitivity	Specificity	AUC
3D-SSIHOG	92.66	94.62	91.20	97.13
Multi-view PSCSS	90.37	89.25	91.20	96.66
Hybrid Framework VI	**94.50**	**95.70**	**93.60**	**98.46**
dey et al [179]	90.40	90.47	90.33	95.48
Wei et al [176]	87.65	89.30	86.00	94.20
Safta et al [165]	91.11	69.79	98.55	96.96
Xie et al [207]	89.53	84.19	92.02	96.65
Shen et al [205]	84.20	70.50	88.90	85.60

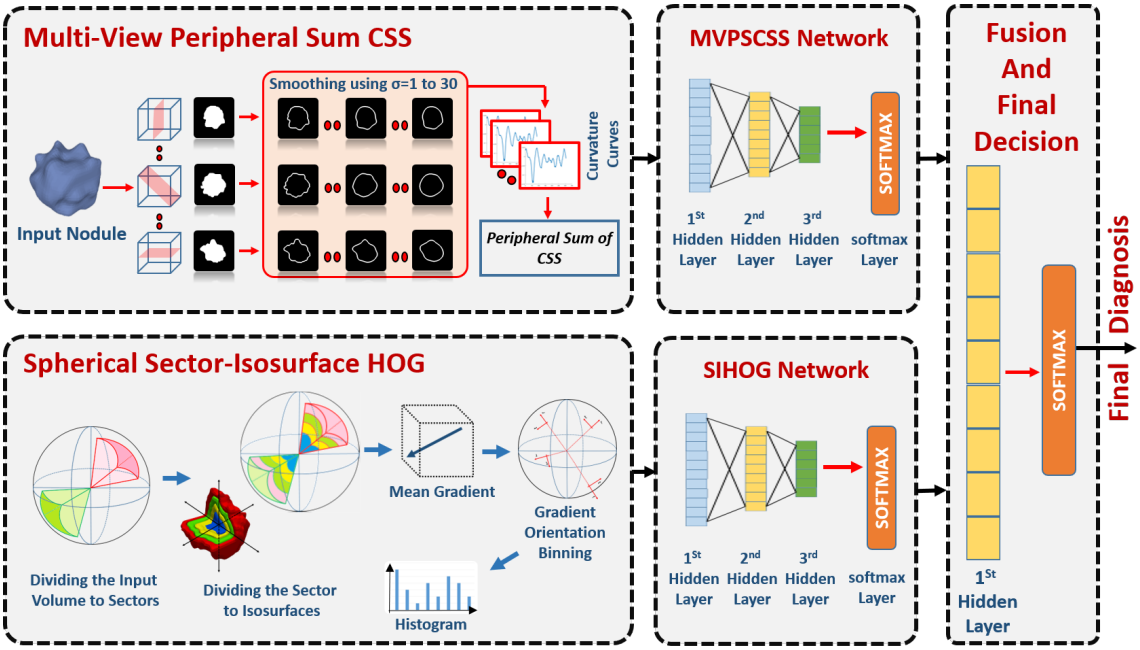

FIGURE 50: The hybrid framework VI that integrates the appearance (3D-SSIHOG) and shape (Multi-view PSCSS) models.

The framework VII integrates the Resolved Ambiguity LBP and MGRF from the appearance models with the spherical harmonics and the fundamental geometric features from the shape models. This framework has been published in the International Conference on Image Processing (ICIP) [61]. This framework is illustrated in Figure 51. Table 19 shows the evaluation metrics to this framework and all its components with comparison to some of other published frameworks that uses the same dataset.

TABLE 19: Evaluation of the hybrid framework VII that integrates appearance (MGRF and Resolved ALBP) and shape (spherical harmonics and geometric features) models and its comparison with 4 different recent frameworks that use the same dataset.

	Evaluation Metrics				
	Accuracy	Sensitivity	Specificity	Precision	AUC
Resolved Ambiguity LBP	92.20	90.32	93.60	91.30	0.9657
MGRF	89.91	93.55	87.20	84.47	0.9666
Spherical Harmonics	89.82	93.55	87.20	84.75	0.9642
Geometric Features	80.73	76.64	84.68	82.83	0.8720
Hybrid Framework VII	**94.95**	**94.62**	**95.20**	**93.62**	**0.9874**
Orozco et al [228]	82.00	90.90	73.91	-	0.81
Wei et al [176]	87.65	89.30	86.00	86.45	0.942
Costa et al [229]	91.81	93.42	91.21	80.61	0.940
Xie et al [207]	89.53	84.19	92.02	83.78	0.9665

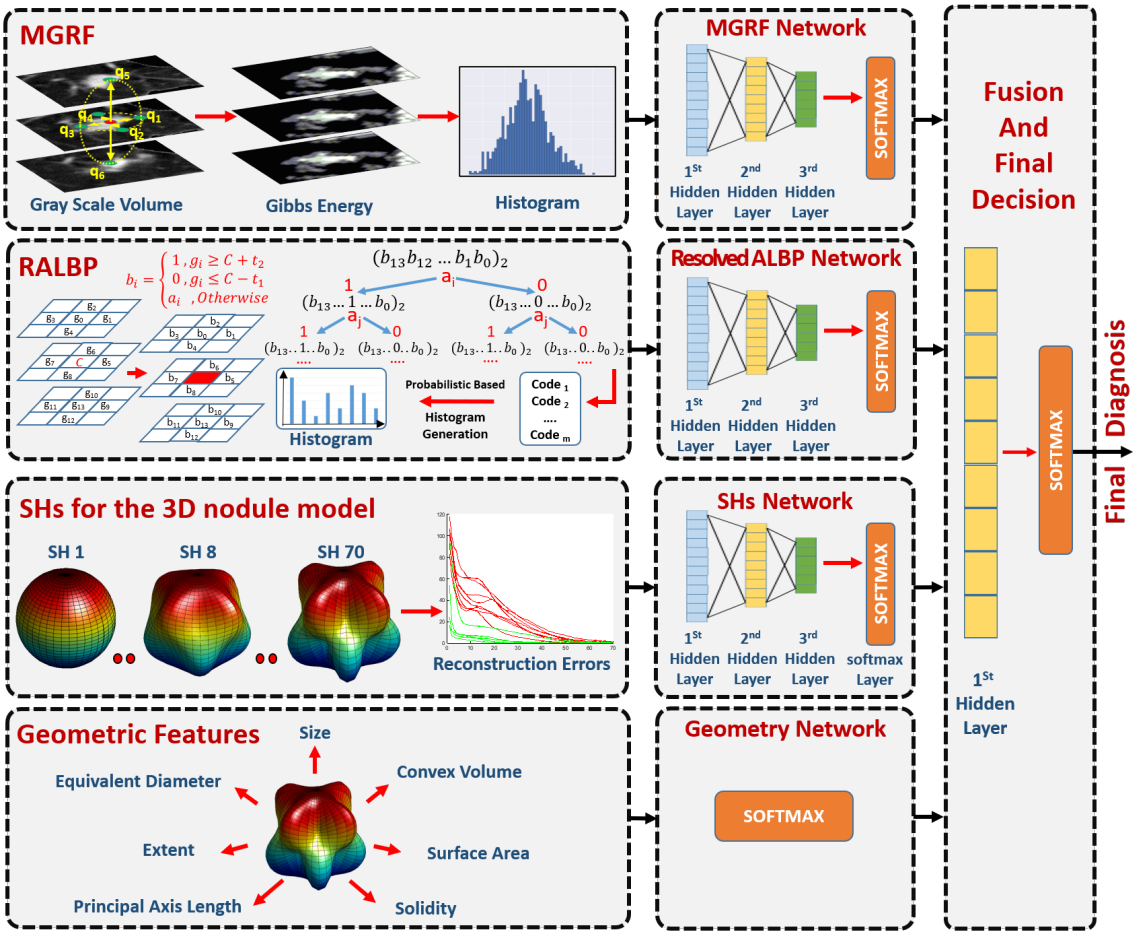

FIGURE 51: The hybrid framework VII that integrates the appearance (MGRF and Resolved ALBP) and shape (spherical harmonics and geometric features) models.

d. The hybrid frameworks integrating the imaging features and clinical bio-markers.

The framework VIII that will be detailed in this section has been published in the Scientific Reports journal [107]. This framework integrates imaging features and breath bio-markers that are obtained from a single exhaled breath to classify the nodules. The locally acquired dataset that is explained in Section IV.A.1.b is utilized for this framework validation. This framework is illustrated in Figure 52. The classification accuracy, sensitivity, and specificity were 97.87%, 97.30%, and 100.00%, respectively. Table 20 shows the classification accuracy, sensitivity, and specificity for each of the different used features

combinations in this framework. Nodule size had the least accuracy and sensitivity while shape and appearance features had the highest accuracy and sensitivity.

TABLE 20: Evaluation of the hybrid framework that integrates imaging markers and clinical bio-marker(breath analysis) models and its different combinations.

	Evaluation Metrics		
	Accuracy	Sensitivity	Specificity
Size	61.19	29.73	100.00
Shape	89.55	89.19	90.00
Appearance	86.57	91.86	80.00
Breath Analysis	75.99	71.43	80.56
Shape + Size	91.04	89.19	93.33
Appearance + Size	89.55	91.89	86.67
Shape + Appearance	91.04	94.59	86.67
Shape + Breath	89.55	89.19	90.00
Appearance + Breath	88.06	91.89	83.33
Size + Breath	79.10	72.97	86.67
Shape + Size + Breath	92.54	91.89	93.33
Shape + Appearance + Breath	92.65	94.74	90.00
Size + Appearance + Breath	92.54	94.59	90.00
Imaging features only	94.03	91.89	96.67
Hybrid Framework VIII	**97.87**	**97.30**	**100.00**

The results of this work demonstrates that combining both breath bio-marker and imaging data will significantly improve the accuracy, sensitivity, and specificity for clinical diagnosis of lung cancer. Importantly, the used breath analysis technology is cost effective (20$ per test) compared to X-Rays. Moreover, breath analysis alone offers 80% nodule

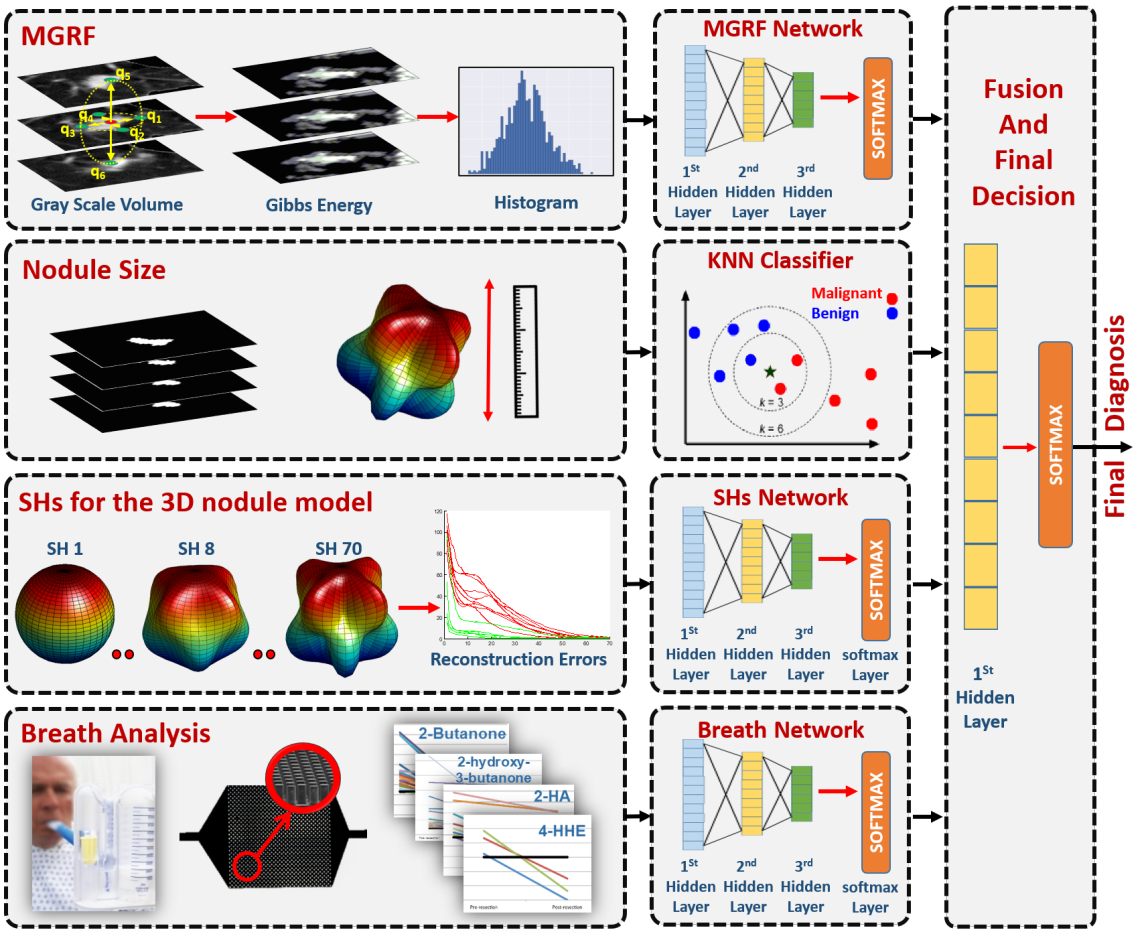

FIGURE 52: The hybrid framework that integrates the imaging markers (MGRF, spherical harmonics, and size) and clinical bio-markers (breath test) models

classification accuracy. Among the other clinical bio-markers the breath test is chose to be integrated with the imaging markers as the organic compounds are volatile in nature, which make the concentration of these compounds higher in the breath compared to other markers (e.g., saliva, urine, and/or blood). In addition, the breath test gives an immediate result as the exhaled breath is collected directly to the bag where the mass spectrometry is used to analyze it. Most importantly, the breath analysis gives a local diagnosis for the lung compared to other bio-markers (e.g., the urine bio-markers will work better for detecting the tumors within the kidney). The sample size of patients with both breath and CT imaging data was limited ($n = 47$) and thus a leave-one-subject-out validation method is used.

4. Results summary

All the developed models give an accurate description for the lung nodules in terms of appearance and shape features. The integration between all the appearance features or shape features separately did not achieve a significant enhancement, while the integration between them boost the framework performance in terms of accuracy, sensitivity, and specificity.

TABLE 21: Evaluation of all the developed hybrid frameworks

	Evaluation Metrics		
	Accuracy	Sensitivity	Specificity
Hybrid Framework I	92.20	92.22	92.19
Hybrid Framework II	92.66	95.70	90.40
Hybrid Framework III	93.12	92.47	93.60
Hybrid Framework IV	93.79	94.36	92.80
Hybrid Framework V	94.50	93.55	95.20
Hybrid Framework VI	94.50	95.70	93.60
Hybrid Framework VII	94.95	94.62	95.20
Hybrid Framework VIII	**97.87**	**97.30**	**100.00**

Table 21 shows all the developed hybrid frameworks evaluation metrics. The hybrid framework VIII has the highest accuracy, sensitivity, and specificity among all the developed frameworks. However, this comparison is unfair, as the hybrid framework VIII is validated using a small size dataset (47 patients), but it shows the ability of integrating the clinical bio-markers to enhance the overall system performance. For imaging features, the hybrid framework VII shows the highest accuracy measure that reach 94.95%.

CHAPTER V
CONCLUSION AND FUTURE WORK

This dissertation presented a non-invasive CAD framework for the diagnosis of the pulmonary nodules malignancy from a single computed tomography scan. It utilize two groups of features, which are appearance (texture) features and shape (contour) features. The experimental results highlighted the ability of theses features to accurately differentiate between the malignant and benign nodules. The main advantages of the proposed system is its ability to diagnose the pulmonary nodules from single computed tomography scan instead of repetitive scans. The extracted features were able to give a good description for the nodule prior growth rate by examining the nodules texture and shape, which is the main point for pulmonary nodule diagnosis. These abilities are very important for this clinical application as it help the radiologists to detect the lung cancer in an early stage. This early detection of lung cancer will significantly improve the effectiveness of treatment and increases the survival rate of the lung cancer patients. The comparison results of the presented framework with the other approaches show that the developed system has promise to reach the accepted clinical accuracy threshold. Moreover, the outline of the major contributions of the theses are as follows:

- A novel and memory-efficient way for speeding up the calculations of the 3D histogram of oriented gradient is proposed. This algorithm is based on the idea of the integral nodule volume to calculate the gradient repeatedly along different dimensions and for different regions. The orientation binning process are done in a general way using a uniform polyhedrons. The number of bins determines the number of the sides in the used polyhedrons.

- An innovative enhancement to the 3D histogram of oriented gradient is implemented and called 3D spherical sector isosurfaces histogram of oriented gradient. The main idea in the proposed enhancement was to divide the nodule volume into central isosurfaces and spherical sectors, considering their intersections as a cell to calculate the mean gradient instead or the original rectangle grid. Moreover, the spherical coordinates is used instead of the ordinary Cartesian coordinates to make the new descriptor a rotation invariant.

- In order to avoid the noise sensitivity in the original local binary pattern, two thresholds were added , t_1 and t_2 to be the lower and the upper bound of the differences of the voxels that will be assigned to 0 and 1 respectively, in addition to an ambiguous state, a, which is assigned to the voxels that are not either 0 or 1. This new proposed coding strategy makes the descriptor less sensitive to the noise and increase its precision in describing the nodule texture.

- An innovative analytical local binary pattern is implemented to compute some information about the distribution of the surrounding pixels' gray levels and compare it to the average of theses information, such as: mean, standard deviation, median, maximum, and minimum to capture the texture appearance of the nodule while reducing the sensitivity of the descriptor to the noise. Moreover, using this statistical information from the surrounding neighbor makes the final descriptor a rotation invariant one without any additional procedure.

- A new Multi-view peripheral sum curvature scale space descriptor is developed to describe the shape complexity of the nodule by calculating the curvature along the nodule contour and count the curvature-zero crossings.

- A fusion network for different classification features based on two stages. The first one generates a primary estimation for every descriptors. Followed by the second stage that consists of an autoencoder with a single layer augmented with a soft-

max classifier that provide us with the final classification of the nodule. This fusion network combined different features, like 7^{th}- order Markov Gibbs random field (MGRF), spherical harmonics expansions, fundamental geometric features, etc.

- A new developed hybrid frameworks that integrate different imaging features and clinical bio-markers for early and accurate diagnosis of lung cancer. This frameworks implies that adding more clinical bio-markers to the diagnosis framework, having a great potential to improve the accuracy of the system.

Several ideas for the future work of this dissertation include, but are not restricted to, the following:

- Integrate the module that classifies between benign and malignant nodules to a full Computer Aided Diagnosis system that contains the lung segmentation, the lung nodules detection and the lung nodules segmentation modules. Integrating all modules will allow to develop a full CAD system for the lung nodules classification.

- Integrate the full CAD system into the CT scanners. This will assist the radiologists in their diagnosis and help them reduce the labor intensive and time consuming that this task require.

- Recruit more patients with both breath and CT data to validate the diagnosis framework on larger datasets.

- Integrate more clinical bio-markers (eg, urine, blood, and saliva) to the CAD system to quantity the effect of their components on lung cancer classification and improve the diagnosis by making it earlier and more accurate.

- As deep learning algorithms emerged and proved their efficiency in multiple applications including medical ones. An orientation for the future work could be to fuse between the developed features in this dissertation and the new deep learning fea-

tures. This fusion between both handcrafted and learned features may improve the results even more.

- The developed CAD system in this dissertation fused between features at the decision level, a new orientation could be to fuse between features at the features level and classify the hole combined feature vector after dimensionality reduction using a single classifier to get the final malignancy score.

REFERENCES

[1] K. Awai, K. Murao, A. Ozawa, M. Komi, H. Hayakawa, S. Hori, and Y. Nishimura. Pulmonary nodules at chest ct: effect of computer-aided diagnosis on radiologists' detection performance. *Radiology*, 230(2):347–352, 2004.

[2] I. Bankman. *Handbook of medical image processing and analysis*. Elsevier, 2008.

[3] American Cancer Society. Cancer Facts and Figures, 2019.

[4] A. Soliman, F. Khalifa, A. Shaffie, N. Liu, N. Dunlap, B. Wang, A. Elmaghraby, G. Gimel'farb, and A. El-Baz. Image-based cad system for accurate identification of lung injury. In *2016 IEEE International Conference on Image Processing (ICIP)*, pages 121–125. IEEE, 2016.

[5] A. Soliman, F. Khalifa, A. Shaffie, N. Dunlap, B. Wang, A. Elmaghraby, and A. El-Baz. Detection of lung injury using 4d-ct chest images. In *2016 IEEE 13th International Symposium on Biomedical Imaging (ISBI)*, pages 1274–1277. IEEE, 2016.

[6] A. Soliman, F. Khalifa, A. Alansary, G. Gimel'farb, and A. El-Baz. Segmentation of lung region based on using parallel implementation of joint mgrf: Validation on 3d realistic lung phantoms. In *2013 IEEE 10th International Symposium on Biomedical Imaging*, pages 864–867. IEEE, 2013.

[7] A. Soliman, F. Khalifa, A. Alansary, G. Gimel'farb, and A. El-Baz. Performance evaluation of an automatic mgrf-based lung segmentation approach. In *AIP Conference Proceedings*, volume 1559, pages 323–332. American Institute of Physics, 2013.

[8] A. Shaffie, A. Soliman, M. Ghazal, F. Taher, N. Dunlap, B. Wang, A. Elmaghraby, G. Gimel'farb, and A. El-Baz. A new framework for incorporating appearance and shape features of lung nodules for precise diagnosis of lung cancer. In *2017 IEEE International Conference on Image Processing (ICIP)*, pages 1372–1376. IEEE, 2017.

[9] E. Hosseini-Asl, J. M. Zurada, and A. El-Baz. Lung segmentation based on nonnegative matrix factorization. In *2014 IEEE International Conference on Image Processing (ICIP)*, pages 877–881. IEEE, 2014.

[10] A. A. Farag, A. El-Baz, G. Gimel'farb, R. Falk, M. A. El-Ghar, T. Eldiasty, and S. Elshazly. Appearance models for robust segmentation of pulmonary nodules in 3d ldct chest images. In *International Conference on Medical Image Computing and Computer-Assisted Intervention*, pages 662–670. Springer, 2006.

[11] A. A. Farag, A. El-Baz, G. G. Gimel'farb, R. Falk, and S. G. Hushek. Automatic detection and recognition of lung abnormalities in helical ct images using deformable templates. In *International Conference on Medical Image Computing and Computer-Assisted Intervention*, pages 856–864. Springer, 2004.

[12] A. El-Baz, F. Khalifa, A. Elnakib, M. Nitzken, A. Soliman, P. McClure, M. Abou El-Ghar, and G. Gimel'farb. A novel approach for global lung registration using 3d markov-gibbs appearance model. In *International Conference on Medical Image Computing and Computer-Assisted Intervention*, pages 114–121. Springer, 2012.

[13] A. El-Baz, A. Soliman, P. McClure, G. Gimel'farb, M. A. El-Ghar, and R. Falk. Early assessment of malignant lung nodules based on the spatial analysis of detected lung nodules. In *2012 9th IEEE international symposium on biomedical imaging (ISBI)*, pages 1463–1466. IEEE, 2012.

[14] A. El-Baz, G. Gimel'farb, M. Abou El-Ghar, and R. Falk. Appearance-based diagnostic system for early assessment of malignant lung nodules. In *2012 19th IEEE International Conference on Image Processing*, pages 533–536. IEEE, 2012.

[15] A. El-Baz, M. Nitzken, F. Khalifa, A. Elnakib, G. Gimel'farb, R. Falk, and M. A. El-Ghar. 3d shape analysis for early diagnosis of malignant lung nodules. In *Biennial International Conference on Information Processing in Medical Imaging*, pages 772–783. Springer, 2011.

[16] A. El-Baz, G. Gimel'farb, R. Falk, and M. El-Ghar. Appearance analysis for diagnosing malignant lung nodules. In *2010 IEEE International Symposium on Biomedical Imaging: From Nano to Macro*, pages 193–196. IEEE, 2010.

[17] A. El-Baz, G. Gimel'farb, R. Falk, M. Abou El-Ghar, S. Rainey, D. Heredia, and T. Shaffer. Toward early diagnosis of lung cancer. In *International Conference on Medical Image Computing and Computer-Assisted Intervention*, pages 682–689. Springer, 2009.

[18] A. El-Baz, G. Gimel'farb, R. Falk, M. Abou El-Ghar, and H. Refaie. Promising results for early diagnosis of lung cancer. In *2008 5th IEEE International Symposium on Biomedical Imaging: From Nano to Macro*, pages 1151–1154. IEEE, 2008.

[19] A. El-Baz, G. Gimel'farb, R. Falk, and M. A. El-Ghar. A new approach for automatic analysis of 3d low dose ct images for accurate monitoring the detected lung nodules. In *2008 19th International Conference on Pattern Recognition*, pages 1–4. IEEE, 2008.

[20] A. El-Baz, G. L. Gimel'farb, R. Falk, T. Holland, and T. Shaffer. A framework for unsupervised segmentation of lung tissues from low dose computed tomography images. In *BMVC*, pages 1–10, 2008.

[21] A. El-Baz, G. Gimel'farb, R. Falk, and M. A. El-Ghar. A novel approach for automatic follow-up of detected lung nodules. In *2007 IEEE International Conference on Image Processing*, volume 5, pages V–501. IEEE, 2007.

[22] A. El-Baz, G. Gimel'farb, R. Falk, and M. A. El-Ghar. A new cad system for early diagnosis of detected lung nodules. In *2007 IEEE International Conference on Image Processing*, volume 2, pages II–461. IEEE, 2007.

[23] A. El-Baz, A. Farag, G. Gimel'farb, R. Falk, M. A. El-Ghar, and T. Eldiasty. A framework for automatic segmentation of lung nodules from low dose chest ct scans. In *18th International Conference on Pattern Recognition (ICPR'06)*, volume 3, pages 611–614. IEEE, 2006.

[24] A. El-Baz, S. E. Yuksel, S. Elshazly, and A. A. Farag. Non-rigid registration techniques for automatic follow-up of lung nodules. In *International Congress Series*, volume 1281, pages 1115–1120. Elsevier, 2005.

[25] A. El-Baz, A. A. Farag, R. Falk, and R. La Rocca. A unified approach for detection, visualization, and identification of lung abnormalities in chest spiral ct scans. In *International Congress Series*, volume 1256, pages 998–1004. Elsevier, 2003.

[26] A. M. Ali, A. S. El-Baz, and A. A. Farag. A novel framework for accurate lung segmentation using graph cuts. In *2007 4th IEEE International Symposium on Biomedical Imaging: From Nano to Macro*, pages 908–911. IEEE, 2007.

[27] B. Abdollahi, A. Soliman, A. Civelek, X.-F. Li, G. Gimel'Farb, and A. El-Baz. A novel gaussian scale space-based joint mgrf framework for precise lung segmentation. In *2012 19th IEEE International Conference on Image Processing*, pages 2029–2032. IEEE, 2012.

[28] A. El-Baz and J. S. Suri. *Lung imaging and computer aided diagnosis*. CRC Press, 2011.

[29] A. Soliman, F. Khalifa, A. Elnakib, M. Abou El-Ghar, N. Dunlap, B. Wang, G. Gimel'farb, R. Keynton, and A. El-Baz. Accurate lungs segmentation on ct chest images by adaptive appearance-guided shape modeling. *IEEE transactions on medical imaging*, 36(1):263–276, 2016.

[30] E. Hosseini-Asl, J. M. Zurada, G. Gimel'farb, and A. El-Baz. 3-d lung segmentation by incremental constrained nonnegative matrix factorization. *IEEE transactions on biomedical engineering*, 63(5):952–963, 2015.

[31] A. El-Baz, G. M. Beache, G. Gimel'farb, K. Suzuki, K. Okada, A. Elnakib, A. Soliman, and B. Abdollahi. Computer-aided diagnosis systems for lung cancer: challenges and methodologies. *International journal of biomedical imaging*, 2013, 2013.

[32] A. El-Baz, A. Elnakib, A. El-Ghar, G. Gimel'farb, R. Falk, A. Farag, et al. Automatic detection of 2d and 3d lung nodules in chest spiral ct scans. *International journal of biomedical imaging*, 2013, 2013.

[33] A. El-Baz, M. Nitzken, G. Gimelfarb, E. Van Bogaert, R. Falk, M. A. El-Ghar, and J. Suri. Three-dimensional shape analysis using spherical harmonics for early assessment of detected lung nodules. *Lung Imaging and Computer Aided Diagnosis*, 19:421–438, 2011.

[34] A. El-Baz, M. Nitzken, E. Vanbogaert, G. Gimel'farb, R. Falk, and M. A. El-Ghar. A novel shape-based diagnostic approach for early diagnosis of lung nodules. In *2011 IEEE International Symposium on Biomedical Imaging: From Nano to Macro*, pages 137–140. IEEE, 2011.

[35] A. El-Baz, P. Sethu, G. Gimel'farb, F. Khalifa, A. Elnakib, R. Falk, and M. A. El-Ghar. Elastic phantoms generated by microfluidics technology: Validation of an imaged-based approach for accurate measurement of the growth rate of lung nodules. *Biotechnology journal*, 6(2):195–203, 2011.

[36] A. El-Baz, G. Gimelfarb, R. Falk, M. A. El-Ghar, and J. Suri. Appearance analysis for the early assessment of detected lung nodules. *Lung imaging and computer aided diagnosis*, 17:395–404, 2011.

[37] A. El-Baz, G. Gimel'farb, R. Falk, and M. A. El-Ghar. Automatic analysis of 3d low dose ct images for early diagnosis of lung cancer. *Pattern Recognition*, 42(6):1041–1051, 2009.

[38] A. S. El-Baz, A. Soliman, M. El-Melegy, and M. Abou El-Ghar. Segmentation of medical images, June 25 2020. US Patent App. 16/628,795.

[39] A. S. El-Baz, A. Soliman, F. Khalifa, A. Shaffie, N. Dunlap, and B. Wang. Accurate detection and assessment of radiation induced lung injury based on a computational model and computed tomography imaging, June 2 2020. US Patent 10,667,778.

[40] A. S. El-Baz, A. Dwyer, R. Ouseph, F. Khalifa, A. Soliman, and M. Shehata. Computer aided diagnostic system for classifying kidneys, October 22 2019. US Patent 10,453,569.

[41] A. S. El-Baz, A. Dwyer, R. Ouseph, F. Khalifa, A. Soliman, and M. Shehata. Computer aided diagnostic system for classifying kidneys, March 27 2018. US Patent 9,928,347.

[42] F. Taher, A. Soliman, H. Kandil, A. Mahmoud, A. Shalaby, G. Gimel'farb, and A. El-Baz. Precise cerebrovascular segmentation. In *2020 IEEE International Conference on Image Processing (ICIP)*, pages 394–397. IEEE, 2020.

[43] A. Soliman, A. Shaffie, M. Ghazal, G. Gimel'farb, R. Keynton, and A. El-Baz. A novel cnn segmentation framework based on using new shape and appearance features. In *2018 25th IEEE International Conference on Image Processing (ICIP)*, pages 3488–3492. IEEE, 2018.

[44] A. Soliman, F. Khalifa, A. Shaffie, N. Dunlap, B. Wang, A. Elmaghraby, G. Gimel'farb, M. Ghazal, and A. El-Baz. A comprehensive framework for early assessment of lung injury. In *2017 IEEE International Conference on Image Processing (ICIP)*, pages 3275–3279. IEEE, 2017.

[45] A. Soliman, F. Khalifa, N. Dunlap, B. Wang, M. Abou El-Ghar, and A. El-Baz. An iso-surfaces based local deformation handling framework of lung tissues. In *2016 IEEE 13th International Symposium on Biomedical Imaging (ISBI)*, pages 1253–1259. IEEE, 2016.

[46] A. Soliman, A. Elnakib, F. Khalifa, M. Abou El-Ghar, and A. El-Baz. Segmentationof pathological lungs from ct chest images. In *2015 IEEE International Conference on Image Processing (ICIP)*, pages 3655–3659. IEEE, 2015.

[47] A. Soliman, M. Abbas, and A. El-Desoky. Schema matching in heterogeneous database. In *Seventh International Engineering Conference*, 2010.

[48] H. Sliman, A. Elnakib, G. M. Beache, A. Soliman, F. Khalifa, G. Gimel'farb, A. Elmaghraby, and A. El-Baz. A novel 4d pde-based approach for accurate assessment of myocardium function using cine cardiac magnetic resonance images. In *2014 IEEE International Conference on Image Processing (ICIP)*, pages 3537–3541. IEEE, 2014.

[49] H. Sliman, F. Khalifa, A. Elnakib, G. Beache, A. Elmaghraby, and A. El-Baz. A new segmentation-based tracking framework for extracting the left ventricle cavity from cine cardiac mri. In *Proceedings of IEEE International Conference on Image Processing,(ICIP'13)*, pages 685–689, 2013.

[50] H. Sliman, F. Khalifa, A. Elnakib, A. Soliman, G. Beache, G. Gimel'farb, A. Emam, A. Elmaghraby, and A. El-Baz. Accurate segmentation framework for the left ventricle wall from cardiac cine mri. In *AIP Conference Proceedings*, volume 1559, pages 287–296. American Institute of Physics, 2013.

[51] A. A. Sleman, A. Soliman, M. Ghazal, H. Sandhu, S. Schaal, A. Elmaghraby, and A. El-Baz. Retinal layers oct scans 3-d segmentation. In *2019 IEEE International Conference on Imaging Systems and Techniques (IST)*, pages 1–6. IEEE, 2019.

[52] A. A. Sleman, A. Eltanboly, A. Soliman, M. Ghazal, H. Sandhu, S. Schaal, R. Keynton, A. Elmaghraby, and A. El-Baz. An innovative 3d adaptive patient-related atlas for automatic segmentation of retina layers from oct images. In *2018 25th IEEE International Conference on Image Processing (ICIP)*, pages 729–733. IEEE, 2018.

[53] M. Shehata, F. Khalifa, A. Soliman, M. Abou El-Ghar, A. Dwyer, G. Gimel'farb, R. Keynton, and A. El-Baz. A promising non-invasive cad system for kidney function assessment. In *International Conference on Medical Image Computing and Computer-Assisted Intervention*, pages 613–621. Springer, Cham, 2016.

[54] M. Shehata, F. Khalifa, E. Hollis, A. Soliman, E. Hosseini-Asl, M. Abou El-Ghar, M. El-Baz, A. C. Dwyer, A. El-Baz, and R. Keynton. A new non-invasive approach for early classification of renal rejection types using diffusion-weighted mri. In *2016 IEEE International Conference on Image Processing (ICIP)*, pages 136–140. IEEE, 2016.

[55] M. Shehata, F. Khalifa, A. Soliman, M. El-Ghar, A. Dwyer, and A. El-Baz. Early assessment of acute renal rejection. In *Proceedings of 12th Annual Scientific Meeting of American Society for Diagnostics and Interventional Nephrology (ASDIN'16)*, pages 19–21, 2016.

[56] M. Shehata, F. Khalifa, A. Soliman, A. Takieldeen, M. Abou El-Ghar, A. Shaffie, A. C. Dwyer, R. Ouseph, A. El-Baz, and R. Keynton. 3d diffusion mri-based cad system for early diagnosis of acute renal rejection. In *2016 IEEE 13th International Symposium on Biomedical Imaging (ISBI)*, pages 1177–1180. IEEE, 2016.

[57] M. Shehata, F. Khalifa, A. Soliman, R. Alrefai, M. Abou El-Ghar, A. C. Dwyer, R. Ouseph, and A. El-Baz. A novel framework for automatic segmentation of kidney from dw-mri. In *2015 IEEE 12th International Symposium on Biomedical Imaging (ISBI)*, pages 951–954. IEEE, 2015.

[58] M. Shehata, F. Khalifa, A. Soliman, R. Alrefai, M. Abou El-Ghar, A. C. Dwyer, R. Ouseph, and A. El-Baz. A level set-based framework for 3d kidney segmentation from diffusion mr images. In *2015 IEEE International Conference on Image Processing (ICIP)*, pages 4441–4445. IEEE, 2015.

[59] A. Shaffie, A. Soliman, H. A. Khalifeh, M. Ghazal, F. Taher, A. Elmaghraby, R. Keynton, and A. El-Baz. A comprehensive framework for accurate classification

of pulmonary nodules. In *2020 IEEE International Conference on Image Processing (ICIP)*, pages 408–412. IEEE, 2020.

[60] A. Shaffie, A. Soliman, H. A. Khalifeh, M. Ghazal, F. Taher, A. Elmaghraby, R. Keynton, and A. El-Baz. Radiomic-based framework for early diagnosis of lung cancer. In *2019 IEEE 16th International Symposium on Biomedical Imaging (ISBI 2019)*, pages 1293–1297. IEEE, 2019.

[61] A. Shaffie, A. Soliman, H. A. Khalifeh, F. Taher, M. Ghazal, N. Dunlap, A. Elmaghraby, R. Keynton, and A. El-Baz. A novel ct-based descriptors for precise diagnosis of pulmonary nodules. In *2019 IEEE International Conference on Image Processing (ICIP)*, pages 1400–1404. IEEE, 2019.

[62] A. Shaffie, A. Soliman, H. A. Khalifeh, F. Taher, M. Ghazal, N. Dunlap, A. Elmaghraby, R. Keynton, and A. El-Baz. A new system for lung cancer diagnosis based on the integration of global and local ct features. In *2019 IEEE International Conference on Imaging Systems and Techniques (IST)*, pages 1–6. IEEE, 2019.

[63] A. Shaffie, A. Soliman, M. Ghazal, F. Taher, N. Dunlap, B. Wang, V. Van Berkel, G. Gimelfarb, A. Elmaghraby, and A. El-Baz. A novel autoencoder-based diagnostic system for early assessment of lung cancer. In *2018 25th IEEE international conference on image processing (ICIP)*, pages 1393–1397. IEEE, 2018.

[64] A. Shaffie, A. Soliman, H. A. Khalifeh, M. Ghazal, F. Taher, R. Keynton, A. Elmaghraby, and A. El-Baz. On the integration of ct-derived features for accurate detection of lung cancer. In *2018 IEEE International Symposium on Signal Processing and Information Technology (ISSPIT)*, pages 435–440. IEEE, 2018.

[65] S. Salahat, A. Soliman, T. McGloughlin, N. Werghi, and A. El-Baz. Segmentation of abdominal aortic aneurysm (aaa) based on topology prior model. In *Annual Conference on Medical Image Understanding and Analysis*, pages 219–228. Springer, Cham, 2017.

[66] M. Mostapha, A. Soliman, F. Khalifa, A. Elnakib, A. Alansary, M. Nitzken, M. F. Casanova, and A. El-Baz. A statistical framework for the classification of infant dt images. In *2014 IEEE International Conference on Image Processing (ICIP)*, pages 2222–2226. IEEE, 2014.

[67] M. Mostapha, A. Alansary, A. Soliman, F. Khalifa, M. Nitzken, R. Khodeir, M. F. Casanova, and A. El-Baz. Atlas-based approach for the segmentation of infant dti mr brain images. In *2014 IEEE 11th International Symposium on Biomedical Imaging (ISBI)*, pages 1255–1258. IEEE, 2014.

[68] M. Mostapha, F. Khalifa, A. Alansary, A. Soliman, G. Gimel'farb, and A. El-Baz. Dynamic mri-based computer aided diagnostic systems for early detection of kidney transplant rejection: A survey. In *AIP Conference Proceedings*, volume 1559, pages 297–306. American Institute of Physics, 2013.

[69] S. Mesbah, A. Shalaby, S. Stills, A. Soliman, A. Willhite, S. Harkema, E. Rejc, and A. El-Baz. A novel automatic segmentation method to quantify the effects of spinal cord injury on human thigh muscles and adipose tissue. In *International Conference on Medical Image Computing and Computer-Assisted Intervention*, pages 703–711. Springer, Cham, 2017.

[70] N. Liu, A. Soliman, G. Gimel'farb, and A. El-Baz. Segmenting kidney dce-mri using 1 st-order shape and 5 th-order appearance priors. In *International Conference on Medical Image Computing and Computer-Assisted Intervention*, pages 77–84. Springer, Cham, 2015.

[71] F. Khalifa, M. Shehata, A. Soliman, M. Abou El-Ghar, T. El-Diasty, A. C. Dwyer, M. El-Melegy, G. Gimel'farb, R. Keynton, and A. El-Baz. A generalized mri-based cad system for functional assessment of renal transplant. In *2017 IEEE 14th International Symposium on Biomedical Imaging (ISBI 2017)*, pages 758–761. IEEE, 2017.

[72] F. Khalifa, A. Soliman, A. C. Dwyer, G. Gimel'farb, and A. El-Baz. A random forest-based framework for 3d kidney segmentation from dynamic contrast-enhanced ct images. In *2016 IEEE International Conference on Image Processing (ICIP)*, pages 3399–3403. IEEE, 2016.

[73] F. Khalifa, A. Soliman, A. Takieldeen, M. Shehata, M. Mostapha, A. Shaffie, R. Ouseph, A. Elmaghraby, and A. El-Baz. Kidney segmentation from ct images using a 3d nmf-guided active contour model. In *2016 IEEE 13th International Symposium on Biomedical Imaging (ISBI)*, pages 432–435. IEEE, 2016.

[74] H. Kandil, A. Soliman, F. Taher, M. Ghazal, M. Hadi, A. Elmaghraby, and A. El-Baz. Analysis of the importance of systolic blood pressure versus diastolic blood pressure in diagnosing hypertension: Mra study. In *2020 IEEE International Conference on Image Processing (ICIP)*, pages 443–447. IEEE, 2020.

[75] H. Kandil, A. Soliman, F. Taher, M. Ghazal, M. Hadi, G. Giridharan, and A. El-Baz. A cad system for the early prediction of hypertension based on changes in cerebral vasculature. In *2019 IEEE International Conference on Imaging Systems and Techniques (IST)*, pages 1–5. IEEE, 2019.

[76] H. Kandil, A. Soliman, F. Taher, A. Mahmoud, A. Elmaghraby, and A. El-Baz. Using 3-d cnns and local blood flow information to segment cerebral vasculature. In *2018 IEEE International Symposium on Signal Processing and Information Technology (ISSPIT)*, pages 701–705. IEEE, 2018.

[77] H. Kandil, A. Soliman, L. Fraiwan, A. Shalaby, A. Mahmoud, A. ElTanboly, A. Elmaghraby, G. Giridharan, and A. El-Baz. A novel mra framework based on integrated global and local analysis for accurate segmentation of the cerebral vascular system. In *2018 IEEE 15th International Symposium on Biomedical Imaging (ISBI 2018)*, pages 1365–1368. IEEE, 2018.

[78] M. Ismail, A. Soliman, A. ElTanboly, A. Switala, M. Mahmoud, F. Khalifa, G. Gimel'farb, M. F. Casanova, R. Keynton, and A. El-Baz. Detection of white matter abnormalities in mr brain images for diagnosis of autism in children. In *2016 IEEE 13th International Symposium on Biomedical Imaging (ISBI)*, pages 6–9. IEEE, 2016.

[79] M. Ismail, M. Mostapha, A. Soliman, M. Nitzken, F. Khalifa, A. Elnakib, G. Gimel'farb, M. Casanova, and A. El-Baz. Segmentation of infant brain mr images based on adaptive shape prior and higher-order mgrf. In *2015 IEEE International Conference on Image Processing (ICIP)*, pages 4327–4331. IEEE, 2015.

[80] K. Hammouda, F. Khalifa, A. Soliman, H. Abdeltawab, M. Ghazal, M. Abou El-Ghar, A. Haddad, H. E. Darwish, R. Keynton, and A. El-Baz. A 3d cnn with a learnable adaptive shape prior for accurate segmentation of bladder wall using mr images. In *2020 IEEE 17th International Symposium on Biomedical Imaging (ISBI)*, pages 935–938. IEEE, 2020.

[81] K. Hammouda, F. Khalifa, A. Soliman, M. Ghazal, M. Abou El-Ghar, A. Haddad, M. Elmogy, H. Darwish, R. Keynton, and A. El-Baz. A deep learning-based approach for accurate segmentation of bladder wall using mr images. In *2019 IEEE International Conference on Imaging Systems and Techniques (IST)*, pages 1–6. IEEE, 2019.

[82] K. Hammouda, F. Khalifa, A. Soliman, M. Ghazal, M. Abou El-Ghar, et al. A cnn-based framework for bladder wall segmentation using mri. In *2019 Fifth International Conference on Advances in Biomedical Engineering (ICABME)*, pages 1–4. IEEE, 2019.

[83] Y. ElNakieb, O. Dekhil, M. Ali, A. Shalaby, A. Soliman, A. Mahmoud, R. Keynton, M. Ghazal, G. Barnes, and A. S. El-Baz. Autism diagnosis framework using diffusion tensor imaging. In *INSAR 2020 Virtual Meeting*. INSAR.

[84] Y. ElNakieb, A. Soliman, A. Mahmoud, O. Dekhil, A. Shalaby, et al. Autism spectrum disorder diagnosis framework using diffusion tensor imaging. In *2019 IEEE International Conference on Imaging Systems and Techniques (IST)*, pages 1–5. IEEE, 2019.

[85] Y. ElNakieb, M. T. Ali, O. Dekhil, M. E. Khalefa, A. Soliman, et al. Towards accurate personalized autism diagnosis using different imaging modalities: smri, fmri, and dti. In *2018 IEEE International Symposium on Signal Processing and Information Technology (ISSPIT)*, pages 447–452. IEEE, 2018.

[86] A. El Tanboly, M. Ismail, A. Switala, M. Mahmoud, A. Soliman, et al. A novel automatic segmentation of healthy and diseased retinal layers from oct scans. In *2016 IEEE International Conference on Image Processing (ICIP)*, pages 116–120. IEEE, 2016.

[87] A. El-Baz, A. Soliman, P. McClure, G. Gimel'farb, M. El-Ghar, R. Falk, F. Khalifa, and G. Beache. Research publications, creative works and other research outputs. In *Symposium on Biomedical Imaging (ISBI)*, volume 1463, page 1466, 2012.

[88] A. Alansary, A. Soliman, M. Nitzken, F. Khalifa, A. Elnakib, M. Mostapha, M. F. Casanova, and A. El-Baz. An integrated geometrical and stochastic approach for accurate infant brain extraction. In *2014 IEEE International Conference on Image Processing (ICIP)*, pages 3542–3546. IEEE, 2014.

[89] A. A. Sleman, A. Soliman, A. H. Mahmoud, M. Ghazal, H. Sandhu, S. Schaal, A. Elmaghraby, and A. El-Baz. Segmentation of retinal layers from oct scans. In *Diabetes and Retinopathy*, pages 109–132. Elsevier, 2020.

[90] M. Mostapha, F. Khalifa, A. Alansary, A. Soliman, J. Suri, and A. S. El-Baz. Computer-aided diagnosis systems for acute renal transplant rejection: Challenges and methodologies. In *Abdomen and Thoracic Imaging*, pages 1–35. Springer, Boston, MA, 2014.

[91] A. Elnakib, M. F. Casanova, A. Soliman, G. Gimel'farb, and A. El-Baz. Analysis of 3d corpus callosum images in the brains of autistic individuals. In *Handbook of Research on Trends in the Diagnosis and Treatment of Chronic Conditions*, pages 159–184. IGI Global, 2016.

[92] F. Taher, A. Soliman, H. Kandil, A. Mahmoud, A. Shalaby, G. Gimel'farb, and A. El-Baz. Accurate segmentation of cerebrovasculature from tof-mra images using appearance descriptors. *IEEE Access*, 8:96139–96149, 2020.

[93] A. Soliman, F. Khalifa, A. Elnakib, and A. S. El-Baz. Map-based framework for segmentation of mr brain images based on visual appearance and prior shape.

[94] A. Soliman, F. Khalifa, A. Shaffie, A. Mahmoud, N. Dunlap, et al. Early assessment of radiation-induced lung injury. *Lung Imaging and CADx*, page 349, 2019.

[95] A. Soliman, M. Ismail, A. T. Eldeen, G. Gimel'farb, A. El-Baz, and R. Keynton. Robust image segmentation with a parametric deformable model using learned shape priors. *Biomedical Image Segmentation: Advances and Trends*, page 77, 2016.

[96] A. Soliman, P. McClure, F. Khalifa, A. Takieldeen, M. Abou El-Ghar, T. El-Diasty, J. S. Suri, A. Elmaghraby, and A. El-Baz. A novel nmf-based cad system for early diagnosis of prostate cancer by using 4-d diffusion-weighted magnetic resonance images (dw-mri). *Biomedical Image Segmentation: Advances and Trends*, page 313, 2016.

[97] A. S. N. Soliman. Computational methods for the analysis of functional 4d-ct chest images. 2016.

[98] A. Soliman, P. McClure, F. Khalifa, A. T. Eldeen, M. Abou El-Ghar, T. El-Diasty, J. S. Suri, A. Elmaghraby, and A. El-Baz. chapter fourteen. *Biomedical Image Segmentation: Advances and Trends*, 2016.

[99] A. Soliman and A. El-Desoky. Schema matching in heterogeneous database. *Al-Azhar University Engineering Journal, JAUES*, 3(17):372–379, 2008.

[100] H. Sliman, F. Khalifa, A. Elnakib, A. Soliman, A. El-Baz, G. M. Beache, A. Elmaghraby, and G. Gimel'farb. Myocardial borders segmentation from cine mr images using bidirectional coupled parametric deformable models. *Medical physics*, 40(9):092302, 2013.

[101] A. A. Sleman, A. Soliman, M. Elsharkawy, G. Giridharan, M. Ghazal, H. Sandhu, S. Schaal, R. Keynton, A. Elmaghraby, and A. El-Baz. A novel 3d segmentation approach for extracting retinal layers from optical coherence tomography images. *Medical Physics*.

[102] M. Shehata, F. Khalifa, A. Soliman, M. Ghazal, F. Taher, M. Abou El-Ghar, A. C. Dwyer, G. Gimel'farb, R. S. Keynton, and A. El-Baz. Computer-aided diagnostic system for early detection of acute renal transplant rejection using diffusion-weighted mri. *IEEE Transactions on Biomedical Engineering*, 66(2):539–552, 2018.

[103] M. Shehata, A. Mahmoud, A. Soliman, F. Khalifa, M. Ghazal, M. Abou El-Ghar, M. El-Melegy, and A. El-Baz. 3d kidney segmentation from abdominal diffusion mri using an appearance-guided deformable boundary. *PloS one*, 13(7):e0200082, 2018.

[104] M. Shehata, F. Khalifa, A. Soliman, A. T. Eldeen, M. El-Ghar, T. El-Diasty, A. El-Baz, and R. Keynton. An appearance-guided deformable model for 4d kidney segmentation using diffusion mri. *Biomedical Image Segmentation: Advances and Trends*, page 271, 2016.

[105] A. Sharafeldeen, M. Elsharkawy, F. Khalifa, A. Soliman, M. Ghazal, et al. Precise higher-order reflectivity and morphology models for early diagnosis of diabetic retinopathy using oct images. *Scientific Reports*, 11(1):1–16, 2021.

[106] A. Shaffie, A. Soliman, A. Mahmoud, H. A. Khalifeh, F. Taher, M. Ghazal, A. Elmaghraby, and A. El-Baz. Early diagnosis system for lung nodules based on the integration of a higher-order mgrf appearance feature model and 3d-cnn.

[107] A. Shaffie, A. Soliman, X.-A. Fu, M. Nantz, G. Giridharan, V. van Berkel, H. A. Khalifeh, M. Ghazal, A. Elmaghraby, and A. El-Baz. A novel technology to integrate imaging and clinical markers for non-invasive diagnosis of lung cancer. *Scientific reports*, 11(1):1–10, 2021.

[108] A. Shaffie, A. Soliman, A. Mahmoud, M. Ghazal, H. Hajjdiab, R. Keynton, G. Giridharan, A. Elmaghraby, J. S. Suri, and A. El-Baz. Lung nodule classification based on the integration of a higher-order markov-gibbs random field appearance model and geometric features. *Lung Imaging and CADx*, page 203, 2019.

[109] A. Shaffie, A. Soliman, L. Fraiwan, M. Ghazal, F. Taher, et al. A generalized deep learning-based diagnostic system for early diagnosis of various types of pulmonary nodules. *Technology in cancer research & treatment*, 17:1533033818798800, 2018.

[110] S. Schaal, M. Ismail, A. C. Palacio, A. ElTanboly, A. Switala, et al. Subtle early changes in diabetic retinas revealed by a novel method that automatically quantifies spectral domain optical coherence tomography (sd-oct) images. *Investigative Ophthalmology & Visual Science*, 57(12):6324–6324, 2016.

[111] S. Salahat, A. Soliman, H. Bhaskar, T. McGloughlin, A. El-Baz, and N. Werghi. 9 detection of calcification from abdominal aortic aneurysm. *Cardiovascular Imaging and Image Analysis*, page 173, 2018.

[112] A. K. Rudra, A. S. Chowdhury, A. Elnakib, F. Khalifa, A. Soliman, G. Beache, and A. El-Baz. Kidney segmentation using graph cuts and pixel connectivity. *Pattern Recognition Letters*, 34(13):1470–1475, 2013.

[113] T. Neyer, A. ElTanboly, A. C. Palacio, M. Ismail, A. Switala, et al. A novel automated method for the objective quantification of retinal layers based on spectral domain optical coherence tomography (sd-oct) imaging reveals sequential changes in the normal retina with age. *Investigative Ophthalmology & Visual Science*, 57(12):5943–5943, 2016.

[114] S. Mesbah, A. M. Shalaby, S. Stills, A. M. Soliman, A. Willhite, S. J. Harkema, E. Rejc, and A. S. El-Baz. Novel stochastic framework for automatic segmentation of human thigh mri volumes and its applications in spinal cord injured individuals. *PloS one*, 14(5):e0216487, 2019.

[115] S. Mesbah, A. M. Shalaby, S. Stills, A. Soliman, A. Willhite, S. J. Harkema, E. Rejc, and A. S. El-Baz. Correction: Novel stochastic framework for automatic segmentation of human thigh mri volumes and its applications in spinal cord injured individuals. *Plos one*, 14(7):e0219810, 2019.

[116] P. McClure, A. Elnakib, M. A. El-Ghar, F. Khalifa, A. Soliman, T. El-Diasty, J. S. Suri, A. Elmaghraby, and A. El-Baz. In-vitro and in-vivo diagnostic techniques for prostate cancer: a review. *Journal of biomedical nanotechnology*, 10(10):2747–2777, 2014.

[117] P. McClure, F. Khalifa, A. Soliman, M. El-Ghar, G. Gimelfarb, A. Elmagraby, and A. El-Baz. A novel nmf guided level-set for dwi prostate segmentation. *Journal of Computer Science & Systems Biology*, 7(6):209–216, 2014.

[118] F. Khalifa, A. Soliman, A. Elmaghraby, G. Gimel'farb, and A. El-Baz. 3d kidney segmentation from abdominal images using spatial-appearance models. *Computational and mathematical methods in medicine*, 2017, 2017.

[119] F. Khalifa, A. Soliman, A. El-Baz, M. Abou El-Ghar, T. El-Diasty, G. Gimel'farb, R. Ouseph, and A. C. Dwyer. Models and methods for analyzing dce-mri: A review. *Medical physics*, 41(12):124301, 2014.

[120] H. Kandil, A. Soliman, A. Mahmoud, A. Shalaby, F. Taher, M. Ghazal, A. Elmagraby, and A. El-Baz. Novel approaches for segmenting cerebral vasculature.

[121] H. Kandil, A. Soliman, F. Taher, M. Ghazal, A. Khalil, G. Giridharan, R. Keynton, J. R. Jennings, and A. El-Baz. A novel computer-aided diagnosis system for the early detection of hypertension based on cerebrovascular alterations. *NeuroImage: Clinical*, 25:102107, 2020.

[122] H. Kandil, A. Soliman, M. Ghazal, A. Mahmoud, A. Shalaby, R. Keynton, A. Elmaghraby, G. Giridharan, and A. El-Baz. A novel framework for early detection of hypertension using magnetic resonance angiography. *Scientific reports*, 9(1):1–12, 2019.

[123] H. Kandil, D. Sosnin, A. Mahmoud, A. Shalaby, A. Soliman, A. Elmaghraby, J. Suri, G. Giridharan, and A. El-Baz. 16 hypertension and correlation to cerebrovascular change: A brief overview. *Cardiovascular Imaging and Image Analysis*, page 345, 2018.

[124] M. Ismail, A. Soliman, M. Ghazal, A. E. Switala, G. Gimel'farb, G. N. Barnes, A. Khalil, and A. El-Baz. A fast stochastic framework for automatic mr brain images segmentation. *PloS one*, 12(11):e0187391, 2017.

[125] M. A. Ghazal, A. Mahmoud, A. Aslantas, A. Soliman, A. Shalaby, J. A. Benediktsson, and A. El-Baz. Vegetation cover estimation using convolutional neural networks. *IEEE Access*, 7:132563–132576, 2019.

[126] A. ElTanboly, A. Soliman, A. Sleman, H. Sandhu, A. El-Baz, S. Schaal, et al. Automated 3-d segmentation of retinal layers from optical coherence tomography images using pattern recognition-based method. *Investigative Ophthalmology & Visual Science*, 59(9):1685–1685, 2018.

[127] Y. A. Elnakieb, M. T. Ali, A. Soliman, A. H. Mahmoud, A. M. Shalaby, et al. Computer aided autism diagnosis using diffusion tensor imaging. *IEEE Access*, 8:191298–191308, 2020.

[128] A. Elnakib, A. Soliman, M. Nitzken, M. F. Casanova, G. Gimel'farb, and A. El-Baz. Magnetic resonance imaging findings for dyslexia: a review. *Journal of biomedical nanotechnology*, 10(10):2778–2805, 2014.

[129] A. El-Baz, A. Elnakib, F. Khalifa, M. Abou El-Ghar, P. McClure, A. Soliman, and G. Gimelrfarb. Precise segmentation of 3-d magnetic resonance angiography. *IEEE Transactions on Biomedical Engineering*, 59(7):2019–2029, 2012.

[130] O. Dekhil, A. Mahmoud, A. Shalaby, A. Soliman, F. Taher, et al. Computational analysis techniques: a case study on fmri for autism spectrum disorder.

[131] O. Dekhil, A. Shalaby, A. Soliman, A. Mahmoud, M. Kong, G. Barnes, A. Elmaghraby, and A. El-Baz. Identifying brain areas correlated with ados raw scores by studying altered dynamic functional connectivity patterns. *Medical Image Analysis*, 68:101899, 2021.

[132] O. Dekhil, M. Ali, Y. El-Nakieb, A. Shalaby, A. Soliman, et al. A personalized autism diagnosis cad system using a fusion of structural mri and resting-state functional mri data. *Frontiers in psychiatry*, 10:392, 2019.

[133] M. F. Casanova, A. S. El-Baz, S. S. Kamat, B. A. Dombroski, F. Khalifa, A. Elnakib, A. Soliman, A. Allison-McNutt, and A. E. Switala. Focal cortical dysplasias in autism spectrum disorders. *Acta neuropathologica communications*, 1(1):1–11, 2013.

[134] M. Ali, A. Saad, A. Soliman, S. Rafrafi-Nouira, and C. Capape. Confirmed occurrence in the mediterranean sea of the red sea orange face butterflyfish chaetodon larvatus (osteichthyes: Chaetodontidae) and first record from the syrian coast. *Cahiers de Biologie Marine*, 58(3):367–369, 2017.

[135] A. Alansary, M. Nitzken, A. Black, A. Elnakib, F. Khalifa, K. Stinebruner, A. Soliman, M. Mostapha, M. Casanova, and A. El-Baz. Brain surface analysis for dementia diagnosis.

[136] A. Alansary, M. Ismail, A. Soliman, F. Khalifa, M. Nitzken, et al. Infant brain extraction in t1-weighted mr images using bet and refinement using lcdg and mgrf models. *IEEE journal of biomedical and health informatics*, 20(3):925–935, 2015.

[137] A. Alansary, A. Soliman, F. Khalifa, A. Elnakib, M. Mostapha, M. Nitzken, M. Casanova, and A. El-Baz. Map-based framework for segmentation of mr brain images based on visual appearance and prior shape. *MIDAS J*, 1:1, 2013.

[138] S. Ahmed, A. Soliman, F. Xiao-An, M. Nantz, G. Guruprasad, H. A. Khalifeh, M. Ghazal, E. Adel, A. El-baz, et al. A novel technology to integrate imaging and clinical markers for non-invasive diagnosis of lung cancer. *Scientific Reports (Nature Publisher Group)*, 11(1), 2021.

[139] Q. Hu, L. F. d. F. Souza, G. B. Holanda, S. S. Alves, F. H. d. S. Silva, T. Han, and P. P. Reboucas Filho. An effective approach for ct lung segmentation using mask

region-based convolutional neural networks. *Artificial intelligence in medicine*, 103:101792, 2020.

[140] C. Liu and M. Pang. Automatic lung segmentation based on image decomposition and wavelet transform. *Biomedical Signal Processing and Control*, 61:102032, 2020.

[141] A. Comelli, C. Coronnello, N. Dahiya, V. Benfante, S. Palmucci, A. Basile, C. Vancheri, G. Russo, A. Yezzi, and A. Stefano. Lung segmentation on high-resolution computerized tomography images using deep learning: A preliminary step for radiomics studies. *Journal of Imaging*, 6(11):125, 2020.

[142] J. Hofmanninger, F. Prayer, J. Pan, S. Röhrich, H. Prosch, and G. Langs. Automatic lung segmentation in routine imaging is primarily a data diversity problem, not a methodology problem. *European Radiology Experimental*, 4(1):1–13, 2020.

[143] J. Tan, L. Jing, Y. Huo, L. Li, O. Akin, and Y. Tian. Lgan: Lung segmentation in ct scans using generative adversarial network. *Computerized Medical Imaging and Graphics*, 87:101817, 2021.

[144] Y. Su, D. Li, and X. Chen. Lung nodule detection based on faster r-cnn framework. *Computer Methods and Programs in Biomedicine*, page 105866, 2020.

[145] M. Toğaçar, B. Ergen, and Z. Cömert. Detection of lung cancer on chest ct images using minimum redundancy maximum relevance feature selection method with convolutional neural networks. *Biocybernetics and Biomedical Engineering*, 40(1):23–39, 2020.

[146] K. Suzuki, Y. Otsuka, Y. Nomura, K. K. Kumamaru, R. Kuwatsuru, and S. Aoki. Development and validation of a modified three-dimensional u-net deep-learning model for automated detection of lung nodules on chest ct images from the lung image database consortium and japanese datasets. *Academic Radiology*, 2020.

[147] H. Cao, H. Liu, E. Song, G. Ma, X. Xu, R. Jin, T. Liu, and C.-C. Hung. A two-stage convolutional neural networks for lung nodule detection. *IEEE journal of biomedical and health informatics*, 24(7):2006–2015, 2020.

[148] B. K. Veronica. An effective neural network model for lung nodule detection in ct images with optimal fuzzy model. *Multimedia Tools and Applications*, pages 1–21, 2020.

[149] H. Cao, H. Liu, E. Song, C.-C. Hung, G. Ma, X. Xu, R. Jin, and J. Lu. Dual-branch residual network for lung nodule segmentation. *Applied Soft Computing*, 86:105934, 2020.

[150] N. V. Keetha, C. S. R. Annavarapu, et al. U-det: A modified u-net architecture with bidirectional feature network for lung nodule segmentation. *arXiv preprint arXiv:2003.09293*, 2020.

[151] X. Dong, S. Xu, Y. Liu, A. Wang, M. I. Saripan, L. Li, X. Zhang, and L. Lu. Multi-view secondary input collaborative deep learning for lung nodule 3d segmentation. *Cancer Imaging*, 20(1):1–13, 2020.

[152] M. H. Hesamian, W. Jia, X. He, Q. Wang, and P. J. Kennedy. Synthetic ct images for semi-sequential detection and segmentation of lung nodules. *Applied Intelligence*, pages 1–13, 2020.

[153] Z. Xiao, B. Liu, L. Geng, F. Zhang, and Y. Liu. Segmentation of lung nodules using improved 3d-unet neural network. *Symmetry*, 12(11):1787, 2020.

[154] M. V. K. Likhitkar, U. Gawande, and M. K. O. Hajari. Automated detection of cancerous lung nodule from the computed tomography images. *IOSR Journal of Computer Engineering*, 16(1):05–11, 2014.

[155] F. V. Farahani, A. Ahmadi, and M. F. Zarandi. Lung nodule diagnosis from ct images based on ensemble learning. In *Computational Intelligence in Bioinformatics and Computational Biology (CIBCB), 2015 IEEE Conference on*, pages 1–7. IEEE, 2015.

[156] S. G. Armato III, G. McLennan, L. Bidaut, M. F. McNitt-Gray, C. R. Meyer, et al. The lung image database consortium (lidc) and image database resource initiative (idri): a completed reference database of lung nodules on ct scans. *Medical physics*, 38(2):915–931, 2011.

[157] M. Firmino, G. Angelo, H. Morais, M. R. Dantas, and R. Valentim. Computer-aided detection (cade) and diagnosis (cadx) system for lung cancer with likelihood of malignancy. *Biomedical engineering online*, 15(1):1–17, 2016.

[158] T. N. Shewaye and A. A. Mekonnen. Benign-malignant lung nodule classification with geometric and appearance histogram features. *arXiv preprint arXiv:1605.08350*, 2016.

[159] J. Jeeva et al. A computer aided diagnosis for detection and classification of lung nodules. In *Intelligent Systems and Control (ISCO), 2015 IEEE 9th International Conference on*, pages 1–5. IEEE, 2015.

[160] P.-W. Huang, P.-L. Lin, C.-H. Lee, and C. Kuo. A classification system of lung nodules in ct images based on fractional brownian motion model. In *2013 International conference on system science and engineering (ICSSE)*, pages 37–40. IEEE, 2013.

[161] F. Han, H. Wang, G. Zhang, H. Han, B. Song, L. Li, W. Moore, H. Lu, H. Zhao, and Z. Liang. Texture feature analysis for computer-aided diagnosis on pulmonary nodules. *Journal of digital imaging*, 28(1):99–115, 2015.

[162] Z. Wang, J. Xin, P. Sun, Z. Lin, Y. Yao, and X. Gao. Improved lung nodule diagnosis accuracy using lung ct images with uncertain class. *Computer methods and programs in biomedicine*, 162:197–209, 2018.

[163] M. Nishio, O. Sugiyama, M. Yakami, S. Ueno, T. Kubo, T. Kuroda, and K. Togashi. Computer-aided diagnosis of lung nodule classification between benign nodule, primary lung cancer, and metastatic lung cancer at different image size using deep convolutional neural network with transfer learning. *PloS one*, 13(7):e0200721, 2018.

[164] R. Arulmurugan and H. Anandakumar. Early detection of lung cancer using wavelet feature descriptor and feed forward back propagation neural networks classifier. In *Computational Vision and Bio Inspired Computing*, pages 103–110. Springer, 2018.

[165] W. Safta and H. Frigui. Multiple instance learning for benign vs. malignant classification of lung nodules in ct scans. In *2018 IEEE International Symposium on Signal Processing and Information Technology (ISSPIT)*, pages 490–494. IEEE, 2018.

[166] W. Safta, M. M. Farhangi, B. Veasey, A. Amini, and H. Frigui. Multiple instance learning for malignant vs. benign classification of lung nodules in thoracic screening ct data. In *2019 IEEE 16th International Symposium on Biomedical Imaging (ISBI 2019)*, pages 1220–1224. IEEE, 2019.

[167] M. B. Rodrigues, R. V. M. Da NóBrega, S. S. A. Alves, P. P. Rebouças Filho, J. B. F. Duarte, A. K. Sangaiah, and V. H. C. De Albuquerque. Health of things algorithms for malignancy level classification of lung nodules. *IEEE Access*, 6:18592–18601, 2018.

[168] A. K. Dhara, S. Mukhopadhyay, A. Dutta, M. Garg, and N. Khandelwal. A combination of shape and texture features for classification of pulmonary nodules in lung ct images. *Journal of digital imaging*, 29(4):466–475, 2016.

[169] W. Huang and S. Tu. Su-f-r-22: Malignancy classification for small pulmonary nodules with radiomics and logistic regression. *Medical physics*, 43(6Part6):3377–3378, 2016.

[170] J. Gong, J.-Y. Liu, X.-W. Sun, B. Zheng, and S.-D. Nie. Computer-aided diagnosis of lung cancer: the effect of training data sets on classification accuracy of lung nodules. *Physics in Medicine & Biology*, 63(3):035036, 2018.

[171] S.-J. Tu, C.-W. Wang, K.-T. Pan, Y.-C. Wu, and C.-T. Wu. Localized thin-section ct with radiomics feature extraction and machine learning to classify early-detected pulmonary nodules from lung cancer screening. *Physics in Medicine & Biology*, 63(6):065005, 2018.

[172] W. Wu, H. Hu, J. Gong, X. Li, G. Huang, and S. Nie. Malignant-benign classification of pulmonary nodules based on random forest aided by clustering analysis. *Physics in medicine and biology*, 64(3):035017–035017, 2019.

[173] N. Guo, R.-F. Yen, G. El Fakhri, and Q. Li. Svm based lung cancer diagnosis using multiple image features in pet/ct. In *2015 IEEE Nuclear Science Symposium and Medical Imaging Conference (NSS/MIC)*, pages 1–4. IEEE, 2015.

[174] S. K. Dilger, J. Uthoff, A. Judisch, E. Hammond, S. L. Mott, B. J. Smith, J. D. Newell, E. A. Hoffman, and J. C. Sieren. Improved pulmonary nodule classification utilizing quantitative lung parenchyma features. *Journal of Medical Imaging*, 2(4):041004, 2015.

[175] G. Wei, H. Ma, W. Qian, H. Jiang, and X. Zhao. Content-based retrieval for lung nodule diagnosis using learned distance metric. In *39th IEEE Annual International Conference of the Engineering in Medicine and Biology Society (EMBC)*, pages 3910–3913, 2017.

[176] G. Wei, H. Ma, W. Qian, F. Han, H. Jiang, S. Qi, and M. Qiu. Lung nodule classification using local kernel regression models with out-of-sample extension. *Biomedical Signal Processing and Control*, 40:1–9, 2018.

[177] A. Nibali, Z. He, and D. Wollersheim. Pulmonary nodule classification with deep residual networks. *International journal of computer assisted radiology and surgery*, 12(10):1799–1808, 2017.

[178] W. Shen, M. Zhou, F. Yang, C. Yang, and J. Tian. Multi-scale convolutional neural networks for lung nodule classification. In *International conference on information processing in medical imaging*, pages 588–599. Springer, 2015.

[179] R. Dey, Z. Lu, and Y. Hong. Diagnostic classification of lung nodules using 3d neural networks. In *2018 IEEE 15th International Symposium on Biomedical Imaging (ISBI 2018)*, pages 774–778. IEEE, 2018.

[180] S. Hussein, K. Cao, Q. Song, and U. Bagci. Risk stratification of lung nodules using 3d cnn-based multi-task learning. In *International conference on information processing in medical imaging*, pages 249–260. Springer, 2017.

[181] K.-L. Hua, C.-H. Hsu, S. C. Hidayati, W.-H. Cheng, and Y.-J. Chen. Computer-aided classification of lung nodules on computed tomography images via deep learning technique. *OncoTargets and therapy*, 8, 2015.

[182] W. Sun, B. Zheng, and W. Qian. Computer aided lung cancer diagnosis with deep learning algorithms. In *Medical imaging 2016: computer-aided diagnosis*, volume 9785, page 97850Z. International Society for Optics and Photonics, 2016.

[183] Q. Song, L. Zhao, X. Luo, and X. Dou. Using deep learning for classification of lung nodules on computed tomography images. *Journal of healthcare engineering*, 2017, 2017.

[184] A. O. de Carvalho Filho, A. C. Silva, A. C. de Paiva, R. A. Nunes, and M. Gattass. Classification of patterns of benignity and malignancy based on ct using topology-based phylogenetic diversity index and convolutional neural network. *Pattern Recognition*, 81:200–212, 2018.

[185] C.-J. Lin, S.-Y. Jeng, and M.-K. Chen. Using 2d cnn with taguchi parametric optimization for lung cancer recognition from ct images. *Applied Sciences*, 10(7):2591, 2020.

[186] S. Suresh and S. Mohan. Roi-based feature learning for efficient true positive prediction using convolutional neural network for lung cancer diagnosis. *Neural Computing and Applications*, pages 1–21, 2020.

[187] W. Shen, M. Zhou, F. Yang, D. Yu, D. Dong, C. Yang, Y. Zang, and J. Tian. Multi-crop convolutional neural networks for lung nodule malignancy suspiciousness classification. *Pattern Recognition*, 61:663–673, 2017.

[188] K. Liu and G. Kang. Multiview convolutional neural networks for lung nodule classification. *International Journal of Imaging Systems and Technology*, 27(1):12–22, 2017.

[189] J. Sang, M. S. Alam, H. Xiang, et al. Automated detection and classification for early stage lung cancer on ct images using deep learning. In *Pattern Recognition and Tracking XXX*, volume 10995, page 109950S. International Society for Optics and Photonics, 2019.

[190] H. Polat and H. Danaei Mehr. Classification of pulmonary ct images by using hybrid 3d-deep convolutional neural network architecture. *Applied Sciences*, 9(5):940, 2019.

[191] C. Zhang, X. Sun, K. Dang, K. Li, X.-w. Guo, et al. Toward an expert level of lung cancer detection and classification using a deep convolutional neural network. *The oncologist*, pages theoncologist–2018, 2019.

[192] M. Al-Shabi, B. L. Lan, W. Y. Chan, K.-H. Ng, and M. Tan. Lung nodule classification using deep local–global networks. *International journal of computer assisted radiology and surgery*, pages 1–5, 2019.

[193] M. Nishio and C. Nagashima. Computer-aided diagnosis for lung cancer: usefulness of nodule heterogeneity. *Academic radiology*, 24(3):328–336, 2017.

[194] D. Kumar, A. Wong, and D. A. Clausi. Lung nodule classification using deep features in CTimages. In *12th IEEE Conference on Computer and Robot Vision*, pages 133–138. IEEE, 2015.

[195] S. Lakshmanaprabu, S. N. Mohanty, K. Shankar, N. Arunkumar, and G. Ramirez. Optimal deep learning model for classification of lung cancer on ct images. *Future Generation Computer Systems*, 92:374–382, 2019.

[196] S. Zhang, F. Sun, N. Wang, C. Zhang, Q. Yu, M. Zhang, P. Babyn, and H. Zhong. Computer-aided diagnosis (cad) of pulmonary nodule of thoracic ct image using transfer learning. *Journal of digital imaging*, pages 1–13, 2019.

[197] Y. Xie, Y. Xia, J. Zhang, D. D. Feng, M. Fulham, and W. Cai. Transferable multi-model ensemble for benign-malignant lung nodule classification on chest ct. In *International Conference on Medical Image Computing and Computer-Assisted Intervention*, pages 656–664. Springer, 2017.

[198] C. A. de Pinho Pinheiro, N. Nedjah, and L. de Macedo Mourelle. Detection and classification of pulmonary nodules using deep learning and swarm intelligence. *Multimedia Tools and Applications*, 79(21):15437–15465, 2020.

[199] G. L. da Silva, O. P. da Silva Neto, A. C. Silva, A. C. de Paiva, and M. Gattass. Lung nodules diagnosis based on evolutionary convolutional neural network. *Multimedia Tools and Applications*, 76(18):19039–19055, 2017.

[200] N. Kalaivani, N. Manimaran, S. Sophia, and D. Devi. Deep learning based lung cancer detection and classification. In *IOP Conference Series: Materials Science and Engineering*, volume 994, page 012026. IOP Publishing, 2020.

[201] Y. Ren, M.-Y. Tsai, L. Chen, J. Wang, S. Li, Y. Liu, X. Jia, and C. Shen. A manifold learning regularization approach to enhance 3d ct image-based lung nodule classification. *International Journal of Computer Assisted Radiology and Surgery*, 15(2):287–295, 2020.

[202] H. Jiang, F. Gao, X. Xu, F. Huang, and S. Zhu. Attentive and ensemble 3d dual path networks for pulmonary nodules classification. *Neurocomputing*, 398:422–430, 2020.

[203] S. B. Shrey, L. Hakim, M. Kavitha, H. W. Kim, and T. Kurita. Transfer learning by cascaded network to identify and classify lung nodules for cancer detection. In

International Workshop on Frontiers of Computer Vision, pages 262–273. Springer, 2020.

[204] B.-C. Kim, Y. S. Sung, and H.-I. Suk. Deep feature learning for pulmonary nodule classification in a lung ct. In *2016 4th International Winter Conference on Brain-Computer Interface (BCI)*, pages 1–3. IEEE, 2016.

[205] S. Shen, S. X. Han, D. R. Aberle, A. A. Bui, and W. Hsu. An interpretable deep hierarchical semantic convolutional neural network for lung nodule malignancy classification. *Expert systems with applications*, 128:84–95, 2019.

[206] G. Zhang, Z. Yang, L. Gong, S. Jiang, and L. Wang. Classification of benign and malignant lung nodules from ct images based on hybrid features. *Physics in Medicine & Biology*, 64(12):125011, 2019.

[207] Y. Xie, J. Zhang, Y. Xia, M. Fulham, and Y. Zhang. Fusing texture, shape and deep model-learned information at decision level for automated classification of lung nodules on chest CT. *Information Fusion*, 42:102–110, 2018.

[208] R. Li, N. W. Todd, Q. Qiu, T. Fan, R. Y. Zhao, W. H. Rodgers, H.-B. Fang, R. L. Katz, S. A. Stass, and F. Jiang. Genetic deletions in sputum as diagnostic markers for early detection of stage i non–small cell lung cancer. *Clinical Cancer Research*, 13(2):482–487, 2007.

[209] Y. Hanai, K. Shimono, K. Matsumura, A. Vachani, S. Albelda, K. Yamazaki, G. K. Beauchamp, and H. Oka. Urinary volatile compounds as biomarkers for lung cancer. *Bioscience, biotechnology, and biochemistry*, 76(4):679–684, 2012.

[210] S. Begum, M. Brait, S. Dasgupta, K. L. Ostrow, M. Zahurak, et al. An epigenetic marker panel for detection of lung cancer using cell-free serum dna. *Clinical Cancer Research*, 17(13):4494–4503, 2011.

[211] P. Zaenker and M. R. Ziman. Serologic autoantibodies as diagnostic cancer biomarkers—a review. *Cancer Epidemiology and Prevention Biomarkers*, 22(12):2161–2181, 2013.

[212] M. Bousamra II, E. Schumer, M. Li, R. J. Knipp, M. H. Nantz, V. Van Berkel, and X.-A. Fu. Quantitative analysis of exhaled carbonyl compounds distinguishes benign from malignant pulmonary disease. *The Journal of thoracic and cardiovascular surgery*, 148(3):1074–1081, 2014.

[213] X.-A. Fu, M. Li, R. J. Knipp, M. H. Nantz, and M. Bousamra. Noninvasive detection of lung cancer using exhaled breath. *Cancer medicine*, 3(1):174–181, 2014.

[214] M. Li, D. Yang, G. Brock, R. J. Knipp, M. Bousamra, M. H. Nantz, and X.-A. Fu. Breath carbonyl compounds as biomarkers of lung cancer. *Lung Cancer*, 90(1):92–97, 2015.

[215] E. M. Schumer, J. R. Trivedi, V. van Berkel, M. C. Black, M. Li, X.-A. Fu, and M. Bousamra II. High sensitivity for lung cancer detection using analysis of exhaled carbonyl compounds. *The Journal of thoracic and cardiovascular surgery*, 150(6):1517–1524, 2015.

[216] E. M. Schumer, M. C. Black, M. Bousamra II, J. R. Trivedi, M. Li, X.-A. Fu, and V. van Berkel. Normalization of exhaled carbonyl compounds after lung cancer resection. *The Annals of thoracic surgery*, 102(4):1095–1100, 2016.

[217] P. Viola and M. Jones. Rapid object detection using a boosted cascade of simple features. In *Computer Vision and Pattern Recognition, 2001. CVPR 2001. Proceedings of the 2001 IEEE Computer Society Conference on*, volume 1, pages I–I. IEEE, 2001.

[218] G. Ekman. Weber's law and related functions. *The Journal of Psychology*, 47(2):343–352, 1959.

[219] A. El-Baz, G. Gimel'farb, and J. S. Suri. *Stochastic modeling for medical image analysis*. CRC Press, 2015.

[220] D. Ziou, S. Tabbone, et al. Edge detection techniques-an overview. *Pattern Recognition and Image Analysis C/C of Raspoznavaniye Obrazov I Analiz Izobrazhenii*, 8:537–559, 1998.

[221] J. Canny. A computational approach to edge detection. *IEEE Transactions on pattern analysis and machine intelligence*, (6):679–698, 1986.

[222] H. Si. Tetgen, a delaunay-based quality tetrahedral mesh generator. *ACM Transactions on Mathematical Software (TOMS)*, 41(2):1–36, 2015.

[223] Q. Fang, S. Carp, J. Selb, R. Moore, D. Kopans, E. Miller, D. Brooks, and D. Boas. A multi-modality image reconstruction platform for diffuse optical tomography. In *Biomedical optics*, page BMD24. Optical Society of America, 2008.

[224] Q. Fang and D. A. Boas. Tetrahedral mesh generation from volumetric binary and grayscale images. In *2009 IEEE International Symposium on Biomedical Imaging: From Nano to Macro*, pages 1142–1145. Ieee, 2009.

[225] G. A. Hansen, R. W. Douglass, and A. Zardecki. *Mesh enhancement: selected elliptic methods, foundations and applications*. World Scientific, 2005.

[226] M. K. Chung, K. M. Dalton, L. Shen, A. C. Evans, and R. J. Davidson. Weighted fourier series representation and its application to quantifying the amount of gray matter. *IEEE transactions on medical imaging*, 26(4):566–581, 2007.

[227] M. Kantardzic. *Data mining: concepts, models, methods, and algorithms*. John Wiley & Sons, 2011.

[228] H. M. Orozco, O. O. V. Villegas, et al. Automated system for lung nodules classification based on wavelet feature descriptor and support vector machine. *Biomedical engineering online*, 14(1):9, 2015.

[229] R. W. de Sousa Costa et al. Classification of malignant and benign lung nodules using taxonomic diversity index and phylogenetic distance. *Medical & biological engineering & computing*, pages 1–12, 2018.

[230] R. Gruetzemacher and A. Gupta. Using deep learning for pulmonary nodule detection & diagnosis. 2016.

CURRICULUM VITAE

Ahmed Mahmoud Ahmed Shaffie

Paul C. Lutz Hall, Room # 304

BioImaging Laboratory

Department of Bioengineering

University of Louisville, Louisville, KY, USA

E-mail: *Ahmed.Shaffie@louisville.edu*,

amshaffie.oq@gmail.com

Tel: (502) 807-3809

Education

2015-Present Ph.D. Student, Department of Computer Engineering and Computer Science, University of Louisville, Louisville, KY 40292, USA

PhD Candidate since Spring 2017, GPA = $4.0/4.0$.

2012 M.Sc., Department of Engineering Mathematics and Physics, Alexandria University, Alexandria 21526, Egypt.

M.Sc. Thesis: *Recognition System for Isolated Arabic Characters Using Center of Gravity*- Dr. Galal Elkobrosy and Abdelfatah Rizk, Thesis Advisors.

2005 B.Sc., Computer Science and Automatic Control Department, Alexandria University, Alexandria 21526, Egypt.

Sr. Project: *Data mining as a tool for intrusion detection system.*

Experience

2015–2019 Graduate Research Assistant, BioImaging laboratory, Department of Bioengineering, University of Louisville, Louisville, KY 40292, USA.

2006–2015 Graduate Research Assistant, Department of Engineering Mathematics and Physics, Alexandria University, Alexandria 21526, Egypt.

Professional Affiliations and Training

- Member, Institute of Electrical and Electronics Engineers (IEEE).
- Member, IEEE Signal Processing (SPS) Society.
- Member, Biomedical Engineering Society (BMES).

Awards and Recognition

- ***Student Research Exposition, 2019,*** The first place award in the Doctoral category.
- ***Exemplary Research Scholarship Award, 2019*** University of Louisville, Bioengineering Department.
- ***Research Louisville, 2018,*** The first place award in the Doctoral Engineering category.
- ***Student Research Exposition, 2018,*** The first place award in the Doctoral category.
- ***Research Louisville, 2017,*** The first place award in the Doctoral Engineering category.
- ***Graduate Student Scholarship,*** University of Louisville, Fall 2015- Spring 2018
- ***Degree of Honor,*** of Cumulative Academic Distinction, Alexandria University, June 2005.
- ***Academic Distinction Award,*** for excellence outstanding students Faculty of Engineering, Alexandria University, 2002 - 2005.

Publications

During my Ph.D. (Fall 2015–*****), I have authored or co-authored more than **** technical publications that have appeared in world-renown journals, book chapters, top-rank international conferences and workshops , and abstracts.

- **Journal Articles (Total =** 3)

    1. **A. Shaffie** and G. Elkobrosy "Fast Recognition System for Isolated Printed Characters Using Center of Gravity and Principal Axis," *Applied Mathematics (AM),* vol. 4, no. 9, pp. 1313–1319, 2013.
    2. **A. Shaffie**, A. Soliman, Luay Fraiwan, M. Ghazal, F. Taher, N. Dunlap, B. Wang, V. van Berkel, G. Gimel'farb, A. Elmaghraby, and A. El-Baz, "A Generalized Deep Learning Based Diagnostic System for Early Diagnosis of Various Types of Pulmonary Nodules," *Technology in Cancer Research & Treatment Journals,* vol. 17, 2018.
    3. **A. Shaffie**, A. Soliman, X. Fue, M. Nantz, G. Giridharan, V. Berkel, H. Khalifeh, M. Ghazal, A. Elmaghraby, and A. El-baz, "A Novel Technology to Integrate Imaging and Clinical Markers for Non-Invasive Diagnosis of Lung Cancer," *Scientific Reports,* vol. 11, 2021.

- **Books (Total = 3)**

    1. **A. Shaffie**, A. Soliman, A. Mahmoud, M. Ghazal, H. Hajjdiab, R. Keynton, G. Giridharan, Adel Elmaghraby, J. Suri, and A. El-Baz, "Lung Nodule Classification based on the Integration of Higher-Order MGRF Appearance Model and Geometric Features," *in Lung Imaging and CADx*, CRC Press, 2019, ch. 9, pp. 203–215.
    2. A. Soliman,F. Khalifa, **A. Shaffie**, A. Mahmoud, N. Dunlap, B. Wang, A. Elmaghraby, G. Gimel'farb, R. Keynton, M. Ghazal, J. Suri, A. El-Baz, "Lung Nodule Classification based on the Integration of Higher-Order MGRF Ap-

pearance Model and Geometric Features," *in Lung Imaging and CADx*, CRC Press, 2019, ch. 15, pp. 249–264.

3. **A. Shaffie**, "A Fast Recognition System for Isolated Printed Characters Using Center of Gravity," *LAP LAMBERT Academic Publishing*, 2011, ISBN: 978-3-8465-0002-6.

- **Peer-Reviewed Conference Proceedings (Total = 19)**

1. M. Shehata, F. Khalifa, A. Soliman, A. Takieldeen, M. A. El-Ghar, **A. Shaffie**, A. C. Dwyer, R. Ouseph, A. El-Baz, and R. Keynton, "3D Diffusion MRI-Based CAD System for Early Diagnosis of Acute Renal Rejection," In: *Proceedings of IEEE International Symposium on Biomedical Imaging: From Nano to Macro (ISBI'16)*, Prague, Czech Republic, April 13–16, 2016, pp. 1177-1180.
2. F. Khalifa, A. Soliman, A. Takieldeen, M. Shehata, M. Moustapha, **A. Shaffie**, R. Ouseph, A. Elmaghraby, and A. El-Baz, "Kidney Segmentation from CT Images Using A 3D NMF-Guided Active Contour Model," In: *Proceedings of IEEE International Symposium on Biomedical Imaging: From Nano to Macro (ISBI'16)*, Prague, Czech Republic, April 13–16, 2016, pp. 432-435.
3. A. Soliman, F. Khalifa, **A. Shaffie**, N. Dunlap, B. Wang, A. Elmaghraby, and A. El-Baz, "Detection of Lung Injury Using 4D-CT Chest Images," In: *Proceedings of IEEE International Symposium on Biomedical Imaging: From Nano to Macro (ISBI'16)*, Prague, Czech Republic, April 13–16, 2016, pp. 1274-1277.
4. A. Soliman, F. Khalifa, **A. Shaffie**, N. Liu, N. Dunlap, B. Wang, A. Elmaghraby, G. Gimel'farb, and A. El-Baz. "Image-based CAD system for accurate identification of lung injury," In: *Proceedings of IEEE International Conference on Image Processing (ICIP 2016)*, Phoenix, USA, Sept 25–28, 2016,

pp. 121-125.

5. **A. Shaffie**, A. Soliman, M. Ghazal, F. Taher, N. Dunlap, B. Wang, A. Elmaghraby, G. Gimel'farb and A. El-Baz, "A New Framework for Incorporating Appearance And Shape Features Of Lung Nodules for Precise Diagnosis Of Lung Cancer," In: *Proceedings of IEEE International Conference on Image Processing (ICIP 2017)*, Beijing, China, Sept 17–20, 2017, pp. 1372-1376.
6. A. Soliman, F. Khalifa, **A. Shaffie**, N. Dunlap, B Wang, A. Elmaghraby, G. Gimel'farb, M Ghazal, and A. El-Baz," A Comprehensive Framework for Early Assessment Of Lung Injury," In: *Proceedings of IEEE International Conference on Image Processing (ICIP 2017)*, Beijing, China, Sept 17–20, 2017, pp. 3275-3279.
7. **A. Shaffie**, A. Soliman, N. Dunlap, B. Wang, A. Elmaghraby, G. Gimel'farb, V.V. Berkel, and A. El-Baz, "A New Framework for Incorporating Appearance and Shape Features of Lung Nodules for Precise Diagnosis of Lung Cancer," In: *Biomedical Engineering Society (BMES 2017*, Phoenix, Arizona, USA, Oct 11–14, 2017, (Poster).
8. **A. Shaffie**, A. Soliman, M. Ghazal, F. Taher, N. Dunlap, B. Wang, V. van Berkel, G. Gimel'farb, A. Elmaghraby, and A. El-Baz, "A Novel Autoencoder-Based Diagnostic System for Early Assessment of Lung Cancer," In: *Proceedings of IEEE International Conference on Image Processing (ICIP 2018)*, Athens, Greece, Oct 7–10, 2018, pp. 1393-1397.
9. A. Soliman, **A. Shaffie**, M. Ghazal, G. Gimel'farb, R. Keynton, and A. El-Baz, "A Novel CNN Segmentation Framework based on using New Shape and Appearance Features," In: *Proceedings of IEEE International Conference on Image Processing (ICIP 2018)*, Athens, Greece, Oct 7–10, 2018, pp. 3488-3492.
10. **A. Shaffie**, A. Soliman, V.V. Berkel, N. Dunlap, B. Wang, M. Ghazal, G.

Gimel'farb, X. Fu, M. Nantz, A. Elmaghraby, G. Giridharan, and A. El-Baz, "Integration of Imaging based Markers and Clinical Biomarkers for Early Detection of Lung Cancer," In: *Biomedical Engineering Society (BMES 2018*, Atlanta, Georgia, USA, Oct 17–20, 2018, (Poster).

11. **A. Shaffie**, A. Soliman, H. Abu Khalifeh, M. Ghazal, F. Taher, R. Keynton, A. Elmaghraby, and A. El-baz, "On The Integration of CT-Derived Features for Accurate Detection of Lung Cancer," In: *Proceedings of IEEE Symposium on Signal Processing and Information Technology (ISSPIT 2018)*, Louisville, Kentucky, USA, Dec 6–8, 2018, pp. 435-440.
12. **A. Shaffie**, A. Soliman, H. Abu Khalifeh, M. Ghazal, F. Taher, A. Elmaghraby, R. Keynton, and A. El-baz, "Radiomic-Based Frame Work For Early Diagnosis Of Lung Cancer" In: *Proceedings of IEEE International Symposium on Biomedical Imaging (ISBI'19)*, Venice, Italy, April 8–11, 2019.
13. **A. Shaffie**, A. Soliman, H. Abu Khalifeh, F. Taher, M. Ghazal, N. Dunlap, A. Elmaghraby, R. Keynton, and A. El-baz, "A Novel CT Based Descriptors for Precise Diagnosis of Pulmonary Nodules," In: *Proceedings of IEEE International Conference on Image Processing (ICIP 2019)*, Taipei, Taiwan, Sept 22–25, 2019.
14. **A. Shaffie**, A. Soliman, H. Abu Khalifeh, F. Taher, M. Ghazal, N. Dunlap, A. Elmaghraby, R. Keynton, and A. El-baz, "A New System for Lung Cancer Diagnosis based on the Integration of Global and Local CT Features," In: *Proceedings of IEEE International Conference on Imaging Systems and Techniques (IST 2019)*, Abu Dhabi, UAE, December 8–10, 2019.
15. **A. Shaffie**, A. Soliman, V. van Berkel, N. Dunlap, B. Wang, M. Ghazal, G. Gimel'farb, X. Fu, M. Nantz, G. Giridharan, and A. El-Baz,, "Integration of Imaging based Markers and Clinical Biomarkers for Early Detection of Lung Cancer," In: *BMES 2020 Virtual Annual Meeting,*, October, 2020.

16. **A. Shaffie**, A. Soliman, H. Khalifeh, M. Ghazal, F. Taher, A. Elmaghraby, R. Keynton, and A. El-Baz, "A Comprehensive Framework for Accurate Classification of Pulmonary Nodules," In: *Proceedings of IEEE International Conference on Image Processing (ICIP 2020)*, Abu Dhabi, UAE, October 25-28, 2020.
17. A. Alksas, M. Shehata, G. Saleh, **A. Shaffie** , A. soliman, M. Ghazal, H. Khalifeh, A. AbdelRazek, and A. El-Baz, "A Novel Computer-Aided Diagnostic System for Early Assessment of Hepatocellular Carcinoma," In: *Proceedings of IEEE International Conference on Pattern Recognition (ICPR 2021)*, Milano, Italy, January 10-15, 2021.
18. M. Shehata, A. Alksas, R. Abouelkheir, A. Elmahdy, **A. Shaffie**, A. Soliman, M. Ghazal, H. Khalifeh, A. Abdel Razek, and A. El-baz, "A New Computer-Aided Diagnostic (CAD) System For Precise Identification Of Renal Tumors" In: *Proceedings of IEEE International Symposium on Biomedical Imaging (ISBI'21)*, Nice, France, April 13–16, 2021.
19. **A. Shaffie**, A. Soliman, H. Khalifeh, M. Ghazal, F. Taher, A. Elmaghraby, and A. El-Baz, "A Novel Framework for Accurate and Non-invasive Pulmonary Nodule Diagnosis by Integrating Texture and Contour Descriptors" In: *Proceedings of IEEE International Symposium on Biomedical Imaging (ISBI'21)*, Nice, France, April 13–16, 2021.

- **Patents and Disclosures (Total = 2)**

1. **A. Shaffie**, A. El-Baz, A. Soliman, , F. Khalifa, N. Dunlap, B. Wang, "Accurate Detection and Assesment of Radiation Induced Lung Injury based on Computational Model and Computed Tomography Imaging," *U.S. Non-Provisional patent ULRF No. 16078-02*.
2. **A. Shaffie**, A. El-Baz, A. Soliman, , G. A. Giridharan, V. van Berkel, X. Fu,

M. H. Nantz, ”Breath Analysis-CAD Platform for Early, Accurate Detection of Small Lung Nodules,” *U.S. Disclosure ULRF No. 118032*.

Graduate Advisors

Dr. Adel Elmaghraby, Dissertation Co-advisor, Department of Computer Science and Engineering; and **Dr. Aymen El-baz**, Dissertation Co-advisor, Department of Bioengineering, Speed School of Engineering, University of Louisville, Louisville, KY.